The Dissertation Committee for Frederick Theodore Nugen
certifies that this is the approved version of the following dissertation:

**Advances in saccular aneurysm biomechanics:
enlargement via rate-sensitive inelastic growth,
bio-mathematical stages of aneurysm disease,
and initiation profiles.**

Committee:

Thomas J. R. Hughes, Co-supervisor

Robert D. Moser, Co-supervisor

Ronald E. Barr

Michael S. Sacks

Oscar Gonzalez

H. Kent Beasley

Craig M. Kemper

Advances in saccular aneurysm biomechanics: enlargement via rate-sensitive inelastic growth, bio-mathematical stages of aneurysm disease, and initiation profiles.

by

Frederick Theodore Nugen, B.S. Math., M.S., M.S.

DISSERTATION

Presented to the Faculty of the Graduate School of

The University of Texas at Austin

in Partial Fulfillment

of the Requirements

for the Degree of

DOCTOR OF PHILOSOPHY

THE UNIVERSITY OF TEXAS AT AUSTIN

December 2016

My thanks go firstly to my advisor, Thomas J. R. Hughes, who is inspiring, patient, flexible, perspicacious, has an unbeatable sense of direction, gives great advice, tells wonderful stories, and thinks of everything.

When Tom speaks, he only says one sentence at a time; yet somehow he adds value for everyone in the room simultaneously, regardless of their familiarity with the subject at hand. New people learn an overview, and well-educated people get new perspective; or well-educated people learn something new, and new people see where the edge of science is. Everyone in between has a better understanding of what aspects of the subject are most important.

Presented with a puzzling issue, Tom drills down and uncovers the cause even when it is far from his area of expertise. He is excellent at stripping away extraneous effects and revealing the core behavior of any problem.

Tom, thank you for introducing me to so many eminent researchers. I owe my entire career and future prospects to you.

Thanks go to my many collaborators over the years: Michael Borden, Luca Dedè, Oscar Gonzalez, Kent Beasley MD, Tate Erlinger MD, Craig Kemper MD, Christian Gasser, Shaolie Hossain, John Evans, and Ju Liu.

I made this journey with the emotional support of many people, including Bob Nugen, Kathleen Ellis, Jon Montgomery, Rob Nugen, Rene Heimstra, William McKenna, David Cruz, Michael Ossowski, Robert Ristroph, and Kagan Thornton; with the aid of staff members Lorraine Sanchez, Christine Bailor, and Cynthia Steiner; and with the many baristas who provided a pleasant secondary office.

Thanks also go to Tinsley Oden and everyone at the Institute for Computational Engineering and Sciences and the Department of Mechanical Engineering for endless patience and support.

This work could not have been completed without the support of Mary Magel and The Missy Project. I am endlessly grateful to them.

The work herein was made possible by grants from the following sources (in reverse chronological order):

- The Missy Project;
- Kathleen Ellis;
- The Missy Project via Brain and Spine Center, Brackenridge Hospital;
- Texas Higher Education Coordinating Board,

  Norman Hackerman Advanced Research Program, #003658-0025-2006;
- National Science Foundation, #0417446.

Advances in saccular aneurysm biomechanics: enlargement via rate-sensitive inelastic growth, bio-mathematical stages of aneurysm disease, and initiation profiles.

Frederick Theodore Nugen, Ph.D.
The University of Texas at Austin, 2016

Supervisors: **Thomas J. R. Hughes**
Robert D. Moser

I have created the first simulation of saccular aneurysm initiation and development from a healthy artery geometry. It is capable of growing saccular aneurysm geometries from patient-specific data. My model describes aneurysm behavior in a way that bridges fields. I assume arteries are made of a rate-sensitive inelastic material which produces irreversible deformation when it is overstressed. The material is assumed to consist of a 3D hyperelastic background material embedded with 1D transversely-isotropic fibers. I optionally use a Winkler foundation term to model support of external organs and distinguish healthy tissue from diseased tissue. Lesions are defined as a local degradation of artery wall structure. My work suggests passive mechanisms of growth are insufficient for predicting saccular aneurysms. Furthermore, I identify a new concept of stages of aneurysm disease. The stages connect mathematical descriptions of the simulation with clinically-relevant changes in the modeled aneurysm. They provide an evocative framework through which clinical descriptions of arteries can be neatly matched with mathematical features of the

model. The framework gives a common language of concepts—e.g., collagen fiber, pseudoelastic limit, inelastic strain, and subclinical lesion—through which researchers in different fields, with different terminologies, can engage in an ongoing dialog: under the model, questions in medicine can be translated into equivalent questions in mathematics. A new stage of "subclinical lesion" has been identified, with a suggested direction for future biomechanics research into early detection and treatment of aneurysms. This stage defines a preclinical aneurysm-producing lesion which occurs before any artery dilatation. It is a stage of aneurysm development involving microstructural changes in artery wall makeup. Under the model, this stage can be identified by its reduced strength: its structural support is still within normal limits, but presumably would perform more poorly in *ex vivo* failure testing than healthy tissue from the same individual. I encourage clinicians and biomechanicians to measure elastin degradation, and to build detailed multiscale models of elastin degradation profiles as functions of aging and tortuosity; and similarly for basal tone. I hope such measurements will to lead to early detection and treatment of aneurysms. I give specific suggestions of biological tissue experiments to be performed for improving and reinforming constitutive modeling techniques.

Table of Contents

Chapter 1

Introduction

Computer simulation is revolutionizing healthcare research. It has bolstered clinical diagnoses and treatment. It allows well-informed decisions to replace educated guesses. It allows safe, low-cost calculations to replace expensive, risky procedures. It reduces costs for development of new devices. It is an intersection point for collaboration, and inspires joint institutions for translational medicine.

I have garnered the experience of physicians and engineers to provide predictive diagnostics for the treatment of disease, so that physicians can intervene before a patient becomes untreatable. This work is intended to build infrastructure for sharing and collaborative research between engineering and medicine, toward a common goal: improving patient care.

I have developed a modeling paradigm for the creation of patient-specific geometries of arteries; an analytic framework for describing the growth mechanics of aneurysms as a fiber-based inelastic material; and, a descriptive framework for connecting clinical features of aneurysm development with mathematical descriptions of model variables. Together, they provide a predictive capability for aneurysm modeling, from patient-specific image data to predicted outcome.

The theoretical formulation synthesizes existing concepts in the mechanics literature with novel developments in biological modeling and will provide physicians with tools of superior accuracy and predictive value. It takes standard equations that govern the

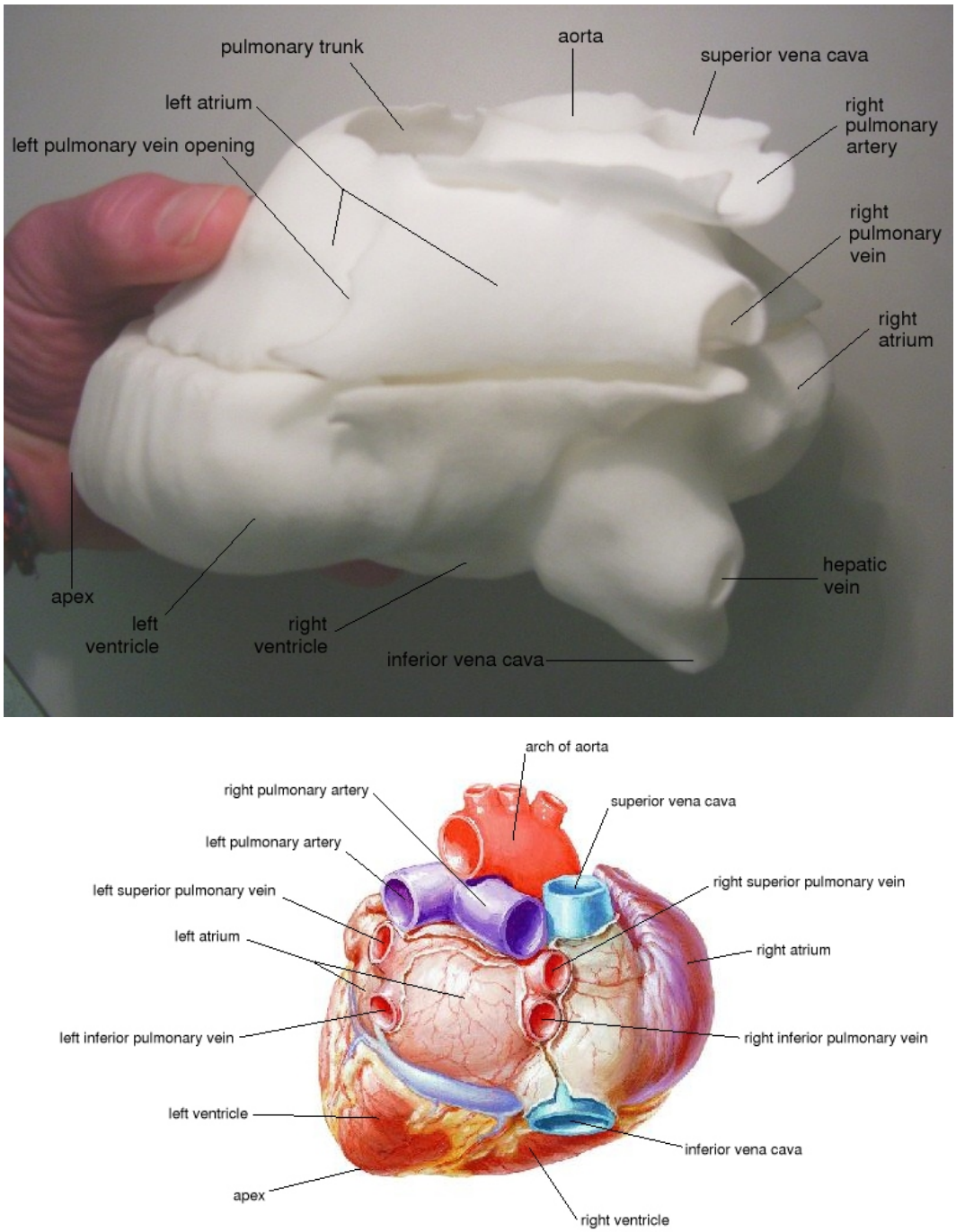

Figure 1: Comparison of a subject-specific model of a human heart and a standard educational model [Netter 2003, plate 210a]. Major differences in geometry and structure are normal. For example, the subject has only one pulmonary vein on each side of the heart (left and right); educational models show two on each side.

behavior of materials that change in mass, and couples it with a biologically-viable growth law. The entire formulation is implemented in the computational framework of isogeometric analysis, using smooth geometries, ensuring accurate and stable results. Most computer modeling technologies require an additional meshing step which is time-consuming, reduces accuracy, and introduces stress singularities. [Cottrell 2009]

A portion of this work is the development of a modeling pipeline for building accurate geometries of the heart and arteries, demonstrated in Figure 1. The heart model in Figure 1 is a useful tool for facilitating communication between physicians, engineers, and patients. The modeling pipeline is the basis for a general technique for modeling organs in the body, demonstrated in Figure 3. The modeling pipeline formalizes existing model-building techniques for the cardiovascular system and can extend tools that have been developed for blood flow, turbulence, and solid mechanics computations.

The simulation will build on existing technologies for modeling tissue as an anisotropic elastic material. Other researchers in the literature have utilized models for describing fiber-based material, including terms for growth and decay (change of mass), and a notion of history-dependent turnover of tissue. However, a complete model for aneurysm disease has not been formed.

A new era was introduced in [Taylor 1998], in which patient-specific engineering simulations are run to evaluate the relative value of various possible treatments and to plan and design the optimal intervention. The automation and improvements of the present modeling system are necessary to provide better conclusions of the behavior and mechanical nature of diseased arteries as well as improve the overall predictive capability of sim-

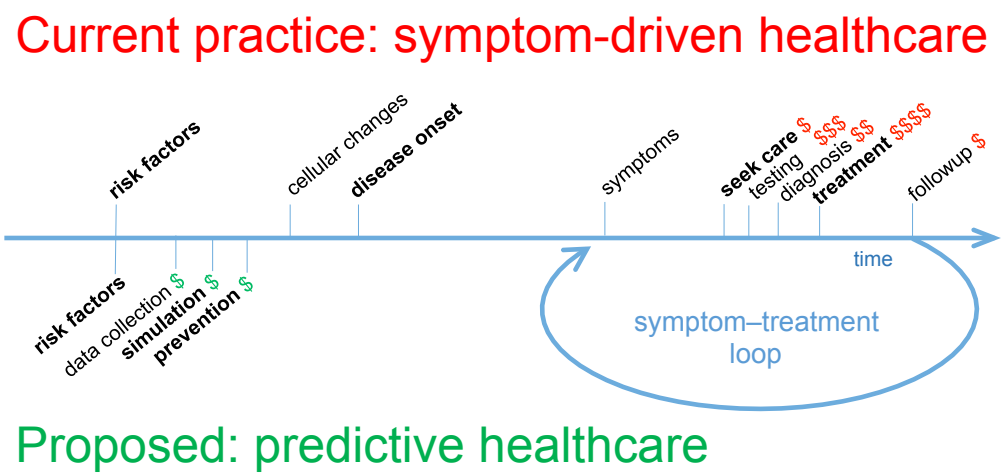

Figure 2: Existing and proposed strategies for providing healthcare. Many diseases, such as aneurysms and atherosclerosis, are not discovered until the disease has progressed into advanced stages. I propose predictive systems which will alert physicians to potential problems, before damage has occurred. Early treatments can be less costly, less invasive and have fewer side effects.

ulation tools. Physicians who use these tools will better understand aneurysm dynamics, improve their morbidity and mortality rates, and save lives.

1.1 Broader Impact

The broader impact of this work is its ability to suggest novel tissue measurements and facilitate collaborative analysis between physicians and engineers. Quantities computed in this work can indicate risk factors for aneurysm enlargement. Current risk factors have low predictability and high variability.

Most biological mechanisms within arteries are difficult or impossible to measure *in vivo*. I suggest measurements which can be used to understand initiation of disease and aging processes in the body. The measurements will improve researchers' ability to

distinguish distinct etiologies of aneurysms, by helping to classify outcomes with initial parameters.

I created a modeling pipeline for building patient-specific artery geometries. This is an important stepping stone for computational medicine. The ability to run predictive simulations on patient-specific data is a crucial advance in clinical decision support. See Figure 2.

I subdivided the computed results into distinct stages in time. The stages were defined by mathematical properties of the constitutive model, and they neatly connect with clinical presentations of aneurysms. One of the stages corresponds to an unrecognized stage of disease progression.

When performing simulations, I found classes of initial data in which the computed results are predictive of certain observed outcomes. By investigating the effects of internal model variables, I can begin to form postulates/hypotheses for a physical interpretation for the variables. With a physical interpretation can come biological experiments and measurements. Specifically, I suggest careful measurement of elastin degradation profiles in space and time. These measurements should create advances within the medical community for treatment and risk assessment.

1.2 Specific Aims

This work investigates specific implications of a biomechanics growth model for aneurysms.

One investigation is to quantify and analyze force and stress distributions in unruptured intracranial saccular aneurysm deformations. From a given deformation, stresses, forces, and strains can be calculated, giving insight into the environments of aneurysms.

Internal parameters can be determined to give physiologically-reasonable results. They cannot be measured *in vivo*, but they can be easily displayed in a simulation.

I created a realistic saccular aneurysm deformation, beginning from a healthy artery and deforming into a diseased configuration. I computed the stresses involved to effect such a deformation. My observations indicated the need for a supporting force at the neck to effect a saccular aneurysm (as opposed to a fusiform aneurysm). I also discovered existing constitutive models were insufficient to describe the development of saccular aneurysms under physiologic conditions. Existing constitutive models required nonphysiologic conditions.

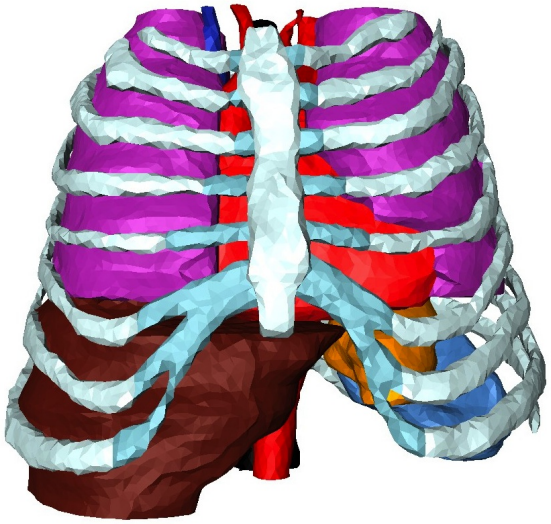

Figure 3: The author's segmentation of thoracic organs for a company seeking FDA approval. The FDA increasingly requires computational analysis for new technology. Included are the ribcage, lungs, heart, liver, spleen, stomach, aorta, spinal cord, and vena cava.

I developed a new constitutive model for describing the disease process within aneurysms. It uses rate-sensitive inelasticity to describe strain during disease.

I created a pipeline for building patient-specific geometries of arteries. The pipeline and patient-specific data helped us postulate an initial lesion.

I applied physiologic forces to the model to grow saccular aneurysm geometries from healthy configurations. These simulations are driven by blood pressure and the postulated lesion.

I have identified directions for future research. I suggest investigating the effect of elastic limit profiles on aneurysm shape. I also propose tissue experiments which can be performed to improve the models herein, and will help improve models of aging in other tissues.

Finally, I propose the identification of stages of aneurysm disease. The stages in this work align corresponding terminology from medicine, engineering, and mathematics. The alignment provides a means for mathematical descriptions of medical findings. With this it is possible to create new understanding in each field. One new clinical stage has been identified: "subclinical lesion." The idea will be explored with clinicians and biomechanicians, to improve and refine the model. For the stages to have the greatest impact, input from many different sources should be incorporated.

1.3 Clinical background and significance

An aneurysm is a bulge in the wall of an artery, a vein, or the heart. Arterial aneurysms occur in only a few places for reasons that are not fully understood: mainly in the abdominal aorta and cranial arteries, especially near or on the Circle of Willis.

Aneurysms are classified into saccular aneurysms and fusiform aneurysms, depicted in Figure 4. Sites of diagnosed saccular aneurysms are shown in Figure 5. They are common, life-threatening, and poorly understood. A ruptured aneurysm is often debilitating or lethal. The mechanisms for enlargement and remodeling are unknown and there exist no tests to determine which will grow or which aneurysms are stable. Imaging aneurysms is either expensive (magnetic resonance imaging), invasive (catheterization), or toxic (x-ray computed tomography). Routine screening is not done. Consequently, little is known about the disease process.

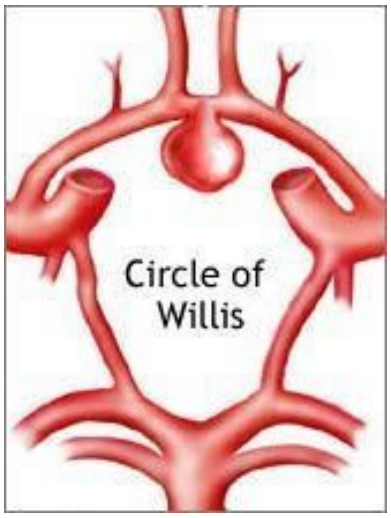

(a) Saccular aneurysm in the anterior communicating artery (top) of the Circle of Willis. Saccular aneurysms usually form at the flow divider of a branch; the fibrous layer is weaker there.

(b) Physical model of a patient's abdominal aortic aneurysm prior to surgery. This is an example of a fusiform aneurysm. They often involve branch vessels.

Figure 4: Distinction between aneurysms: a saccular aneurysm of the brain, and a fusiform aneurysm of the abdominal aorta. The etiology for intracranial and abdominal aneurysms is different, but they have an underlying principle in common: the tissue becomes weakened and subsequently bulges outward as a result of blood pressures. This work investigates intracranial saccular aneurysms, depicted in (a).

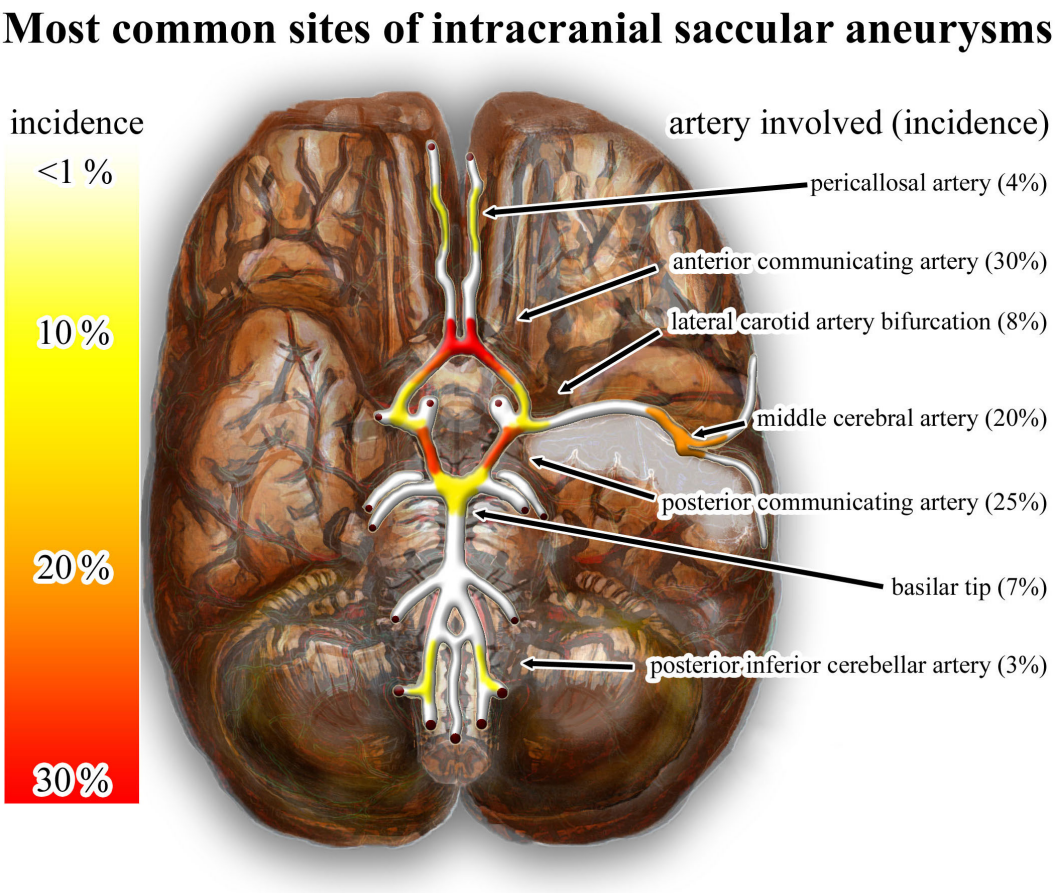

Figure 5: The most common sites of diagnosed intracranial saccular aneurysms. [Zaorsky 2011]

In modeling aneurysms, I simulate tissue-level mechanics of artery walls. There has been significant effort put into mechanical modeling of arteries in the past few decades. It is established that arteries consist of several layers of tissues, and that the tissues are partly composed of collagen fibers whose main (mechanical) purpose is reinforcement of the tissue. There are, investigations have shown, multiple "families" of fibers, symmetrically oriented in a helix fashion, and there is some spread to the distribution of fiber angles. These fibers have dynamic roles in the makeup of artery walls, and characterizing that role is ongoing research in arterial wall modeling.

According to [Kroon 2007], fibers are largely circumferentially oriented near the interior surface (5–10° from circumferential); helically oriented near the exterior surface (50° from circumferential); and vary smoothly between.

Histology studies suggest arteries begin healthy, deform into a bleb without a neck, then into a saccular shape with a clear neck. (The neck does not seem to form by a "pinching" of a fusiform aneurysm.) This understanding is based on shapes of aneurysms commonly observed; there is comparatively little longitudinal data. Growing aneurysms are considered deadly and would be intervened upon if possible. Histology studies suggest a localized region of healthy tissue becomes overly weakened, such that it cannot maintain its healthy shape, and bulges outward due to blood pressure. Weakening occurs due to loss of the muscular layer and also disruption of the collagen fiber network. Structural changes occur within the artery wall, causing the tissue increases its surface area (by production of new tissue, not necessarily by stretching like a balloon).

Some researchers and clinicians suggest that some people may be born with a propensity for localized degradation of arterial tissue. Congenital aneurysm disease I clas-

sify as arterial malformation; it is not in the scope of this work. In this work, I investigate only acquired aneurysm disease.

Animal testing has yielded limited results. Methods for causing aneurysms—such as suturing in a pocket of tissue, degrading the aneurysm wall with chemicals, and physically scarring the arterial wall—cause unnatural structural changes. It is unclear what value they have for predicting progression of naturally-formed human aneurysms. New techniques for evaluating aneurysms are imperative.

Aneurysms have several mechanical measures by which their risk of rupture is evaluated. The main ones are maximum diameter, rate of expansion, and wall shear stress. Saccular aneurysms also have the neck-to-height ratio. Maximum diameter is widely considered inadequate, the rate of expansion is almost never known, wall shear stress cannot be measured,[1,2] and neck-to-height ratio is unreliable [Nader-Sepahi 2004]. Aneurysms regularly defy the measures: many small aneurysms rupture, and many large aneurysms do not. Owing to studies showing enlargement is correlated with rupture, maximum diameter is the predominant clinical standard. Upper and lower boundaries for dictating treatment are deliberately vague and based on a balance of risks.[3]

As treatment becomes safer and more effective, treatment guidelines have become more aggressive. Overtreatment is an imperfect solution, however. We need predictive models to become more selective and more accurate with our treatment choices.

[1] Also, while abnormal wall shear stress is used to indicate danger, it is not settled whether or in what conditions high or low wall shear stress is protective or harmful, nor even a range of "safe" levels of wall shear stress.

[2] Wall shear stress can be reverse engineered in some situations [Lu 2013].

[3] A physician must also consider associated symptoms, suitability for surgery, and patient and familial history.

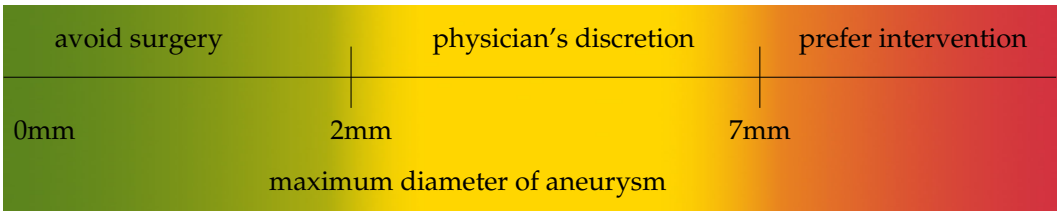

Figure 6: Cut points showing what appear to be current-practice guidelines for cranial aneurysms [Beck 2006, commentary]. Large and small aneurysms have accepted treatments; a new tool's greatest utility lies in regions of uncertainty.

For each type of aneurysm, if the maximum diameter is below a lower bound (assuming the aneurysm is otherwise uncomplicated), surgery is usually not performed. See Figure 6. Above some upper bound, physicians will tend to strongly recommend intervention. In between, physicians have discretion—this is where a predictive tool finds its greatest effect. Focusing on this limited range of the commonest aneurysms maximizes the applicability of one's efforts and has the greatest value to the medical community.

Before operating on an intracranial aneurysm, a physician insists upon seeing an image of the aneurysm in order to envision its geometry in three dimensions. The physician is not satisfied with seeing one or two orthogonal projections—s/he wants to rotate a three-dimensional surface representation or to increment through parallel slices.

This insistence upon a three dimensional representation demonstrates a belief that the *geometry* of an aneurysm is a key feature of its treatment. In fact, aneurysms with irregular walls or blebs are known to be more dangerous than less complicated ones. Physicians need tools that evaluate *geometry* in terms of its risk of worsening. Geometric *quantifiers* must be developed.

This work is a necessary step toward the greater goal of establishing a geometric quantifier for the evaluation of an aneurysm's disease progression. The quantifier should

provide a risk measure for physicians to understand the likelihood of the aneurysm's enlargement. It should also provide a means of comparing risk of one shape in one environment with the risk of a different shape in a different environment, but to do that, one must first build predictive modeling and simulation tools.

The medical community is ready for these tools. A patient-specific computational tool for the evaluation of aneurysms can be easily inserted into the differential diagnosis physicians and hospitals use to treat this condition:

1. It will use imaging data already taken for this condition.
2. Its use will not contradict or invalidate any existing treatment options.
3. Physicians already want this capability.
4. No tool exits to perform the task.

Now is the time to build one.

The current work develops understanding of the mechanics of growth and remodeling of solids with two fiber families through rate-dependent inelastic strain. As shown below, this is my geometric quantifier.

A main focus of the current research is to provide a medical professional with a detailed geometry that accurately depicts the nuances of a patient-specific aneurysm. Accurate geometries will enable precise predictions of the aneurysm's behavior. Current technology allows only general predictions.

Modeling pipelines are necessary since most medical imaging is designed for visualization and is not suitable for computation. (Some threshold-based computational techniques exist for raw CT data.) Several pipelines have been developed for this work. A preliminary pipeline, used to model the human heart, is discussed below. See Figure 7.

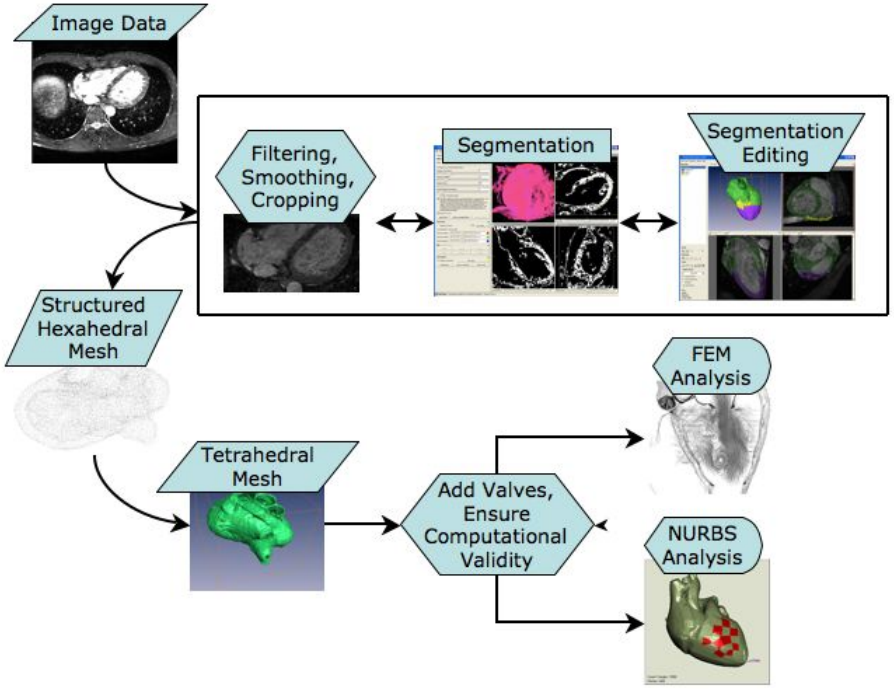

(a) Original pipeline for heart modeling, depicting task dependency.

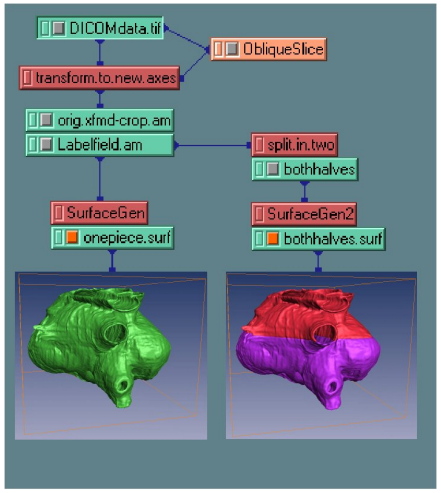

(b) Simplified data flow diagram for manual segmentation process. The right-hand image shows the cut into two parts, for the purpose of viewing the interior of the physical model.

Figure 7: Heart pipeline used to construct the model shown in Figure 1 on page 2. The segmentation software output a triangle surface mesh, which is the input required for the rapid prototyping machine used to produce the plastic model. The same pipeline was used for arteries. (See Chapter 5 below.)

One of the characteristic features of an imaging pipeline is its segmentation process. Segmentation is intractable, and a segmentation process which yields good results for one organ and imaging modality often does not work well for a different organ or modality, even if the two organs share a boundary. For instance, in segmenting the lungs, one may be tolerant of including pulmonary vessels here and there; in segmenting the pulmonary vessels, incorrect connections can completely change the structure of the pulmonary network.

The current work brings together several emerging lines of research on vascular anatomy and hemodynamic simulation. Among the territories which have been overlooked is the development of physiologic boundary conditions for the arterial wall.

1.4 Constitutive modeling background

Aneurysms are common, life threatening, and poorly understood. It is nearly impossible to observe the disease process which leads to aneurysms, especially in early stages. As a result, little is known about causes of the disease, and there is no strongly-correlated marker of patient prognosis. Several things are known. Biomechanical extension tests of artery tissue show an elastic response to applied loads at low-to-moderate strain; irreversible damage to the arterial wall is the main proponent of aneurysm rupture; and collagen fiber remodeling is a chief mechanism of damage. These observations suggest nonlinear solid mechanics is an appropriate framework for investigating onset and progression of aneurysms.

Significant research has been performed on careful analysis of elastic properties of aneurysms (strain energy coefficients, fiber directions, fiber dispersion). In addition, some recent work has been performed on insensitivity of aneurysm models to elastic parameters.

In this work, I gather results and observations from that body of research into an elastic model. On top of that, I investigate properties of an inelastic theory. The inelastic theory is an improvement over existing constitutive models in that it has the capability to produce realistic saccular aneurysm geometries, which no other theory has been shown to produce from a healthy artery.

1.4.1 Homeostatic stress

One common theory assumes that tissues enjoy a so-called "homeostatic" normal stress level [Humphrey 2000], and that they actively remodel in order to restore their homeostatic stress to this level. Improved understanding over the last several decades has led to the recognition of several mechanisms for creating and preserving this homeostatic stress in the face of hypertension, remodeling, aging, residual stresses, etc.

It has been concluded that collagen types I and III are deposited oriented according to stresses and/or strains experienced by the wall at the time of deposition, and they are deposited with a pre-existing internal stretch. Proper expressions for the orientation of collagen fibers and their so-called "pre-stretch" is a subject of ongoing study. Studies suggest the extracellular matrix structure regulates arterial strain in the long term, and smooth muscle tone acutely modifies residual strain [Zeller 1998]. A satisfactory model quantifying these behaviors remains elusive.

Material properties for constitutive equations and kinetic parameters for evolution equations describing fiber remodeling were measured for mouse arteries *ex vivo* in [Gleason 2007], extending work that was presented in [Humphrey(2) 2002].

1.4.2 Fiber reorientation

A somewhat recent advance in continuum modeling of arteries is the incorporation of various effects of collagen fibers in the artery wall. Current research has been directed toward understanding how the tissue updates its fiber properties (fiber direction, strength, or numbers of cells) based on mechanical stimuli. These kinds of developmental changes occur at a timescale of months, much longer than the one-second timescale of the cardiac cycle. Since the actual timescales of the changes being modeled is unknown, it is common to consider theories of fiber reorientation without specification of a timescale, and to connect only beginning and/or end point configurations with clinical observations. (When a timescale is used, it is typically the lifetime of collagen fibers, about 70 days.)

These phenomena be modeled as aging, healing, pathogenesis, or simple maintenance; and it can measure changes to arteries under hypertension, disease, surgery, or medical management.

1.4.3 Transversely isotropic fibers

Recent research suggests fibers in arteries can be modeled as having "preferred" directions. The preferred direction may change with time or stress. The overall tissue response can be modeled as isotropic, consisting of multiple fiber families. There appear to be multiple preferred directions in arteries. The angle of these directions changes through the thickness, with deeper fibers being more circumferentially oriented, and superficial layers having fibers that are more axially oriented. (See Figure **??**.) In [Holzapfel 2000], the author presents the "Gasser model," a theoretical formulation of two families of fibers perfectly aligned in directions at a specified angle γ from the circumferential. The model

assumes an incompressible hyperelastic arterial wall with a strain energy function defined by

$$\Psi(\boldsymbol{C}) = \frac{\mu}{2}(\bar{I}_1 - 3) + \sum_{i=4,6} \frac{k_1}{2k_2}\left[\exp\left(k_2(\bar{I}_i - 1)^2\right) - 1\right] ,$$

with material constants k_1 and k_2 and invariants

$$\begin{aligned} \bar{I}_1 &= \operatorname{tr} \bar{\boldsymbol{C}} , \\ \bar{I}_4 &= \hat{\boldsymbol{a}}_0 \cdot \bar{\boldsymbol{C}}\hat{\boldsymbol{a}}_0 , \text{ and} \\ \bar{I}_6 &= \hat{\boldsymbol{b}}_0 \cdot \bar{\boldsymbol{C}}\hat{\boldsymbol{b}}_0 . \end{aligned} \tag{1}$$

The symbol $\bar{\boldsymbol{C}} = J^{-2/3}\boldsymbol{F}^{\mathsf{T}}\boldsymbol{F}$ represents the isochoric part of the deformation tensor, and $\hat{\boldsymbol{a}}_0$ and $\hat{\boldsymbol{b}}_0$ are the directions of the fiber families in the reference configuration. The fibers are assumed to act only under tension, so the $\bar{I}_4$ and $\bar{I}_6$ terms are ignored if they are less than 1. With this formulation, the authors formulate a complete theory of fiber-reinforced hyperelastic solids. In [Kroon 2007], the authors use this formulation in a structure-based saccular aneurysm model allowing fiber reorientation.

1.4.4 Collagen turnover models

Humphrey and Taber propose, in [Humphrey 2000], that growth[4] in arteries is based on arteries remodeling their geometry to restore to normal levels, both the circumferential wall stress and wall shear stress due to blood flow. It is thought that the remodeling itself can create, as a byproduct, enlargement of a weakened artery wall into an aneurysm.

[4] The authors define *growth* as the addition of mass, independent of accompanying deformation. This is to be distinguished from *enlargement*, which describes an increase in the volume of blood the aneurysm can surround. In the current work, I use the same definitions.

The artery wall is modeled in [Baek 2006] as a membrane by terms W^k in the strain energy function—terms which provide for collagen production and removal.

$$\begin{aligned} w(t) &= \sum_{k=1,2} \Big(\quad \text{initial} \quad + \quad \text{historical} \quad \Big) \\ &= \sum_{k=1,2} \Big(\quad \frac{M^k(0)}{\rho} Q^k(t) W^k(0,t) \quad + \quad \int_0^t \frac{m^k(\tau)}{\rho} q^k(t-\tau) W^k(\tau,t)\, d\tau \quad \Big) \end{aligned}$$

"Initial stress" refers to any stresses present at time 0, when computation begins. The initial mass fraction of the k-th constituent is $M^k(0)/\rho$.[5] The decay term $Q^k(t-0)$ mitigates the initial stress of the k-th constituent to simulate the gradual turnover (particularly, the removal) of collagen present at time 0. The stress $W^k(0,t)$ is the stress at the current time t of the collagen present at the initial time 0.

"Historical stress" refers to the stress developed during aneurysm growth, from time 0 to the current time t. It uses the same format as the initial stress term—it has a volume term $m^k(\tau)/\rho$, a decay term $q^k(t-\tau)$, and a stress term $W^k(\tau,t)$. The stress term $W^k(\tau,t)$ is the stress at the current time t of the collagen deposited at time τ.

Postulating an initial weak section of an otherwise healthy straight cylindrical artery, the authors observe the changes in geometry and thickness (volume per unit area) due to turnover of fibrous constituents. "Old" fibers, which may be under high stress (or low stress), are removed by the body and replaced with "new" fibers, under their initial pre-stress. The material thus becomes inelastic. See [Humphrey 2000]. The amounts of "new" versus "old" fibers may differ. Humphrey, *et al.* believe these changes are realistic, measurable *in vivo*, and contribute an attributable risk of aneurysm enlargement.

[5] The artery wall is modeled as a membrane; volume and thickness are computed during postprocessing.

It is believed that arteries remodel according to the stress they feel on the cardiac timescale, and also the time rates of stress. That is, if $\boldsymbol{S}_{\text{cardiac}}$ is some sort of stress average felt by the artery and $\boldsymbol{S}_{\text{FSI}}$ is a stress due to short-term blood dynamics, then $\boldsymbol{S}_{\text{cardiac}}$ may depend on $\boldsymbol{S}_{\text{FSI}}$, $\dot{\boldsymbol{S}}_{\text{FSI}}$, $\ddot{\boldsymbol{S}}_{\text{FSI}}$, etc. A proper rule for this dependence is not known.

1.5 Highlights

1. A new growth and remodeling formulation in a 3D solid mechanics model using isogeometric analysis is developed.

2. It utilizes subject-specific geometries from clinical image data and for application to disease progression *in vivo*.

3. It implements realistic fiber microstructure.

4. It proposes a Winkler foundation term to describe the effect of basal tone and tethering of arteries to external organs.

5. It proposes a rate-dependent inelastic model of aneurysm growth.

6. It identifies parallels between mathematical properties of the model and clinical diagnoses.

Chapter 2

Solid mechanics

I use continuum mechanics to describe the motion of artery walls in humans. I assume artery walls are a continuous medium whose motion is dictated by the forces applied and internal stresses.

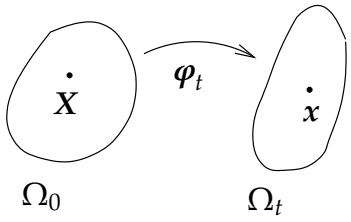

Figure 8: $\boldsymbol{\varphi}_t : \Omega_0 \to \Omega_t$.

Biological tissues *in vivo* change mass. While most mass increase occurs during adolescence, change of mass in adults is an important indicator of health. This is a long timescale process on the order of weeks to years, a similar timescale to the progression of aneurysm disease.

I do not explicitly model the influx of nutrients or reuptake of cells. My simulations of enlargement of aneurysms allow volume changes at constant density—mass is not conserved. When mass increases, I say there is "growth"; and when it decreases, "decay." The term "enlargement" will refer to deformation which increases the apparent size of the simulated aneurysm. Enlargement is independent of growth.

I use growth kinematics to derive my constitutive equations. It turns out they are largely unchanged from kinematic setups without growth. Conservation of mass has a simple change, and the conservation of linear and angular momentum are unchanged. I do not consider thermodynamics or entropy.

The mechanics of a growing mass are well known. For example, [Lubarda 2002] presents a thorough treatment, beginning with the balance laws. I choose not to dupli-

cate that effort. Here I present a brief treatment in the vein of [Lubarda 2002], to establish notation and state my governing equations.

2.1 Notation

Suppose there is a body $\mathcal{B}$ of a continuous material that occupies the region $\Omega_0 \subseteq \mathbb{R}^3$ at time $t = 0$, and that $\boldsymbol{\varphi}_t : \Omega_0 \to \Omega_t$ is a motion of the body to a (possibly different) region $\Omega_t \subseteq \mathbb{R}^3$ at time t, for $t \in [0, T]$. See Figure 8.

As usual, write $\boldsymbol{x} = \boldsymbol{\varphi}_t(\boldsymbol{X}) = \boldsymbol{\varphi}(\boldsymbol{X}, t)$. Assume $\boldsymbol{\varphi}_0 : \Omega_0 \to \Omega_0$ is the identity map. Write the velocity $\boldsymbol{v}$ as $\boldsymbol{v}(\boldsymbol{x}, t) = \left(\frac{d}{dt}|_X\right)\boldsymbol{\varphi}$, where $\frac{d}{dt} = \frac{d}{dt}|_X$ is the material time derivative.

The deformation tensor $\boldsymbol{F}$ is $\boldsymbol{F} = \nabla_X \varphi(\boldsymbol{X}, t) = \frac{\partial x}{\partial X}$. The determinant $J = \det \boldsymbol{F}$. The right Cauchy–Green deformation tensor is $\boldsymbol{C} = \boldsymbol{F}^{\mathsf{T}}\boldsymbol{F}$. The Second Piola–Kirchhoff stress is $\boldsymbol{S}$. Cauchy stress is $\boldsymbol{\sigma}$. The Green–Lagrange strain tensor $\boldsymbol{E} = \frac{1}{2}\left(\boldsymbol{F}^{\mathsf{T}}\boldsymbol{F} - \boldsymbol{I}\right)$. The strain tensor $\boldsymbol{e} = \frac{1}{2}\left(\boldsymbol{F}\boldsymbol{F}^{\mathsf{T}} - \boldsymbol{I}\right)$.

2.2 Balance laws for a growing mass

Suppose that for each material point $\boldsymbol{X}$, the material's mass grows at some rate $R \in \mathbb{R}$. The value of R may change over time: $R = R(\boldsymbol{X}, t)$. If $R > 0$ there is growth, and if $R < 0$ there is decay. Though the material grows, it is assumed to be a continuous material in space. Therefore, every spatial point in the body at time t is assumed to have existed at time 0. All calculations, then, can be expressed appropriately in material or spatial coordinates. In spatial coordinates, I would use a lowercase letter: $r = r(\boldsymbol{x}, t) \in \mathbb{R}$. In the case of conservation of mass, $r \equiv 0$.

2.2.1 Continuity equation

Write dm for a differential unit of mass, and dv and dV as a differential volume elements for the current and material volume, respectively. Define r such that

$$\frac{d}{dt}\, dm = r\, dv\,,$$

and $\rho = dm/dv$ as the current mass density. Then

$$\begin{aligned} r\, dv &= \frac{d}{dt}(dm) \\ &= \frac{d}{dt}(\rho\, dv) \\ &= \left(\frac{d}{dt}\rho\right) dv + \rho\, \frac{d}{dt}\, dv\,. \end{aligned} \tag{2}$$

Volume growth is proportional to the divergence of the velocity field:

$$\frac{d}{dt}\, dv = (\nabla_{\boldsymbol{x}} \cdot \boldsymbol{v})\, dv\,. \tag{3}$$

Combining (2) and (3) into

$$\frac{d\rho}{dt}\, dv + \rho\, (\nabla_{\boldsymbol{x}} \cdot \boldsymbol{v})\, dv = r\, dv\,,$$

I achieve the continuity equation for a growing mass:

$$\frac{d\rho}{dt} + \rho\, (\nabla_{\boldsymbol{x}} \cdot \boldsymbol{v}) = r\,. \tag{4}$$

The current volume density ρ is assumed to be nearly constant for all time, for all points, so $\frac{d\rho}{dt} \approx 0$. My numerical formulation assumes a nearly incompressible material, with a very high Poisson's ratio. This is used as a simplifying assumption. Healthy artery walls appear to keep a constant density during changes in fibrous structure. In aneurysm development, artery walls appear to first reduce their density (loss of media layer), then

increase it (increased collagen production), even as they become thin (due to degradation) or thick (due to inflammation). Exploration of density of diseased tissue is not a feature of this work.

Because $dv = J\,dV$, if I take R such that $r\,dv = R\,dV$, I have $rJ = R$.

2.2.2 Reynolds Transport Theorem

Consider a quantity q in the current configuration. The Reynolds Transport Theorem is

$$\frac{d}{dt}\int_{\Omega_t} \rho q\, dv \;=\; \int_{\Omega_t} \left(\rho \frac{dq}{dt} + rq\right)\, dv\,. \tag{5}$$

2.2.3 Balance of linear momentum

Growth does not affect linear momentum.

For a body force $\boldsymbol{b}$, surface normal $\boldsymbol{n}$, and Cauchy stress $\boldsymbol{\sigma}$, Euler's first law of motion for a growing mass is

$$\frac{d}{dt}\int_{\Omega_t} \rho \boldsymbol{v}\, dv \;=\; \int_{\partial\Omega_t} \boldsymbol{\sigma}\cdot\boldsymbol{n}\, da \;+\; \int_{\Omega_t} \rho \boldsymbol{b}\, dv \;+\; \int_{\Omega_t} r\boldsymbol{v}\, dv\,. \tag{6}$$

But by the Reynolds Transport Theorem with the velocity as q,

$$\frac{d}{dt}\int_{\Omega_t} \rho \boldsymbol{v}\, dv \;=\; \int_{\Omega_t} \left(\rho \frac{d\boldsymbol{v}}{dt} + r\boldsymbol{v}\right)\, dv\,. \tag{7}$$

The integrands of (6) and (7) which contain the growth term cancel, giving the usual linear momentum equations for a material without growth:

$$\begin{aligned}\int_{\Omega_t} \rho\, \frac{d\boldsymbol{v}}{dt}\, dv \;&=\; \int_{\partial\Omega_t} \boldsymbol{\sigma}\cdot\boldsymbol{n}\, da \;+\; \int_{\Omega_t} \rho\boldsymbol{b}\, dv \\ \rho\, \frac{d\boldsymbol{v}}{dt} &= \nabla_{\boldsymbol{x}}\cdot\boldsymbol{\sigma} + \rho\boldsymbol{b}\,.\end{aligned} \tag{8}$$

Writing $\boldsymbol{F} = \nabla_{\boldsymbol{X}} \boldsymbol{\varphi}_t = \frac{\partial \boldsymbol{x}}{\partial \boldsymbol{X}}$, $\rho_0 = \rho J$, and $R = rJ$, Euler's first law in material coordinates reads

$$\begin{aligned}\frac{d}{dt}\int_{\Omega_0} \rho_0 \boldsymbol{v}\, dV &= \int_{\partial\Omega_0} \boldsymbol{FSN}\, dA + \int_{\Omega_0} \rho_0 \boldsymbol{B}\, dV + \int_{\Omega_0} R\boldsymbol{v}\, dV \\ &= \int_{\Omega_0} \nabla_{\boldsymbol{X}} \cdot (\boldsymbol{FS}) + \rho_0 \boldsymbol{B} + R\boldsymbol{v}\, dV\,.\end{aligned}$$

Pulling the derivative inside the integral, and then using the fact $\frac{d}{dt}\rho_0 = \frac{d}{dt}(\rho J) = R$, the left-hand side is

$$\begin{aligned}\frac{d}{dt}\int_{\Omega_0} \rho_0 \boldsymbol{v}\, dV &= \int_{\Omega_0} \Big(\rho_0 \frac{d\boldsymbol{v}}{dt} + \frac{d}{dt}(\rho_0)\boldsymbol{v}\Big)\, dV \\ &= \int_{\Omega_0} \Big(\rho_0 \frac{d\boldsymbol{v}}{dt} + R\boldsymbol{v}\Big)\, dV\,.\end{aligned}$$

Together, they combine to give the balance of linear momentum in material coordinates.

$$\int_{\Omega_0} \rho_0 \frac{d\boldsymbol{v}}{dt}\, dV = \int_{\Omega_0} \nabla_{\boldsymbol{X}} \cdot (\boldsymbol{FS})\, dV + \int_{\Omega_0} \rho_0 \boldsymbol{B}\, dV + \int_{\Omega_0} R\boldsymbol{v}\, dV\,,$$

or

$$\rho_0 \frac{d\boldsymbol{v}}{dt} = \nabla_{\boldsymbol{X}} \cdot (\boldsymbol{FS}) + \rho_0 \boldsymbol{B}\,. \tag{9}$$

2.2.4 Balance of angular momentum

Growth does not affect angular momentum.

In integral form, Euler's second law of motion for a growing mass reads,

$$\int_{\Omega_t} \frac{d}{dt}(\boldsymbol{x} \times \rho \boldsymbol{v})\, dv = \int_{\Omega_t} \rho\, (\boldsymbol{x} \times \boldsymbol{b}) + r\, (\boldsymbol{x} \times \boldsymbol{v})\, dv + \int_{\partial\Omega_t} (\boldsymbol{x} \times \boldsymbol{\sigma}) \cdot \boldsymbol{n}\, da\,. \tag{10}$$

Master balance law:

$$\frac{d}{dt}\,\alpha = \frac{\partial}{\partial t}\,\alpha + \nabla_{\boldsymbol{x}} \cdot (\alpha \boldsymbol{v}) = \beta + \nabla_{\boldsymbol{x}} \cdot \boldsymbol{\gamma}\ .$$

$$\frac{d}{dt}\int\limits_{\Omega_t} \alpha\ dv = \int\limits_{\Omega_t} \beta\ dv + \int\limits_{\partial\Omega_t} \boldsymbol{\gamma}\,\boldsymbol{n}\ da\ .$$

	α quantity	β source	γ flux
continuity (4)	ρ	r	$\mathbf{0}$
momentum (spatial) (6)	$\rho \boldsymbol{v}$	$\rho \boldsymbol{b} + r\boldsymbol{v}$	$\boldsymbol{\sigma}$
angular momentum (10)	$\boldsymbol{x} \times \rho \boldsymbol{v}$	$\rho\,(\boldsymbol{x} \times \boldsymbol{b}) + r\,(\boldsymbol{x} \times \boldsymbol{v})$	$\boldsymbol{x} \times \boldsymbol{\sigma}$

Table 9: Master balance law. This is the usual form, when conservation of mass holds ($r \equiv 0$). In this form, it appears momentum depends on growth r, but the Reynolds Transport Theorem shows momentum does not depend on growth.

Again by the Reynolds Transport Theorem, with $(\boldsymbol{x} \times \boldsymbol{v})$ as q, the above becomes the usual momentum equation

$$\int\limits_{\Omega_t} \rho\,\frac{d}{dt}(\boldsymbol{x} \times \boldsymbol{v})\ dv\ = \int\limits_{\Omega_t} \rho\,(\boldsymbol{x} \times \boldsymbol{b})\ dv\ + \int\limits_{\partial\Omega_t} (\boldsymbol{x} \times \boldsymbol{\sigma}) \cdot \boldsymbol{n}\ da\ . \tag{11}$$

Therefore I still achieve symmetry $\boldsymbol{\sigma} = \boldsymbol{\sigma}^{\mathsf{T}}$ of the Cauchy stress.

2.2.5 Master balance law

The above equations can be summarized in a master balance law. It is interesting to note how growth disrupts the cleanliness of this representation. Table 9 shows the usual spatial form of the master balance law, and the integrands which create each balance law. The usual form of the master balance law obscures the lack of dependence on growth for momentum.

Alternatively, consider Table 10. In that table, I have incorporated mass density into the master balance law (by simply applying the Reynolds Transport Theorem). After

Transported master balance law:

$$\rho \frac{d}{dt} \eta = \rho \xi + \nabla_{\boldsymbol{x}} \cdot \boldsymbol{\gamma} \,.$$

$$\int_{\Omega_t} \rho \frac{d}{dt} \eta \, dv = \int_{\Omega_t} \rho \, \xi \, dv + \int_{\partial \Omega_t} \boldsymbol{\gamma} \, \boldsymbol{n} \, da \,.$$

	$\eta = \alpha / \rho$ quantity	$\xi = \beta - r\eta$ source	$\boldsymbol{\gamma}$ flux
(continuity)	1	0	$\mathbf{0}$
momentum (spatial) (8)	$\boldsymbol{v}$	$\boldsymbol{b}$	$\boldsymbol{\sigma}$
angular momentum (11)	$\boldsymbol{x} \times \boldsymbol{v}$	$(\boldsymbol{x} \times \boldsymbol{b})$	$\boldsymbol{x} \times \boldsymbol{\sigma}$

Table 10: Alternative form for a master balance law. Linear and angular momentum are revealed to be independent of growth. Interestingly, in this form the continuity equation reads $0 = 0 + 0$.

having done so, the master balance law reveals the lack of dependence on r. The continuity equation in this form becomes trivial.

2.3 Boundary-value problem statements

Here I state the initial–boundary-value problem in general terms. To state the aneurysm problem, I begin with linear momentum. I assume a quasi-static material, and end with the usual large deformation kinematics setup for a solid subject to Dirichlet, Neumann, and body force conditions. The strong and weak formulations are stated here. The Galerkin form is given in § 4.1 below. Additional specifics for each simulation will be given together with the simulation results, in Chapters 6.

2.3.1 Quasi-static assumption

The timescale of growth and remodeling is long, much longer than the action of intertial or transient effects. At each timestep, I assume the material has reached equilibrium, and therefore has no velocity. I do not model acute injury, or motion or acceleration of the person's head. Despite the material's velocity being zero, it undergoes motion, because its material properties evolve from timestep to timestep. The solid is said to be "quasi-static"[1]. That is,

$$\boldsymbol{v} = \dot{\boldsymbol{\varphi}} \equiv 0 \,.$$

Therefore, linear momentum (8) and (9) become the familiar

$$\nabla_{\boldsymbol{x}} \cdot \boldsymbol{\sigma} + \rho \boldsymbol{b} = 0 \,,$$

$$\nabla_{\boldsymbol{X}} \cdot (\boldsymbol{F}\boldsymbol{S}) + \rho_0 \boldsymbol{B} = 0 \,. \tag{12}$$

The Cauchy stress is $\boldsymbol{\sigma}$, the Second Piola–Kirchhoff stress is $\boldsymbol{S}$, mass density in material coordinates is $\rho_0 = \rho J$, and body forces are $\boldsymbol{b} = \boldsymbol{b}(\boldsymbol{x}, t)$ and $\boldsymbol{B} = \boldsymbol{B}(\boldsymbol{X}, t) = \boldsymbol{b}(\boldsymbol{x}, t) \circ \boldsymbol{\varphi}(\boldsymbol{X}, t)$. Gravitational forces will be neglected, but later on (in §3.9) I will introduce a Winkler body force.

2.3.2 Strong form

The traction conditions are as in Figure 11. The interior surface of the *in vivo* artery is assumed to feel the equivalent effect of a constant, average blood pressure p_{BP}, and the outer surface is assumed to feel the pressure p_{brain} of the cerebral spinal fluid. Both these pressures are maintained in the spatial description. (They are follower forces.)

[1] This is a common assumption for long-term effects. In my simulations, including dynamic effects improved convergence.

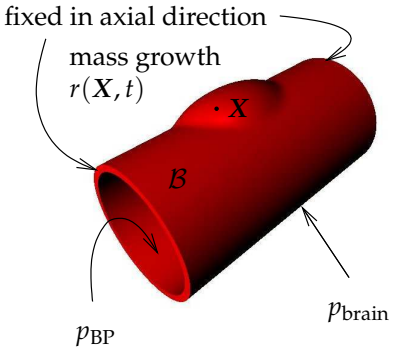

Figure 11: The body $\mathcal{B}$ in the growth problem. The material is a continuous solid with a growing mass. Internal and external pressures are shown. The simulation is quasi-static, growth being on a timescale of weeks to decades.

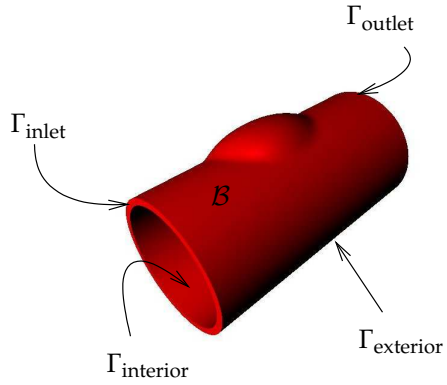

Figure 12: Definitions of the boundary subsets of the artery.

Specifically, define sets comprising the boundary $\partial\mathcal{B} = \partial\Omega_0$ as in Figures 11 and 12:

$$\begin{aligned}
\Gamma_g &= \Gamma_{g0} = \Gamma_{\text{inlet}} \cup \Gamma_{\text{outlet}} \\
\Gamma_h &= \Gamma_{h0} = \Gamma_{\text{interior}} \cup \Gamma_{\text{exterior}} \\
\Gamma_{gt} &= \boldsymbol{\varphi}_t(\Gamma_{g0}) \\
\Gamma_{ht} &= \boldsymbol{\varphi}_t(\Gamma_{h0}) \,,
\end{aligned} \tag{13}$$

and define essential and natural boundary conditions

$$\begin{aligned}
g(\boldsymbol{X}, t) &\equiv \text{const in axial direction}, && \text{on } \Gamma_g \\
h(\boldsymbol{X}, t) &\equiv p_{\text{BP}}, && \text{on } \Gamma_{\text{interior}} \\
h(\boldsymbol{X}, t) &\equiv p_{\text{brain}}, && \text{on } \Gamma_{\text{exterior}} \,.
\end{aligned} \tag{14}$$

Then for each t in $[0, T]$, the strong form of the boundary value problem is

(GNR, S) Given g, h as above, find $\boldsymbol{\varphi} \in H^1(\Omega_0)$ such that

$$\begin{aligned}
&\nabla_{\boldsymbol{x}} \cdot \boldsymbol{\sigma} + \rho \boldsymbol{b} = 0 && \text{in } \Omega_t \\
&\boldsymbol{\varphi} \equiv g && \text{on } \Gamma_{gt} \\
&\boldsymbol{\sigma}\boldsymbol{n} = h\boldsymbol{n} && \text{on } \Gamma_{ht} \,.
\end{aligned}$$

It is important to observe that because the natural configurations evolve with t, the material properties embedded in $\boldsymbol{\sigma}$ are time-dependent, and so the boundary value problems also have a time dependence.

2.3.3 Weak form

Define the "space" of candidate solutions and the space of test functions to be

$$\mathcal{S} = \{\boldsymbol{\varphi} \in H^1(\Omega_0) : \ \boldsymbol{\varphi} \restriction \Gamma_g \equiv g\} \ \text{ and} \tag{15}$$

$$\mathcal{V} = \{\boldsymbol{\psi} \in H^1(\Omega_0) : \ \boldsymbol{\psi} \restriction \Gamma_g \equiv 0\} \, . \tag{16}$$

Multiplying the constitutive equation (12),

$$0 = \nabla_{\boldsymbol{X}} \cdot (\boldsymbol{F}\boldsymbol{S}) + \rho_0 \boldsymbol{B} \, ,$$

by a test function $\boldsymbol{\psi}$ and integrating by parts gives

$$\begin{aligned} 0 &= \int_{\Omega_0} \boldsymbol{\psi} \cdot \left(\nabla_{\boldsymbol{X}} \cdot (\boldsymbol{F}\boldsymbol{S}) + \rho_0 \boldsymbol{B} \right) \, dV \\ &= -\int_{\Omega_0} (\nabla_{\boldsymbol{X}} \boldsymbol{\psi}) : (\boldsymbol{F}\boldsymbol{S}) \, dV + \int_{\partial\Omega_0} \boldsymbol{\psi} \cdot (\boldsymbol{F}\boldsymbol{S}) \boldsymbol{N} \, dA \ + \int_{\Omega_0} \boldsymbol{\psi} \cdot \rho_0 \boldsymbol{B} \, dV \\ &= -\int_{\Omega_0} (\nabla_{\boldsymbol{X}} \boldsymbol{\psi}) : (\boldsymbol{F}\boldsymbol{S}) \, dV + \int_{\Gamma_h} \boldsymbol{\psi} \cdot Jh\boldsymbol{F}^{-\mathsf{T}} \boldsymbol{N} \, dA \ + \int_{\Omega_0} \boldsymbol{\psi} \cdot \rho_0 \boldsymbol{B} \, dV \, . \end{aligned} \tag{17}$$

The outward-pointing unit normal in the reference configuration is $\boldsymbol{N}$, and $J = \det \boldsymbol{F}$. The area element dA is related to da via the familiar relation $\boldsymbol{n} \, da = J\boldsymbol{F}^{-\mathsf{T}} \boldsymbol{N} \, dA$.

In index notation[2]—where repeated indices are summed over values 1, 2, 3—equation (17) becomes

$$0 = -\int_{\Omega_0} \boldsymbol{\psi}_{i,J} \, \boldsymbol{F}_{iI} \boldsymbol{S}_{IJ} \, dV + \int_{\Gamma_h} \boldsymbol{\psi}_i \, Jh\boldsymbol{F}^{-\mathsf{T}}_{iI} \boldsymbol{N}_I \, dA \ + \int_{\Omega_0} \boldsymbol{\psi}_i \, \rho_0 \boldsymbol{B}_i \, dV. \tag{18}$$

The comma index notation indicates a derivative: $\boldsymbol{\psi}_{i,J} = \partial \boldsymbol{\psi}_i / \partial \boldsymbol{X}_J$.

[2] The symbol J as a subscript is an index.

The weak formulation then becomes the task

$$\text{(GNR, W)} \left\{ \begin{array}{l} \text{Given } g,\ h, \text{ as above, find } \boldsymbol{\varphi} \in \mathcal{S} \text{ such that for all } \boldsymbol{\psi} \in \mathcal{V}\ , \\ \quad \left(\boldsymbol{\psi}_{i,J},\ \boldsymbol{F}_{iI}\boldsymbol{S}_{IJ}\right)_{\Omega_0} = \left(\boldsymbol{\psi}_i,\ Jh\boldsymbol{F}_{iI}^{-\mathsf{T}}\boldsymbol{N}_I\right)_{\Gamma_h} + \left(\boldsymbol{\psi}_i,\ \rho_0\boldsymbol{B}_i\right)_{\Omega_0}\ . \end{array} \right.$$

Chapter 3

Constitutive model

In this chapter, I shall discuss the manner in which I define stress.

I begin with a hyperelastic model which roughly describes the behavior of soft tissue under normal, healthy loading conditions. On top of that, I add inelastic properties which describe the behavior of the collagen fibers inside of artery walls under diseased, unhealthy conditions.

To describe aneurysm disease, I developed a rate-dependent inelastic continuum model for artery tissue. It has several guiding principles.

One guiding principle of this work is collagen turnover cannot by itself explain cranial aneurysms: aneurysm development can happen at timescales much faster (days–weeks) and also much slower (years) than the timescale of the body's replacement of collagen fibers (months). Instead of the theory of turnover, usually modeled as "fading memory," a theory of inelasticity is implemented. Other guiding principles are the following.

- Collagen fibers are the predominant load-bearing constituent of arteries.
- While arteries have multiple distinct layers, modeling them as a single-layered homogeneous material is sufficiently accurate.
- Non-collagen-fiber material can be modeled as a soft elastic material.
- Disease states can be modeled as irreversible processes instead of a return to homeostasis.
- Existing biomechanical theories for saccular aneurysms have limitations.

3.1 Fiber direction

Collagen fibers arrange themselves in layers, with each layer having symmetrically-arranged fibers pointing in preferred directions. Fiber direction has been studied exensively in the literature, but there has been little connection shown between fiber direction profiles and aneurysm behavior. My own studies of fiber direction are consistent with this, and the model I present is not very sensitive to fiber direction. For that reason, I use a simple fiber direction model. I elaborate on the profile I choose ($\pm 45^{\circ}$ from axial) in §5.9.

The fiber direction profile is prescribed as a vector field $\boldsymbol{M} = \boldsymbol{M}(\boldsymbol{X})$. $\|\boldsymbol{M}\| = 1$ everywhere. Also, λ is the stretch ratio in the fiber direction:

$$\boldsymbol{F} = \boldsymbol{\nabla \varphi}$$

$$\boldsymbol{m} = \boldsymbol{F}\boldsymbol{M}$$

$$\lambda = \|\boldsymbol{m}\| \, .$$

3.2 Elastic strain

The material model used is presented as a strain energy function. The existence of a strain energy function $w = w(t) = w(\boldsymbol{X}, t)$ comes from the hyperelastic assumption [Gonzalez 2008]. Here the notation is

$$\boldsymbol{S} = \frac{\partial w}{\partial \boldsymbol{E}} = 2 \, \frac{\partial w}{\partial \boldsymbol{C}} \, .$$

The strain energy function comes in two major parts. One is the background material's energy, and the other is the fiber energy. The first part's purpose is to represent the stiffness of the "background material" of the artery.

There is considerable debate in the literature over which strain energy functions are the most appropriate to use. For this work, the background material is the neo-Hookean

formula of equation (20) from Ciarlet [Simo, Hughes 1998], and collagen is the exponentially-stiffening material of (21), postulated in [Baek 2006]. Straightforward strain energy functions are used here; the purpose of this work is to investigate inelastic properties, not elastic properties.

I separate the constitutive model for arteries into two parts: that of a soft hyperelastic volumetric background material W_{vol} from [Ciarlet 1988], and exponentially-stiffening one-dimensional collagen fibers W_{fib} from [Baek 2006].

As is common modeling assumption, I suppose there are two families, numbered $k = 1$ and $k = 2$. A fiber from family k will be referred to as a k-fiber. The fiber strain energy W^k is a function of one variable, the square of the elastic stretch ratio in the fiber direction. Write $\boldsymbol{M}^k$ for the fiber direction in material coordinates, and $\boldsymbol{m}^k(t) = \boldsymbol{F}(t)\boldsymbol{M}^k$ for its push-forward into current coordinates.

The overall stretch ratio of a fiber is denoted like this:

$$\lambda^2 = \boldsymbol{m} \cdot \boldsymbol{m} = (\boldsymbol{F}\boldsymbol{M}) \cdot (\boldsymbol{F}\boldsymbol{M}) = \boldsymbol{M} \cdot \boldsymbol{F}^{\mathsf{T}}\boldsymbol{F}\boldsymbol{M} = \boldsymbol{M} \cdot \boldsymbol{C}\boldsymbol{M} \, .$$

The stretch ratio is decomposed into an elastic amount and an irreversible (inelastic) amount:

$$\lambda^k = \lambda^k_{\text{el}} \, \lambda^k_{\text{irr}} \, .$$

The elastic amount can be determined by dividing:

$$\lambda^k_{\text{el}} = \lambda^k / \lambda^k_{\text{irr}} \, .$$

The meaning of irreversible strain will be discussed shortly (in sections 3.6, 3.7, and 3.8). Here, I describe the material's elastic properties.

A lowercase w is used for the overall strain energy, to avoid confusion with component energy terms W.

$$w = W_{\text{vol}} + \sum_{k=1,2} W^k \tag{19}$$

$$W_{\text{vol}} = W_{\text{vol}}(J) = \lambda_{\text{Lamé}}\Big(\frac{1}{4}(J^2-1) - \frac{1}{2}(\ln J)\Big) + \mu_{\text{Lamé}}(\operatorname{tr}\boldsymbol{E} - \ln J) \tag{20}$$

$$W^k = W_{\text{fib}}\big((\lambda^k_{\text{el}})^2\big) = c_1\Big(\exp\Big[c_2\big((\lambda^k_{\text{el}})^2-1\big)^2\Big] - 1\Big)\,. \tag{21}$$

For simplicity, the k indicating fiber direction will often be dropped. Constants c_1 and c_2 are material parameters. Their values are given together with the results. The Green–Lagrange strain tensor $\boldsymbol{E}$ is $\frac{1}{2}\big(\boldsymbol{F}^{\mathsf{T}}\boldsymbol{F} - \boldsymbol{I}\big)$.

Because fiber strain energy depends only on the stretch ratio in the fiber direction—there are no cross-sectional or shear effects—its stress tensor is uniaxial:

$$\begin{aligned}\boldsymbol{S}_{\text{fib}} &= 2\frac{\partial W_{\text{fib}}}{\partial \boldsymbol{C}} = 2\,\frac{dW_{\text{fib}}(\lambda^2_{\text{el}})}{d(\lambda^2_{\text{el}})}\,\frac{\partial\lambda^2_{\text{el}}}{\partial\lambda^2}\,\frac{\partial\lambda^2}{\partial\boldsymbol{C}} = \Big[\,2\,W'_{\text{fib}}(\lambda^2_{\text{el}})\,\frac{1}{\lambda^2_{\text{irr}}}\,\Big]\,\frac{\partial\lambda^2}{\partial\boldsymbol{C}} \\ &= \Big[\,\underbrace{2\,W'_{\text{fib}}(\lambda^2_{\text{el}})}_{s_{\text{el}}}\,\frac{1}{\lambda^2_{\text{irr}}}\,\Big](\boldsymbol{M}\otimes\boldsymbol{M}) = \Big[\frac{s_{\text{el}}}{\lambda^2_{\text{irr}}}\Big](\boldsymbol{M}\otimes\boldsymbol{M})\,.\end{aligned} \tag{22}$$

This is thanks to the convenient well-known observation

$$\frac{\partial}{\partial\boldsymbol{C}}\lambda^2 = \frac{\partial}{\partial\boldsymbol{C}}(\boldsymbol{M}\cdot\boldsymbol{C}\boldsymbol{M}) = (\boldsymbol{M}\otimes\boldsymbol{M})\,.$$

Setting $s_{\text{el}} = 2\,W'_{\text{fib}}(\lambda^2_{\text{el}})$ is a notational convenience designed to reiterate that s_{el} depends only on *elastic* quantities.

3.3 Isotropic, hyperelastic background material

The background material is a soft volumetric material whose purpose is to maintain the artery's thickness during inflation. It repesents the non-collagen portions of the artery.

This choice could be replaced with a two-dimensional membrane material. That would alleviate several struggles with the simulation that have nothing to do with the constitutive model I present. Namely, using a thick-walled material creates opportunities to deal with bending stiffness, locking problems, and Newton convergence issues where a deformation with $\det \boldsymbol{F} < 0$ is attempted. I chose to use a thick-walled material to pave the way for future research in modeling inflammation, atherslcerosis, and other thickness-related processes in arteries.

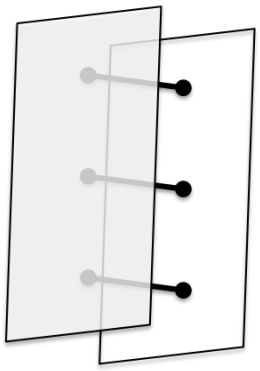

Figure 13: Physical interpretation of fiber Cauchy stress. Fibers should be thought of as individual proteins connecting two infinitesimal parallel plates. Fiber Cauchy stress does not change with changes to the cross-sectional area of the plates, or to irreversible strain in the fibers.

3.4 One dimensional, independently-acting collagen fibers

As I have seen, in this theory, fiber strain energy and stresses are uniaxial quantities. This definition of Cauchy stress for collagen has a good physical interpretation: that of individual fibers connecting two infinitesimal plates. (See Figure 13.) First, stress depends on elastic strain. Second, irreversible strain λ_{irr} of fibers has no effect on stress. Third, strain normal to the fibers has no effect on stress. That is, expansion and contraction of the infinitesimal plates only changes the (infinitesimal) distance between the cables, not their stress.[1]

[1] This is a modeling assumption. In tissues, as with textiles, perpendicular strains are not entirely decoupled: large strain in one direction leads to a greater stress–strain response in normal directions.

3.5 Derivatives of the strain energy

Here are the expressions for the Second Piola–Kirchhoff tensor $\boldsymbol{S}$ and the elasticity tensor $\mathbb{C}$ for the growth and remodeling timescale as the first and second derivatives of the strain energy function W with respect to $\boldsymbol{C}$.

Continuing the work done in equation 22, the contributions from the fibers $\big($see equation (21)$\big)$ have derivatives

$$\begin{aligned} W'_{\text{fib}}(\lambda^2_{\text{el}}) &= \frac{dW}{d\lambda^2_{\text{el}}} = \frac{d}{d\lambda^2_{\text{el}}}\, c_1 \Big(\exp\left[c_2 \big(\lambda^2_{\text{el}} - 1\big)^2 \right] - 1 \Big) \\ &= c_1 \exp\left[c_2 \big(\lambda^2_{\text{el}} - 1\big)^2 \right] \cdot 2c_2(\lambda^2_{\text{el}} - 1) \qquad (23) \\ \boldsymbol{S}^k_{IJ} = 2\frac{\partial W^k}{\partial \boldsymbol{C}_{IJ}} &= \Big[\, 2\, W'_{\text{fib}}(\lambda^2_{\text{el}})\ \frac{1}{\lambda^2_{\text{irr}}} \,\Big]\ \boldsymbol{M}_I \boldsymbol{M}_J \\ &= 2c_1 e^{c_2(\lambda^2_{\text{el}}-1)^2}\, 2c_2(\lambda^2_{\text{el}} - 1)\ \boldsymbol{M}_I \boldsymbol{M}_J \qquad (24) \\ \mathbb{C}^k_{IJKL} = 2\frac{\partial \boldsymbol{S}^k_{IJ}}{\partial \boldsymbol{C}_{KL}} &= 4c_1 e^{c_2(\lambda^2_{\text{el}}-1)^2}\, 2c_2(\lambda^2_{\text{el}} - 1)\ \boldsymbol{M}_I \boldsymbol{M}_J\, 2c_2(\lambda^2_{\text{el}} - 1)\ \boldsymbol{M}_K \boldsymbol{M}_L \\ &\quad + 4c_1 e^{c_2(\lambda^2_{\text{el}}-1)^2}\, 2c_2 \boldsymbol{M}_I \boldsymbol{M}_J \boldsymbol{M}_K \boldsymbol{M}_L\,. \\ &= 4c_1 \big(4c_2^2\,(\lambda^2_{\text{el}} - 1)^2 + 2c_2\big)\, e^{c_2(\lambda^2_{\text{el}}-1)^2}\ \boldsymbol{M}_I \boldsymbol{M}_J \boldsymbol{M}_K \boldsymbol{M}_L\,. \qquad (25) \end{aligned}$$

3.6 Aneurysm enlargement as irreversible strain

I choose to model the enlargement of aneurysms using a rate-sensitive inelastic theory. The main reason for doing so is that I do not believe, as some researchers do [Baek 2006, Kroon 2007], that disease is well-modeled as a (perhaps flawed) return to homeostasis. More generally, I believe the predominant theories in the literature cannot account for the etiology of saccular aneurysms. A new approach is needed.

I view disease as *irreversible* alterations in both structure and function of arterial tissue. Arterial tissue behaves elastically within physiologic regimes, and if the tissue is strained above some limit, it undergoes irreversible strain.

3.7 Definition of irreversible strain

A preliminary model I devised uses irreversible strain defined by the following equations.

$$
\begin{aligned}
\text{collagen Cauchy stress tensor:} \quad & \boldsymbol{\sigma}_{\text{fib}} = \sigma\,(\hat{\boldsymbol{m}} \otimes \hat{\boldsymbol{m}}), \quad \hat{\boldsymbol{m}} = \boldsymbol{m}/\|\boldsymbol{m}\| \\
\text{collagen Cauchy stress scalar:} \quad & \sigma = \hat{\boldsymbol{m}} \cdot \boldsymbol{\sigma}_{\text{fib}} \hat{\boldsymbol{m}} \\
\text{elastic strain:} \quad & \lambda_{\text{el}} = \frac{\lambda}{\lambda_{\text{irr}}}\,, \quad \lambda = \|\boldsymbol{m}\| \\
\text{flow rule:} \quad & \dot{\lambda}_{\text{irr}} = \frac{\langle \phi \rangle}{\tau_{\text{relax}}}\,, \quad \phi = \frac{\sigma}{k} - 1\,, \quad \langle x \rangle \equiv \begin{cases} x & x > 0 \\ 0 & x \leqslant 0\,. \end{cases} \\
\text{pseudoelastic limit:} \quad & k = k\big(\sigma, \boldsymbol{x}, t;\ \varphi(\boldsymbol{x}, [0,t])\big) \\
\text{hardening law:} \quad & \dot{k} = \dot{k}_{\text{irr}} + \dot{k}_{\text{les}} \\
\text{irreversible hardening:} \quad & \dot{k}_{\text{irr}} = \dot{\lambda}_{\text{irr}} H_{\text{irr}} \\
\text{lesion onset (softening):} \quad & \dot{k}_{\text{les}} = \dot{k}_{\text{les}}(\boldsymbol{x}, t) \\
& \qquad = H_{\text{les}}(k_{\text{les}} - k^{\infty}_{\text{les}})\,, \quad k^{\infty}_{\text{les}} = k^{\infty}_{\text{les}}(\boldsymbol{x}, t)\,.
\end{aligned}
$$

A few remarks about these modeling choices:

1. I use the notation of a boldface $\boldsymbol{\sigma}$ for the Cauchy stress *tensor*; and a lightface σ for a *scalar* representing Cauchy stress. I often use the scalar when discussing collagen Cauchy stress, especially in Chapters 6–7. This is not such an abuse of notation because collagen fibers are one-dimensional (in my model) and their stress tensor is uniaxial. (See the following remark.)

2. Fibers, as one-dimensional quantities, have no volume. The Cauchy stress, like the 2nd Piola–Kirchhoff stress, is uniaxial:

$$\begin{aligned}
\boldsymbol{\sigma}_{\text{fib}} &= J^{-1}\boldsymbol{F}\boldsymbol{S}_{\text{fib}}\boldsymbol{F}^{\mathsf{T}} \\
&= J^{-1}\boldsymbol{F}\left[\frac{s_{\text{el}}}{\lambda_{\text{irr}}^2}\right](\boldsymbol{M}\otimes\boldsymbol{M})\,\boldsymbol{F}^{\mathsf{T}} = J^{-1}\left[\frac{s_{\text{el}}}{\lambda_{\text{irr}}^2}\right]\boldsymbol{F}\,(\boldsymbol{M}\otimes\boldsymbol{M})\,\boldsymbol{F}^{\mathsf{T}} \\
&= J^{-1}\left[\frac{s_{\text{el}}}{\lambda_{\text{irr}}^2}\right](\boldsymbol{F}\boldsymbol{M}\otimes\boldsymbol{F}\boldsymbol{M}) = J^{-1}\left[\frac{s_{\text{el}}}{\lambda_{\text{irr}}^2}\right](\boldsymbol{m}\otimes\boldsymbol{m}) \\
&= \left(J^{-1}\left[\frac{s_{\text{el}}}{\lambda_{\text{irr}}^2}\right]\lambda^2\right)(\hat{\boldsymbol{m}}\otimes\hat{\boldsymbol{m}}) \\
&= \sigma\,(\hat{\boldsymbol{m}}\otimes\hat{\boldsymbol{m}})\,,
\end{aligned}$$

with the scalar $\sigma = \left(J^{-1}\left[\frac{s_{\text{el}}}{\lambda_{\text{irr}}^2}\right]\lambda^2\right) = J^{-1}s_{\text{el}}\lambda_{\text{el}}^2$.

3. The scalar σ is a function of space and time, as well as the full time history of deformation. In this sense, the material is hyperelastic with memory.

4. The von Mises effective stress is $\sqrt{\frac{3}{2}\,\boldsymbol{s}(\boldsymbol{\sigma}):\boldsymbol{s}(\boldsymbol{\sigma})}$, where the stress deviator $\boldsymbol{s}(\boldsymbol{\sigma})$ is $\boldsymbol{\sigma} - \frac{1}{3}(\operatorname{tr}\boldsymbol{\sigma})\boldsymbol{I}$. If $\boldsymbol{\sigma}$ is a scalar a times $(\hat{\boldsymbol{m}}\otimes\hat{\boldsymbol{m}})$ for some unit vector $\hat{\boldsymbol{m}}$ (which is fortunately the case for us), then the von Mises effective stress is simply $|a|$, which is also $\hat{\boldsymbol{m}}\cdot\boldsymbol{\sigma}\hat{\boldsymbol{m}}$ for $a \geqslant 0$. In this case, the flow rule used in this work, $\langle\phi\rangle/\tau_{\text{relax}} = \langle\frac{a}{k} - 1\rangle/\tau_{\text{relax}}$, is the Perzyna model with rate sensitivity 1 and viscosity-related parameter τ_{relax} [de Souza Neto 2008, p. 448].

5. The timescale τ_{relax} determines the response rate of fibers in my simulated arteries. Its value affects the rate of enlargement of simulated aneurysms. I define it as an approximate timescale of fiber turnover, 70 days. Some researchers argue the turnover rate is accelerated in disease. I choose not to use a variable turnover rate, for lack of experimental data supporting material parameters of disease.

6. The bracket $\langle\cdot\rangle$ is the "positive part" of its argument:

$$\langle x\rangle \equiv \begin{cases} x & x > 0 \\ 0 & x \leqslant 0\,. \end{cases}$$

(For numerical stability, I round off the corner. See the footnote on page 67.)

7. The pseudoelastic stress limit $k = k(\boldsymbol{x}, t)$ is a function of space and time, and also of the current fiber stress σ, and the deformation history $\boldsymbol{\varphi}(\boldsymbol{X}, \cdot)$ of the point $\boldsymbol{X}$.

8. The pseudoelastic limit varies according to two terms, $\dot{k}_{\text{irr}}$ and $\dot{k}_{\text{les}}$. The first is a rate due to material hardening, and the second is a rate due to softening from lesion progression. That is, in this model, the pseudoelastic limit is initially high (as with healthy tissue) ($\sigma > k$), then decreases as the lesion grows (disease) ($\dot{k}_{\text{les}} < 0$). Eventually, the limit drops below healthy levels ($\sigma < k$) and irreversible strain begins. When irreversible strain begins, hardening occurs ($\dot{k}_{\text{irr}} > 0$), which may stabilize the artery (healing). The pseudoelastic limit then evolves according to the balance of these two terms.

9. Lesion onset is postulated as a reduction in the pseudoelastic limit term k_{les}^{∞}. The value of k_{les} follows the (time- and space-varying) postulated value k_{les}^{∞}. I could alter k_{les} or $\dot{k}_{\text{les}}$ (and thus k) directly; but for stability, k_{les}^{∞} alters k_{les} indirectly, through the control equation $\dot{k}_{\text{les}} = H_{\text{les}}(k_{\text{les}} - k_{\text{les}}^{\infty})$, whose steady-state solution is $k_{\text{les}} = k_{\text{les}}^{\infty}$.

10. I use two families of fibers, pointed perpendicular to each other, though this choice is not fundamental. Many setups with an overall isotropic response can be used, where the material can deform inelastically in the "tangent plane" perpendicular to the thickness direction. In fact, the theory presented here is can be thought of as

inelastic membrane strain, but I present it in terms of the "fiber family" formulation currently in vogue. (A true membrane model would have a strain energy due to shear.)

11. All fibers have the same material properties, except for the fiber direction, and are governed by the same constitutive equations.

12. I take fibers to be pointed at ±45 degrees from the axial direction. The axial direction—indeed the entire circumferential–thickness–axial coordinate frame—is defined by the push-forward of an ordinary thick cylinder onto the patient-specific geometry. See Figure 28 on page 102. Fibers are taken to have zero dispersion [Wicker 2008].

13. The elastic background material is used for the volumetric component of strain energy. The Lamé parameter is set at a very incompressible .4995.

3.8 Adaptive irreversible strain

Like every other model in the literature, the methodology above produces stable aneurysms that do not quite go saccular. In order to produce saccular aneurysms, I postulate that the pseudoelastic limit becomes dependent upon the current stress in the aneurysm. By creating a feedback loop, the theory produced saccular aneurysms. This is the first theory which has produced saccular aneurysm geometries from healthy artery geometries.

My constitutive model involves an adaptive pseudoelastic stress, which depends on the strain rate. Particularly, instead of specifying $\dot{k}_{\text{les}}$ (done via k^{∞}_{les}) and observing changes in $\dot{\lambda}_{\text{irr}}$, I specify changes in $\dot{\lambda}_{\text{irr}}$ and observe changes in $\dot{k}_{\text{les}}$.

$$
\begin{aligned}
\text{elastic strain:} \quad & \lambda_{\text{el}} = \frac{\lambda}{\lambda_{\text{irr}}}\,, \quad \lambda = \|\boldsymbol{m}\| \\
\text{collagen Cauchy stress tensor:} \quad & \boldsymbol{\sigma}_{\text{fib}} = \sigma\,(\hat{\boldsymbol{m}} \otimes \hat{\boldsymbol{m}}), \quad \hat{\boldsymbol{m}} = \boldsymbol{m}/\|\boldsymbol{m}\| \\
\text{collagen Cauchy stress scalar:} \quad & \sigma = \hat{\boldsymbol{m}} \cdot \boldsymbol{\sigma}_{\text{fib}} \hat{\boldsymbol{m}} \\
\textbf{postulated strain rate:} \quad & \dot{\lambda}_{\text{irr}} = \dot{\lambda}_{\text{irr}}(\boldsymbol{x}, t) \\
\text{flow rule:} \quad & \dot{\lambda}_{\text{irr}} = \frac{\langle \phi \rangle}{\tau_{\text{relax}}}\,, \quad \phi = \frac{\sigma}{k} - 1 \\
\text{pseudoelastic limit:} \quad & k = \sigma/(\dot{\lambda}_{\text{irr}} \tau_{\text{relax}} + 1) \\
\text{irreversible hardening:} \quad & \dot{k}_{\text{irr}} = \dot{\lambda}_{\text{irr}} H_{\text{irr}} \\
\text{lesion progression:} \quad & \dot{k}_{\text{les}} = \dot{k}_{\text{irr}} - \dot{k} \\
& \qquad = \dot{\lambda}_{\text{irr}} H_{\text{irr}} - \frac{d}{dt}\big[\, a/(\dot{\lambda}_{\text{irr}} \tau_{\text{relax}} + 1)\big] \\
& \qquad = \dot{k}_{\text{les}}(\sigma, \dot{\lambda}_{\text{irr}},\ \boldsymbol{x}, t)\ .
\end{aligned}
$$

This version of events is used when the irreversible strain rate is postulated to be positive, so that the flow rule is activated. In this case the aneurysm is actively enlarging. Lesion progression is determined by the postulated strain rate, instead of vice-versa (during passive enlargement). In fact, it would be better to say that lesion progression is defined by the postulated strain rate. During time intervals where I have somewhat arbitrary choices for settings of k_{les} or $\dot{\lambda}_{\text{irr}}$ (i.e., when $\sigma < k$), I choose so as to effect smooth functions of time. See figures below in Chapter 6 for explicit time histories of chosen parameters and resulting lesion progression.

3.9 Winkler foundation and vascular tone

Diseased artery tissue is made up of different material when compared to healthy tissue, and has a different biomechanical response. Both its structure and function are different.

For example, healthy tissue has elastin and a smooth muscle layer. Diseased tissue lacks these; it's predominantly collagen. In developed aneurysms, aneurysmal tissue is usually thinner—sometimes so thin as to be transparent, where a surgeon can see blood flowing through the artery wall.

Therefore I model healthy and diseased tissue differently. I argue that due to irreversible cellular changes within the artery wall, diseased tissue cannot return to its healthy state. This choice is different from the one in [Baek 2006] where turnover and evolving natural configurations model disease as a flawed return to homeostasis.

In diagnosed aneurysms, there is a complete or near complete loss of the muscular layer. Smooth muscle cells degenerate or modulate their phenotype in response to insult or injury. Their behavior plays a central role in initiation of aneurysms as well as their propensity for rupture [Starke 2014]. The degenerative process is not fully understood, but involves both apoptosis (programmed cell death) and a reduction in the proliferation of smooth muscle cells.

Once the contractile muscular layer is gone, aneurysms have a loss of basal vascular "tone"—the degree of constriction of a vessel from its maximally dilated state. All healthy vessels have tone. Tone is the active mechanism by which arteries maintain homeostasis.

As with every major process in the body, there are many competing influences on tone. Tone is determined by a number of neurohormonal factors extrinsic to the vessel, such as angiotensin II, atrial natriuretic peptide, and sympathetic nervous responses. It also has influences intrinsic to the vessel, such as contraction initiated by myocytes within the smooth muscle cells. If blood pressure increases, smooth muscle cells constrict to reduce flow; and if pressure lessens, vessels dilate to reduce vascular resistance and thus increase flow. Further, "smooth muscle tone can acutely modify residual strain, possibly through interconnections with matrix components" [Zeller 1998]; thus, *ex vivo* testing is an imperfect method for determining *in vivo* residual stress. These factors and more combine to effect the body's strict regulation of blood flow rate to the brain.

These systemic and autoregulation processes are not present in aneurysms; aneurysms always stay maximally dilated.

As a way of encapsulating these observations mathematically, I introduce a two-part lesion modulation. One part is a reduction in Young's modulus E inside the lesion. Important to us is that reducing Young's modulus lowers bending stiffness while still maintaining incompressibility. Another part is a so-called Winkler foundation term.[2] This term represents a macroscopic, combined model representing several biological effects: loss of the muscular layer and thus loss of basal tone, loss of perivas-

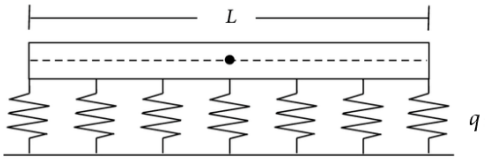

Figure 14: Winkler foundation. The material is modeled as if tiny springs are attached at each point, holding the material in its original position. The "spring constant" is q, measured per unit length (as depicted in this image) or volume (as used in this work).

[2] Emil Winkler originally proposed the term as an elastic model for soil foundations underneath railway beds, in [Winkler 1867].

cular tethering by the extracellular matrix within and surrounding the artery, and loss of support by adjacent tissues such as the brain and blood-brain barrier.

Aneurysmal tissue has no tone and no support, so its Winkler coefficient would be zero. Healthy tissue has a high tone, active mechanisms to maintain its healthy state, and so its Winkler coefficient would be high. This term is optional, and for thin structures I use a Winkler term of 0.

A Winkler foundation is a penalty on displacement, as seen in Figure 14 and equation (26). It is as if each point in the tissue has a small spring attached to it, holding it in its original position.

The Winkler term is often applied as a boundary term, acting on the surface of (in this case) the artery wall. In this work, the Winkler term is approximated as a body force, acting on the surface of the artery as well as in the interior. For thin structures this approximation is acceptable.

The residual $\boldsymbol{R}$ is

$$\boldsymbol{R} = \boldsymbol{F}^{\text{ext}} - (\boldsymbol{F}^{\text{int}} - q\boldsymbol{d}) = \boldsymbol{0}\,, \tag{26}$$

where $q = q(\boldsymbol{X}, t)$ is the volumetric Winkler stiffness coefficient. The $\boldsymbol{F}^{\text{ext}}$ represents external forces, $\boldsymbol{F}^{\text{int}}$ represents internal forces, $\boldsymbol{d}$ is displacement.

If I define the Winkler stiffness as a space-time function of, say, wall shear stress, I could gain the power to allow the evolving geometry to dictate formation of an aneurysm from a fluids calculation, and also better understand the aneurysm's stability. For now, the Winkler coefficient is arbitrarily chosen in advance.

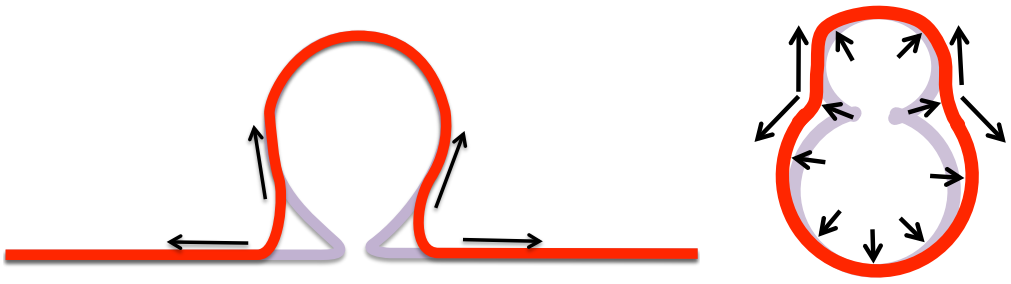

Figure 15: Stresses in an inflated aneurysm. Tension in artery walls from blood pressure or prestress act to enlarge the neck of a saccular aneurysm. This effect occurs in simulations of realistic 3D aneurysms. Bending stiffness also acts to enlarge sharp necks in aneurysms. The Winkler force opposes both of these.

3.10 Alternative growth theories

There have been several growth theories presented in the literature. I briefly present a few of them in order to make mathematical comparisons of them.

3.10.1 Fiber turnover and evolving natural configurations

In this theory, from [Baek 2006], fibers fade over time and are replaced by newer fibers. New fibers evolve their strain amounts and directions. Fix a material point $\boldsymbol{X}$, an arbitrary time $\tau \in [0, t]$ in the past, and take $\boldsymbol{x} = \boldsymbol{\varphi}_\tau(\boldsymbol{X})$. Suppose there is some natural configuration $\mathcal{B}^k$ of k-fibers at time τ. Suppose, within $\mathcal{B}^k$, that the direction $\boldsymbol{M}^k(\tau)$ represents the direction vector for a k-fiber created at time τ that is placed at $\boldsymbol{x}$.

Define a vector $\boldsymbol{M}^k(\tau)$ as the pull-back at time τ of $g_h \boldsymbol{m}^k(\tau, \tau)$ into a reference configuration:

$$\boldsymbol{M}^k(\tau) = \boldsymbol{F}^{-1}(\tau) g_h \boldsymbol{m}^k(\tau, \tau) \, .$$

Then the push-forward of $\boldsymbol{M}^k_{\text{ref}}(\tau)$ into the current (time t) configuration is

$$\boldsymbol{F}(t) \boldsymbol{F}^{-1}(\tau) g_h \boldsymbol{m}^k(\tau, \tau) \, .$$

Define $\boldsymbol{m}^k(\tau, t)$ as such:

$$g_h \boldsymbol{m}^k(\tau, t) = \boldsymbol{F}(t)\boldsymbol{F}^{-1}(\tau) g_h \boldsymbol{m}^k(\tau, \tau) \, .$$

Then $\boldsymbol{m}^k(\tau, t)$ points in the current direction of the k-fiber. Note that $\boldsymbol{m}^k(\tau, t)$ with $\tau = t$ is consistent with the notation $\boldsymbol{m}^k(\tau, \tau)$ previously defined. Also, $\boldsymbol{m}^k(\tau, t)$ is in general not a unit vector unless $\tau = t$, and the stretch in the fiber is

$$\lambda^k(\tau, t) := \left\| \boldsymbol{m}^k(\tau, t) \right\| \, .$$

Then $\lambda^k(\tau, t)$ is the stretch felt at the current time t by the k-fiber placed at $\boldsymbol{x} = \boldsymbol{\varphi}_\tau(\boldsymbol{X})$ at time τ.

To illustrate this result, put the above equations together to derive a formula for stretch separating the time variables t and τ:

$$\begin{aligned}
\lambda^k(\tau, t)^2 &= \left\| \boldsymbol{m}^k(\tau, t) \right\|^2 \\
&= \left\| \boldsymbol{F}(t)\boldsymbol{F}^{-1}(\tau) g_h \boldsymbol{m}^k(\tau, \tau) \right\|^2 \\
&= \left\| \boldsymbol{F}(t)\boldsymbol{M}^k(\tau) \right\|^2 \\
&= \left[\boldsymbol{F}(t)\boldsymbol{M}^k(\tau) \right]^{\mathsf{T}} \left[\boldsymbol{F}(t)\boldsymbol{M}^k(\tau) \right] \\
&= \left[\boldsymbol{M}^k(\tau) \right]^{\mathsf{T}} \boldsymbol{F}(t)^{\mathsf{T}} \boldsymbol{F}(t) \left[\boldsymbol{M}^k(\tau) \right] \\
&= \boldsymbol{M}^k(\tau)^{\mathsf{T}} \boldsymbol{C}(t) \boldsymbol{M}^k(\tau) \\
&= \boldsymbol{M}^k(\tau) \cdot \boldsymbol{C}(t) \boldsymbol{M}^k(\tau) \, .
\end{aligned}$$

The deformation tensor $\boldsymbol{C}(t) = \boldsymbol{F}(t)^{\mathsf{T}} \boldsymbol{F}(t)$ corresponds to $\boldsymbol{\varphi}_t$ of GNR.

The definition of fiber strain energy in [Baek 2006] is

$$W^k = W^k(\tau, t) = c_1 \Big(\exp \left[c_2 \left(g_h^2 \, \frac{\boldsymbol{M}^k(\tau) \cdot \boldsymbol{C}(t) \, \boldsymbol{M}^k(\tau)}{\boldsymbol{M}^k(\tau) \cdot \boldsymbol{C}(\tau) \, \boldsymbol{M}^k(\tau)} - 1 \right)^2 \right] - 1 \Big) \, .$$

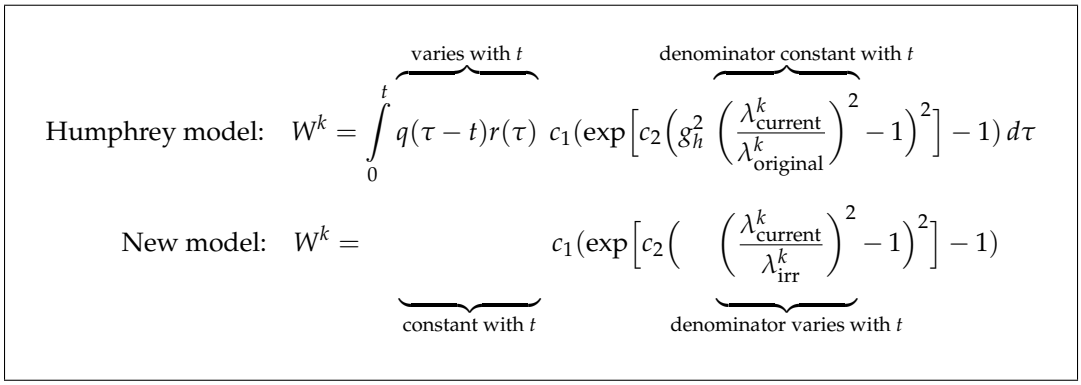

Figure 16: Comparison of the fiber turnover theory of [Baek 2006], commonly called the "Humphrey model," and the theory present here. In the new model, aneurysm enlargement proceeds at a pace determined by λ^k_{irr}. In the Humphrey model, aneurysm enlargement proceeds at a pace determined by the changing time integral of $q(\tau - t)r(\tau)$. Even though newer incarnations of this model use changing profiles for q that depend on strain rates and other factors, function profiles for q and r have not been found which create saccular aneurysms.

Now write

$$\lambda^k_{\text{current}} = \lambda^k(\tau, t) = \boldsymbol{M}^k(\tau) \cdot \boldsymbol{C}(t)\, \boldsymbol{M}^k(\tau)$$

$$\lambda^k_{\text{original}} = \lambda^k(\tau, \tau) = \boldsymbol{M}^k(\tau) \cdot \boldsymbol{C}(\tau)\, \boldsymbol{M}^k(\tau)\ ,$$

to compare this theory to the theory presented here.

The fiber turnover theory of [Baek 2006] uses a time integral for fibers:

$$\int_0^t q(\tau - t)r(\tau)W^k(\tau, t)\, d\tau\ .$$

When I compare them side-by-side, as in Figure 16, I can see the differences between the two theories.

3.10.2 Mass production

Mass production is a crucial aspect of [Baek 2006] model's behavior, and satisfactory expressions do not exist. For this section, I will describe the formulation of [Baek 2006]. Suppose there is a homeostatic stress σ_h, and homeostatic mass production value r_h^k.

$$\begin{aligned}
\boldsymbol{\sigma}_{\mathbf{cardiac}}(\tau) &= J(\tau)^{-1}\boldsymbol{F}(\tau)\boldsymbol{S}^k_{\text{cardiac}}(\tau)\boldsymbol{F}(\tau)^{\mathsf{T}}\,, \\
\sigma^k(\tau) &= \boldsymbol{m}^k(\tau,\tau)\cdot\boldsymbol{\sigma}_{\mathbf{cardiac}}(\tau)\boldsymbol{m}^k(\tau,\tau)\,, \text{ and finally} \\
r^k(\tau) &= r_h^k + r_h^k J(\tau)K_g\big(\sigma^k(\tau)-\sigma_h\big) \\
&= r_h^k\big(1+r^k_{K_g}(\tau)\big)\,.
\end{aligned} \tag{27}$$

The number K_g is a mass growth constant.

Notice that the formula for $\sigma^k(\tau)$ only calls for $\boldsymbol{m}^k(\tau,t)$ at time $t=\tau$.

The mass of the material is simply the sum of the contributions of its constituents plus the contribution of a non-growing elastin. The mass $R(t)$ at time t is a tradeoff between the decay and production of material:

$$R(t) = R^{\text{elastin}} + \sum_{k=1,2}\Big(R^kQ(t) + \int_0^t r^k(\tau)q(t-\tau)\,d\tau\Big) \tag{28}$$

where

$$q(\tau) = \exp(-K\tau)\chi_{\{\tau<\tau_{\max}\}}(\tau) \qquad \text{(exponential decay)} \tag{29}$$

$$\text{or}\quad q(\tau) = (\tau-\tau_{\max})^2(\tau+\tau_{\max}/2) \qquad \text{(cubic decay); and}$$

$$Q(t) = \frac{1}{\left|\int_0^{\tau_{\max}} q(\tau)\,d\tau\right|}\int_t^{\tau_{\max}} q(\tau)\,d\tau \tag{30}$$

are decay functions forced to zero by some time $\tau_{\max}$. The decay function q defines the reuptake of fibers and Q is for fibers existing at the start. Both fiber families start with equal mass: $R^k = \frac{1}{2}$.[3]

The homeostatic growth rate $r_h^k = R^k / \int q$ ensures healthy arteries are stable. Let us observe why this is so.

Temporarily, write $M^1(t)$ for the mass fraction $R^1 Q(t) + \int_0^t r^1(\tau) q(t-\tau)\, d\tau$ of 1-fibers. Then

$$M^1(0) = R^1 Q(0) + 0 = R^1 \,.$$

Assume $r^1(\tau) = r^1$ is constant for all time. For $T > \operatorname{supp}(q)$,

$$\begin{aligned} M^1(T) &= R^1 Q(T) + \int_0^T r^1 q(T-\tau)\, d\tau \\ &= 0 + r^1 \int_0^T q(T-\tau)\, d\tau \\ &= r^1 \int_0^T q(\tau)\, d\tau \,. \end{aligned}$$

If $M^1(t)$ is constant for all time, I must have $R^1 = r^1 \int_0^T q$. Then the value $r^1 = R^1 / \left(\int_0^T q\right)$ (which is a valid choice for r^1 if $\int q > 0$) is a time rate of mass production which achieves constant mass.

For simulation, q is assumed to be piecewise linear, following the time integration algorithm. This choice provides the pleasant property that the numeric time integration of q is exact, and mass fractions are numerically exact.

[3] Even with the elastin, fibers will be treated identically: $R^1 \equiv R^2$. But the R^k will be less than $\frac{1}{2}$ to take elastin into account: $R^1 + R^2 + R^{\text{elastin}} = 1$. The following values are reported in [Humphrey(2) 2002, p. 259] for canine carotid arteries: collagen dry weight = ~45%; elastin dry weight = ~20%; water wet weight = ~70%. Thus, $R^{\text{elastin}} = \frac{20}{45+20} = .30$, and $R^1 = R^2 = .35$. (The R^k do not take water into account.)

Proof: Suppose q is any decay function, and its values at equally-spaced times $t_n = n\,\Delta t$ are written as $q_n = q(t_n)$. For notational convenience, write

$$\sum_{m:n} q = \frac{1}{2}q_m + q_{m+1} + \cdots + q_{n-1} + \frac{1}{2}q_n \,,$$

and note

$$\sum_{m:n} q + \sum_{n:p} q = \sum_{m:p} q$$

for $m < n < p$.

Suppose that for arbitrary q, the sum $\sum_{m:n} q$ is an acceptable approximation to $\int_{[t_m,t_n]} q$. Suppose N is large enough that $t_N \geqslant \mathrm{supp}(q)$. Consider $r^{1h} := R^1 / \sum_{0:N} q$, a numerical approximation to the homeostatic value of r^1 calculated above. Use

$$Q^h(t_n) := \frac{1}{\sum_{0:N} q} \sum_{n:N} q \,.$$

Then for any time $t_n = n\,\Delta t$, with $n \in [0, \infty)$, approximating the value of $M^1(t_n)$ above leads to

$$\begin{aligned}
M^{1h}(t_n) &:= R^1 Q^h(t_n) + r^{1h} \sum_{0:n} q \\
&= R^1 \Big(\frac{1}{\sum_{0:N} q} \sum_{n:N} q \Big) + \Big(R^1 / \sum_{0:N} q \Big) \Big(\sum_{0:n} q \Big) \\
&= \Big(R^1 / \sum_{0:N} q \Big) \Big(\sum_{0:n} q + \sum_{n:N} q \Big) \\
&= \Big(R^1 / \sum_{0:N} q \Big) \Big(\sum_{0:N} q \Big) \\
&= R^1 \,.
\end{aligned}$$

Thus the claims hold.

Formulas for $r^k(\tau)$ is a subject of ongoing research. I can modify the growth rate $r^k(\tau)$ by adding some function of the wall shear stress. If $\mathrm{wss}^k(\tau)$ is the time-varying

wall shear stress for k-fibers at a point X, wss_h is a homeostatic value of wall shear stress, and K_{wss} is a sensitivity constant, then I can define a wall shear stress-induced growth component as

$$r^k_{\text{wss}}(\tau) = J(\tau)\big(K_{\text{wss}}\frac{\text{wss}^k(\tau) - \text{wss}_h}{\text{wss}_h}\big) \ .$$

(In practice, $\text{wss}^k(\tau)$ is only known for select times τ. For simplicity, I shall assume its value is piecewise constant in time.)

In this case, one might write

$$r^k(\tau) = r^k_h \left[1 + r^k_{K_g}(\tau) + r^k_{\text{wss}}(\tau)\right] \ .$$

It may be useful to include additional terms to model other growth signals.

The tensor $\boldsymbol{S}_{\text{cardiac}}$ is a time average of the Second P-K tensor $\boldsymbol{S}_{\text{FSI}}$ for the deformation computed for the cardiac cycle fluid-structure interaction simulation at the most recent time prior to time τ. The mass production term $r^k(\tau)$ is based on a scalar time-average $s^k(\tau)$ of the stresses due to a cardiac cycle.

3.10.3 Elastic-only Cauchy stress

When using a compressible material, a material model which achieves a Cauchy stress depending only on elastic energy is helpful. Particularly, when there is irreversible strain, but no change in elastic strain, the Cauchy stress should not change.

Use the subscript "fib" to denote quantities associated with the fiber hyperelastic strain energy function. A subscript "coll" will denote quantities associated with a new, Cauchy stress-oriented material model. Suppose the combined collagen strain energy response $\boldsymbol{S}_{\text{coll}}$ as a multiple of a single fiber's energy:

$$\boldsymbol{S}_{\text{coll}} = z\, \boldsymbol{S}_{\text{fib}} \ .$$

Pushing $\boldsymbol{S}_{\text{coll}}$ forward to $\boldsymbol{\sigma}_{\text{coll}}$ will reveal the mystery of z's composition. Note from above in equation (22) that $\boldsymbol{S}_{\text{fib}} = 2W'(\lambda_{\text{el}}^2)\,\frac{1}{\lambda_{\text{irr}}^2}(\boldsymbol{M}\otimes\boldsymbol{M}) = s_{\text{el}}/\lambda_{\text{irr}}^2(\boldsymbol{M}\otimes\boldsymbol{M})$. Also, decompose J into $J = \lambda_{\text{irr}}\lambda_{\text{el}}\lambda_{\text{A}}$, where $\lambda_{\text{A}} = J/\lambda = J/\|\boldsymbol{F}\boldsymbol{M}\|$ represents the change in area normal to $\boldsymbol{M}$ induced by $\boldsymbol{F}$.

$$
\begin{aligned}
\boldsymbol{\sigma}_{\text{coll}} &= J^{-1}\boldsymbol{F}\boldsymbol{S}_{\text{coll}}\boldsymbol{F}^{\mathsf{T}} \\
&= s_{\text{el}}\,\frac{z}{J\lambda_{\text{irr}}^2}\,\boldsymbol{F}(\boldsymbol{M}\otimes\boldsymbol{M})\boldsymbol{F}^{\mathsf{T}} \\
&= s_{\text{el}}\,\frac{z}{J\lambda_{\text{irr}}^2}\,(\boldsymbol{m}\otimes\boldsymbol{m}) \\
&= s_{\text{el}}\,\frac{z}{J\lambda_{\text{irr}}^2}\,\lambda^2\,(\hat{\boldsymbol{m}}\otimes\hat{\boldsymbol{m}}) \\
&= s_{\text{el}}\,\frac{z}{J\lambda_{\text{irr}}^2}\,\lambda_{\text{irr}}^2\lambda_{\text{el}}^2\,(\hat{\boldsymbol{m}}\otimes\hat{\boldsymbol{m}}) \\
&= s_{\text{el}}\,\frac{z}{J}\,\lambda_{\text{el}}^2\,(\hat{\boldsymbol{m}}\otimes\hat{\boldsymbol{m}}) \\
&= s_{\text{el}}\,\frac{z}{\lambda_{\text{irr}}\lambda_{\text{el}}\lambda_{\text{A}}}\,\lambda_{\text{el}}^2\,(\hat{\boldsymbol{m}}\otimes\hat{\boldsymbol{m}}) \\
&= s_{\text{el}}\left(\frac{z}{\lambda_{\text{irr}}\lambda_{\text{A}}}\right)\lambda_{\text{el}}\,(\hat{\boldsymbol{m}}\otimes\hat{\boldsymbol{m}})\,.
\end{aligned}
$$

If the scalar part of $\boldsymbol{\sigma}_{\text{coll}}$ is to depend only on elastic quantities, the term $z/(\lambda_{\text{irr}}\lambda_{\text{A}})$ should equal 1. Thus z can equal $\lambda_{\text{irr}}\lambda_{\text{A}}$, which in turn equals J/λ_{el}. I have achieved a possible formula for the material response of fibers.

$$
\begin{aligned}
\boldsymbol{S}_{\text{coll}} &= (J/\lambda_{\text{el}})\,\boldsymbol{S}_{\text{fib}} \\
\boldsymbol{\sigma}_{\text{coll}} &= (s_{\text{el}}\lambda_{\text{el}})(\hat{\boldsymbol{m}}\otimes\hat{\boldsymbol{m}})\,. \qquad (31)
\end{aligned}
$$

The elasticity tensors for this stress formula are

$$
\begin{aligned}
\mathbb{C}_{IJKL}^{\text{coll}} = 2\frac{\partial \boldsymbol{S}_{\text{coll}}}{\partial \boldsymbol{C}} &= 2\boldsymbol{S}_{\text{fib}}\frac{\partial(J/\lambda_{\text{el}})}{\partial \boldsymbol{C}} + \Big(\frac{J}{\lambda_{\text{el}}}\Big)\mathbb{C}_{IJKL}^{\text{fib}} \\
&\approx \Big(\frac{J}{\lambda_{\text{el}}}\Big)\boldsymbol{S}_{\text{fib}}\Big[\boldsymbol{C}^{-1} - \frac{1}{\lambda^2}(\boldsymbol{M}\otimes\boldsymbol{M})\Big] + \Big(\frac{J}{\lambda_{\text{el}}}\Big)\mathbb{C}_{IJKL}^{\text{fib}} \\
&= \boldsymbol{S}_{\text{coll}}\Big[\boldsymbol{C}^{-1} - \frac{1}{\lambda^2}(\boldsymbol{M}\otimes\boldsymbol{M})\Big] + \Big(\frac{J}{\lambda_{\text{el}}}\Big)\mathbb{C}_{IJKL}^{\text{fib}}\,.
\end{aligned}
$$

The push-forward of $\mathbb{C}^{\text{coll}}_{IJKL}$ is

$$\begin{aligned}\mathbb{c}^{\text{coll}}_{ijk\ell} &= \frac{1}{J}\boldsymbol{F}_{iI}\boldsymbol{F}_{jJ}\boldsymbol{F}_{kK}\boldsymbol{F}_{\ell L}\mathbb{C}^{\text{coll}}_{IJKL} \\ &\approx \boldsymbol{\sigma}_{\text{coll}}[\boldsymbol{I}-\hat{\boldsymbol{m}}\otimes\hat{\boldsymbol{m}}]+(J/\lambda_{\text{el}})\mathbb{c}^{\text{fib}}_{ijk\ell}\,.\end{aligned}$$

Particularly, note that $\mathbb{c}^{\text{coll}}_{ijk\ell}$ depends only on elastic quantities.

To derive $\mathbb{C}^{\text{coll}}_{IJKL}$, I made use of a helpful insight from equation (32). Most of the derivation is mundane, with some heavy grunt work conveniently provided by equation (50) below, $\partial J/\partial \boldsymbol{C} = (1/2)J\boldsymbol{C}^{-1}$. A few tricks are provided by $\lambda = \lambda_{\text{el}}\lambda_{\text{irr}}$, equation (34), and the assumption $\Delta t \ll \tau_{\text{relax}}$:

$$(2\lambda_{\text{el}})\frac{\partial\lambda_{\text{el}}}{\partial\boldsymbol{C}} = \frac{\partial\lambda^2_{\text{el}}}{\partial\boldsymbol{C}} = \frac{1}{\lambda^2_{\text{irr}}}\,\boldsymbol{M}\otimes\boldsymbol{M} + O\Big(\frac{\Delta t}{\tau_{\text{relax}}}\Big) \approx \frac{1}{\lambda^2_{\text{irr}}}\,\boldsymbol{M}\otimes\boldsymbol{M}\,.$$

$$\frac{\partial\lambda_{\text{el}}}{\partial\boldsymbol{C}} \approx \frac{1}{2\lambda_{\text{el}}}\frac{1}{\lambda^2_{\text{irr}}}\,\boldsymbol{M}\otimes\boldsymbol{M} = \frac{1}{2\lambda\,\lambda_{\text{irr}}}\,\boldsymbol{M}\otimes\boldsymbol{M}\,.$$

$$\frac{\partial(1/\lambda_{\text{el}})}{\partial\boldsymbol{C}} = -\frac{1}{\lambda^2_{\text{el}}}\frac{\partial\lambda_{\text{el}}}{\partial\boldsymbol{C}} \approx -\frac{1}{\lambda^2_{\text{el}}}\frac{1}{2\lambda\lambda_{\text{irr}}}\,\boldsymbol{M}\otimes\boldsymbol{M} = -\frac{1}{2\lambda^2\lambda_{\text{el}}}\,\boldsymbol{M}\otimes\boldsymbol{M}\,.$$

$$\begin{aligned}\frac{\partial(J/\lambda_{\text{el}})}{\partial\boldsymbol{C}} &\approx \frac{1}{2\lambda_{\text{el}}}J\boldsymbol{C}^{-1} - \frac{J}{2\lambda^2\lambda_{\text{el}}}\,\boldsymbol{M}\otimes\boldsymbol{M} \\ &= \frac{1}{2}\Big(\frac{J}{\lambda_{\text{el}}}\Big)\Big[\boldsymbol{C}^{-1} - \frac{1}{\lambda^2}\,(\boldsymbol{M}\otimes\boldsymbol{M})\Big]\,.\end{aligned} \tag{32}$$

3.10.4 Growth as elastic–plastic decomposition of deformation gradient

Consider an isotropic, homogeneous elastic material with no fibers. Assume that growth is considered as a multiplicative decomposition of the overall deformation gradient.

Call the initial configuration Ω_0, the final configuration Ω, and an intermediate configuration Ω_g. Write

$$\varphi : \Omega_0 \to \Omega_g$$

$$\varphi_e : \Omega_g \to \Omega \, .$$

The mapping $\varphi(\boldsymbol{X}) = \boldsymbol{X}_g$ is thought of as being a "pure" growth mapping, and $\varphi_e(\boldsymbol{X}_g) = \boldsymbol{x}$ is a purely elastic mapping. The deformation gradients

$$\boldsymbol{G} = \frac{\partial \boldsymbol{X}_g}{\partial \boldsymbol{X}}$$
$$\boldsymbol{F}_e = \frac{\partial \boldsymbol{x}}{\partial \boldsymbol{X}_g}$$

satisfy

$$\boldsymbol{F} = \boldsymbol{F}_e \boldsymbol{G} = \frac{\partial \boldsymbol{x}}{\partial \boldsymbol{X}} \, .$$

As a modeling assumption, define the total energy of the system as the elastic energy:

$$\Psi = \int_{\Omega_g} \psi_e(\boldsymbol{X}_g) \, dV_g$$

where $\psi_e : \Omega_g \to \mathbb{R}$ is the elastic strain energy density in the grown configuration. Growth is not considered as adding energy: Ω_g is considered a (potentially nonphysical) stress-free configuration for the final body.

Note that the volume elements dV_0, dV_g, and dv are comfortably related by

$$dV_g = \qquad\qquad (\det \boldsymbol{G}) dV_0 \, ,$$

$$dv = (\det \boldsymbol{F}_e) dV_g = (\det \boldsymbol{F}_e)(\det \boldsymbol{G}) dV_0 = (\det \boldsymbol{F}) dV_0 \, .$$

A pull-back of Ψ to Ω_0 yields

$$\begin{aligned}\Psi &= \int_{\Omega_0} (\det \boldsymbol{G})\ \psi_e(\varphi(\boldsymbol{X}))\ dV_0 \\ &= \int_{\Omega_0} \psi(\boldsymbol{X})\ dV_0\ ,\end{aligned}$$

where I have defined $\psi(\boldsymbol{X})$ to be the strain energy density associated with the deformation $\boldsymbol{F}$:

$$\psi(\boldsymbol{X}) = (\det \boldsymbol{G})\ \psi_e(\varphi(\boldsymbol{X}))\ .$$

This gives

$$\boldsymbol{P} = \frac{\partial \psi}{\partial \boldsymbol{F}} = (\det \boldsymbol{G})\ \boldsymbol{P}_e \boldsymbol{G}^{-\mathsf{T}}\ .$$

(In obtaining this result, I made the eminently reasonable assumption that $\boldsymbol{G}$ is independent of $\boldsymbol{F}$—indeed, after time discretization and simplifying numerical assumptions are made, $\boldsymbol{G}$ is constant.)

A few more observations: $\boldsymbol{S}$ and $\mathbb{C}$ take similar forms in terms of their growth and elastic components:

$$\begin{aligned}\boldsymbol{S}_{IJ} &= (\det \boldsymbol{G})\ \boldsymbol{G}^{-1}_{IK}\ \boldsymbol{S}_{e\,KL}\ \boldsymbol{G}^{-\mathsf{T}}_{LJ}\ , \\ \mathbb{C}_{IJKL} &= (\det \boldsymbol{G})\ \boldsymbol{G}^{-1}_{IM}\boldsymbol{G}^{-1}_{JN}\boldsymbol{G}^{-1}_{KP}\boldsymbol{G}^{-1}_{LQ}\ \mathbb{C}_{e\,MNPQ}\ .\end{aligned}$$

Utilizing these formulae in the IBVP allows independent growth and elastic deformations to take place.

Let us consider two families of fibers which shall be represented by the distinct directions $\boldsymbol{a}$ and $\boldsymbol{b}$ in which they point. For simplicity, let us assume $\forall \boldsymbol{X},\ \boldsymbol{a} \neq \boldsymbol{b}$ so that $\{\boldsymbol{a}, \boldsymbol{b}, \boldsymbol{a} \times \boldsymbol{b}\}$ spans $\mathbb{R}^3$.

For scalars g_1, g_2, and g_3, define the growth tensor as diagonal in this coordinate system.

$$\begin{aligned}\boldsymbol{G} &= g_1(\boldsymbol{a}\otimes\boldsymbol{a}) + g_2(\boldsymbol{b}\otimes\boldsymbol{b}) + g_3(\boldsymbol{a}\times\boldsymbol{b})\otimes(\boldsymbol{a}\times\boldsymbol{b}) \\ &= \begin{bmatrix} g_1 & & \\ & g_2 & \\ & & g_3 \end{bmatrix}_{\{\boldsymbol{a},\boldsymbol{b},\boldsymbol{a}\times\boldsymbol{b}\}} .\end{aligned}$$

This $\boldsymbol{G}$ should be thought of as acting in the fiber directions, with a third action, g_3, controlling volume changes given g_1 and g_2. The scalars g_1 and g_2 represent the amounts of extension (or shortening) in the two fiber directions. The third parameter, g_3, is determined by the increase or decrease of mass of the fibers which is not accounted for in the extension or shortening. (In general, mass increase is independent of fiber lengthening [Humphrey(2) 2002].) Growth may vary with time and space, but must be physical:

$$\boldsymbol{a} = \boldsymbol{a}(\boldsymbol{X},t) \neq \boldsymbol{0}$$

$$\boldsymbol{b} = \boldsymbol{b}(\boldsymbol{X},t) \neq \boldsymbol{0}$$

$$\boldsymbol{a}\times\boldsymbol{b} \neq \boldsymbol{0}$$

$$g_1 = g_1(\boldsymbol{X},t) > 0$$

$$g_2 = g_2(\boldsymbol{X},t) > 0$$

$$g_3 = g_3(\boldsymbol{X},t) > 0$$

$$\det \boldsymbol{G}(\boldsymbol{X},t) > 0\,.$$

The strain energy function of fibers acts only in the fiber direction. (This is a modeling assumption.) Consider, for a moment, the strain energy $\psi^{\boldsymbol{a}}$ of fibers in direction $\boldsymbol{a}$:

$$\begin{aligned}
\psi^{\boldsymbol{a}} &= (\det \boldsymbol{G})\, \psi_e^{\boldsymbol{a}}(\boldsymbol{a} \cdot \boldsymbol{C}_e \boldsymbol{a}) \\
&= (\det \boldsymbol{G})\, \psi_e^{\boldsymbol{a}}(\boldsymbol{a} \cdot \boldsymbol{G}^{-\mathsf{T}} \boldsymbol{C} \boldsymbol{G}^{-1} \boldsymbol{a}) \\
&= (\det \boldsymbol{G})\, \psi_e^{\boldsymbol{a}} \left(\begin{bmatrix} 1 \\ 0 \\ 0 \end{bmatrix} \cdot \begin{bmatrix} 1/g_1 & & \\ & 1/g_2 & \\ & & 1/g_3 \end{bmatrix} \boldsymbol{C} \begin{bmatrix} 1/g_1 & & \\ & 1/g_2 & \\ & & 1/g_3 \end{bmatrix} \begin{bmatrix} 1 \\ 0 \\ 0 \end{bmatrix} \right) \\
&= (\det \boldsymbol{G})\, \psi_e^{\boldsymbol{a}} \left(\begin{bmatrix} 1/g_1 \\ 0 \\ 0 \end{bmatrix} \cdot \boldsymbol{C} \begin{bmatrix} 1/g_1 \\ 0 \\ 0 \end{bmatrix} \right) \\
&= (\det \boldsymbol{G})\, \psi_e^{\boldsymbol{a}} \left(\begin{bmatrix} 1/g_1 \\ 0 \\ 0 \end{bmatrix} \cdot \boldsymbol{F}^{\mathsf{T}} \boldsymbol{F} \begin{bmatrix} 1/g_1 \\ 0 \\ 0 \end{bmatrix} \right) .
\end{aligned}$$

Now suppose that $\boldsymbol{F}$ takes on the special form

$$\boldsymbol{F} = \begin{bmatrix} f & & \\ & 1 & \\ & & 1 \end{bmatrix}_{\{\boldsymbol{a},\boldsymbol{b},\boldsymbol{a}\times\boldsymbol{b}\}} ,$$

meaning that the deformation is one-dimensional and allowed only in the fiber direction $\boldsymbol{a} = [1,0,0]^{\mathsf{T}}_{\{\boldsymbol{a},\boldsymbol{b},\boldsymbol{a}\times\boldsymbol{b}\}}$.

$$\begin{aligned}
\psi^{\boldsymbol{a}} &= (\det \boldsymbol{G})\, \psi_e^{\boldsymbol{a}} \left(\begin{bmatrix} 1/g_1 \\ 0 \\ 0 \end{bmatrix} \cdot \boldsymbol{F}^{\mathsf{T}} \boldsymbol{F} \begin{bmatrix} 1/g_1 \\ 0 \\ 0 \end{bmatrix} \right) \\
&= (\det \boldsymbol{G})\, \psi_e^{\boldsymbol{a}} \left(\begin{bmatrix} 1/g_1 \\ 0 \\ 0 \end{bmatrix} \cdot \begin{bmatrix} f & & \\ & 1 & \\ & & 1 \end{bmatrix} \begin{bmatrix} f & & \\ & 1 & \\ & & 1 \end{bmatrix} \begin{bmatrix} 1/g_1 \\ 0 \\ 0 \end{bmatrix} \right) \\
&= (\det \boldsymbol{G})\, \psi_e^{\boldsymbol{a}} \left(\begin{bmatrix} f/g_1 \\ 0 \\ 0 \end{bmatrix} \cdot \begin{bmatrix} f/g_1 \\ 0 \\ 0 \end{bmatrix} \right) .
\end{aligned}$$

Thus, if f is initially 1 and g_1 becomes different from 1, then maintaining equilibrium requires the overall $\boldsymbol{F}$ to scale the material by a factor of g_1 in the direction of $\boldsymbol{a}$ so as to balance the $1/g_1$ terms. (The determinant of $\boldsymbol{G}$ can be assumed to have remained at 1 throughout.) In fact, this is exactly the same behavior as if the fibers were to lengthen by

a factor of g_1; said another way, the new notion of growth mimics the behavior of changing the *irreversible strain* of fibers. So growth here is equivalent to growth via turnover discussed above, at least in certain situations.

3.10.5 Membrane formulation

A two-dimensional membrane formulation of the theory presented here would appear as follows:

$$\boldsymbol{F}_{\text{irr}} = \begin{bmatrix} \lambda_{11} & \lambda_{12} & \\ \lambda_{21} & \lambda_{22} & \\ & & 1 \end{bmatrix}_{\{\hat{\boldsymbol{m}}^1,\, \hat{\boldsymbol{m}}^2,\, \hat{\boldsymbol{m}}^1 \times \hat{\boldsymbol{m}}^2\}} .$$

The $\hat{\boldsymbol{m}} = \hat{\boldsymbol{m}}(\boldsymbol{x}, t)$ directions may not necessarily be fiber directions, but could be unit vectors in some frame $\{\hat{\boldsymbol{m}}^1, \hat{\boldsymbol{m}}^2, \hat{\boldsymbol{m}}^1 \times \hat{\boldsymbol{m}}^2\}$ defined on the membrane. A membrane model would have an effect due to shear, which is not present in my fiber model. My formulation takes the following form, which does not have shear terms λ_{12} or λ_{21}:

$$\boldsymbol{F}_{\text{irr}} = \begin{bmatrix} \lambda_{\text{irr}}^{k=1} & & \\ & \lambda_{\text{irr}}^{k=2} & \\ & & 1 \end{bmatrix}_{\{\hat{\boldsymbol{m}}^1,\, \hat{\boldsymbol{m}}^2,\, \hat{\boldsymbol{m}}^1 \times \hat{\boldsymbol{m}}^2\}} .$$

Chapter 4

Discretization

Having defined my theory, I can proceed to the numerics. I use isogeometric analysis with hierarchical B-Spline basis functions. A discussion of hierarchical splines can be found in [Evans 2015]. I use hierarchical B-Splines for their ability to describe organic geometries well, and for local refinement. I do local refinement in the lesion region. In my simulations I will use larger, high degree basis functions. This helps avoid some issues with incompressiblility causing bending stiffness.

Time discretization uses Backward Euler, a stable method. I assume the material is quasi-static because growth happens over a long timescale (weeks to years). Time dependence comes from time-dependent material properties (regional decay of the artery wall). I use Newton–Raphson convergence. The simulation is dynamic, for better convergence rates.

The timescale of the problem comes from the rate of change of data, partly defined by τ_{relax}, the timescale of turnover of collagen fibers. $\tau_{\text{relax}} = 70$ days. My timestep is $\Delta t_n \leqslant 1$ day, so $0 < \Delta t_n \ll \tau_{\text{relax}}$. For Newton convergence, I use a slightly inconsistent tangent where I ignore any term containing the factor $\Delta t_n / \tau_{\text{relax}}$.

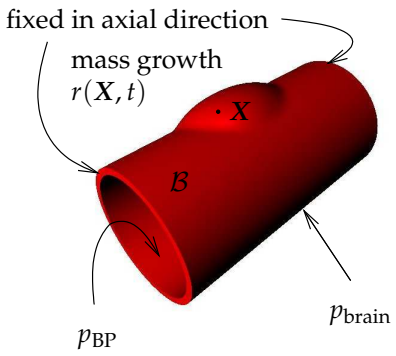

Figure 17: The body $\mathcal{B}$ in the growth and remodeling problem. Boundary conditions are shown. The material is a neo-Hookean hyperelastic solid supported by fibers. The simulation is quasi-static, being on a timescale of weeks to decades.

4.1 Spatial discretization

Discretize the space Ω_0 and Γ_h into Ω_0^s and Γ_{h0}^s, and denote nodes in the discretized spaces by A or B. In a slight abuse of notation,[1] write $\boldsymbol{N}^A$ to represent basis functions.[2]

Now define

$$\mathcal{V}^h = \text{span}\{\boldsymbol{N}^A : A \text{ is an interior node}\}$$

$$\mathcal{S}^h = \mathcal{V}^h \oplus (\text{boundary conditions})$$

as finite-dimensional approximations to $\mathcal{V}$ and $\mathcal{S}$. Write

$$\boldsymbol{\psi}^h = \boldsymbol{\psi}_i^h \boldsymbol{e}_i \quad \text{and} \quad \boldsymbol{\psi}_i^h = \boldsymbol{N}^A c_i^A \in \mathcal{V}^h \,,$$

$$\boldsymbol{\varphi}^h = \boldsymbol{\varphi}_i^h \boldsymbol{e}_i \quad \text{and} \quad \boldsymbol{\varphi}_i^h = \boldsymbol{N}^B d_i^B \in \mathcal{S}^h$$

in terms of some basis $\boldsymbol{e}_i$ as linear combinations of basis functions $\boldsymbol{N}^A$ defined at each node.

[1] For higher-order approximations, there are multiple basis functions for each node. Therefore, A in "$\boldsymbol{N}^A$" ranges over a different (larger) set than A in "node A." There is a natural correspondence from one to the other, so confusion should not arise.

[2] Note that $\boldsymbol{N}^A \neq \boldsymbol{N} \neq \boldsymbol{N}_I$. The first is a basis function at node A, the second is the unit normal in the material description, and the third is the I-th component of the second.

With this notation the Galerkin formulation of (GNR, W) is

$$\text{(GNR, G)} \left\{ \begin{array}{c} \text{Given } g,\ h,\ \text{find } \boldsymbol{\varphi}^h \in \mathcal{S}^h \text{ such that for all } \boldsymbol{\psi}^h \in \mathcal{V}^h\ , \\ \left(\boldsymbol{\psi}^h_{i,J},\ \boldsymbol{F}_{iI}\boldsymbol{S}_{IJ}\right)_{\Omega_0} = \left(\boldsymbol{\psi}^h_i,\ Jh\boldsymbol{F}_{iI}^{-\mathsf{T}}\boldsymbol{N}_I\right)_{\Gamma_{h0}}\ , \end{array} \right.$$

After factoring c_i^A, the constitutive law of (GNR, G) becomes, for each $i = 1, 2, 3$,

$$\left(\frac{\partial \boldsymbol{N}^A}{\partial \boldsymbol{X}_J},\ \boldsymbol{F}_{iI}\boldsymbol{S}_{IJ}\right)_{\Omega_0} - \left(\boldsymbol{N}^A,\ Jh\boldsymbol{F}_{iI}^{-\mathsf{T}}\boldsymbol{N}_I\right)_{\Gamma_{h0}} = 0\ , \tag{33}$$

where $\boldsymbol{X}_J$ is the J-th coordinate of $\boldsymbol{X}$ and the residual $\boldsymbol{R}_i^A$ is the residual in the i-th direction at node A. The space Ω_0 refers to the reference configuration; Γ_{h0} is the Neumann boundary of the artery in the reference configuration. The displacement $\boldsymbol{U}_j^B$ is the displacement in the direction j at node B.

Mapping the integrals into Gauss space, where integration is performed, provides the following. The volumetric term of the residual is

$$\begin{aligned}
\left(\frac{\partial \boldsymbol{N}^A}{\partial \boldsymbol{X}_J},\ \boldsymbol{F}_{iI}\boldsymbol{S}_{IJ}\right)_{\Omega_0} &= \int_{\Omega_0} \left(\frac{\partial \boldsymbol{N}^A}{\partial \boldsymbol{X}_J}\boldsymbol{F}_{iI}\boldsymbol{S}_{IJ}\right) dV_{\boldsymbol{X}} \\
&= \sum_e \int_{\square^e} \left(\frac{\partial \boldsymbol{N}^A}{\partial \boldsymbol{X}_J}\boldsymbol{F}_{iI}\boldsymbol{S}_{IJ}\right)\Big|_{\boldsymbol{X}=\boldsymbol{X}(\boldsymbol{\xi})} \left|\frac{d\boldsymbol{X}}{d\boldsymbol{\xi}}\right| dV_{\boldsymbol{\xi}} \\
&= \sum_e \int_{G^3} \left(\frac{\partial \boldsymbol{N}^A}{\partial \boldsymbol{X}_J}\boldsymbol{F}_{iI}\boldsymbol{S}_{IJ}\right)\Big|_{\boldsymbol{X}(\boldsymbol{\xi}(\boldsymbol{g}))} \left|\frac{d\boldsymbol{X}}{d\boldsymbol{\xi}}(\boldsymbol{\xi}(\boldsymbol{g}))\right| \left|\frac{d\boldsymbol{\xi}}{d\boldsymbol{g}}\right| dV_{\boldsymbol{g}} \\
&= \sum_e \sum_{\mathbf{gp}\in G^3} \left(\frac{\partial \boldsymbol{N}^A}{\partial \boldsymbol{X}_J}\boldsymbol{F}_{iI}\boldsymbol{S}_{IJ}\right)\Big|_{\boldsymbol{X}(\boldsymbol{\xi}(\mathbf{gp}))} \left|\frac{d\boldsymbol{X}}{d\boldsymbol{\xi}}(\boldsymbol{\xi}(\mathbf{gp}))\right| \left|\frac{d\boldsymbol{\xi}}{d\boldsymbol{g}}(\mathbf{gp})\right| \mathrm{gwt}(\mathbf{gp})\ ,
\end{aligned}$$

where the functions $\left|\frac{dX}{d\xi}\right|$ and $\left|\frac{d\xi}{dg}\right|$ are volumetric Jacobians. Marked with the variable names from the code, this term is

$$\underbrace{\left(\frac{\partial N^A}{\partial X_J},\, F_{iI}S_{IJ}\right)_{\Omega_0}}_{\texttt{RHSGu}} = \underbrace{\sum_{\substack{e\\ \uparrow\\ \texttt{iel}}} \sum_{\mathbf{gp}\in G^3}}_{\substack{\texttt{Localto}-\\ \texttt{Global\_3D\_u}}} \underbrace{\left(\frac{\partial N^A}{\partial X_J}F_{iI}S_{IJ}\right)\Big|_{X(\xi(\mathbf{gp}))}}_{\substack{\text{(body forces: } \texttt{shgu}\times\texttt{fi})\\ +\ \texttt{shgradgu}\times\texttt{Ftens}\times\texttt{Stens}}} \underbrace{\left|\frac{dX}{d\xi}(\xi(\mathbf{gp}))\right|}_{\texttt{DetJ}} \underbrace{\left|\frac{d\xi}{dg}(\mathbf{gp})\right|}_{\texttt{da}} \underbrace{\underbrace{\mathrm{gwt}(\mathbf{gp})}_{\substack{\texttt{gwu(igauss)}\\ \times\texttt{gwv(jgauss)}\\ \times\texttt{gww(kgauss)}}}}_{\texttt{gwt}} .$$

Similarly, the boundary term of the residual is

$$\begin{aligned}
&\left(N^A,\, JhF^{-\mathsf{T}}_{iI}N_I\right)_{\Gamma_{h0}}\\
&= \int_{\Gamma_{h0}} N^A JhF^{-\mathsf{T}}_{iI}N_I\, dA_X\\
&= \sum_f \int_{\square^f_h} \left(N^A JhF^{-\mathsf{T}}_{iI}N_I\right)\Big|_{X=X(\xi)} \left|\frac{d\phi^f}{d\xi}\right| dA_\xi\\
&= \sum_f \int_{G^2_h} \left(N^A JhF^{-\mathsf{T}}_{iI}N_I\right)\Big|_{X(\xi(g))} \left|\frac{d\phi^f}{d\xi}(\xi(g))\right| \left|\frac{d\gamma^f}{dg}\right| dA_g\\
&= \sum_f \sum_{\mathbf{gp}\in G^2_h} \left(N^A JhF^{-\mathsf{T}}_{iI}N_I\right)\Big|_{X(\xi(\mathbf{gp}))} \left|\frac{d\phi^f}{d\xi}(\xi(\mathbf{gp}))\right| \left|\frac{d\gamma^f}{dg}(\mathbf{gp})\right| \mathrm{gwt}\,,\\
&= \sum_{\substack{f\\ \uparrow\\ \texttt{ifac}}} \underbrace{\sum_{\mathbf{gp}\in G^2_h}}_{\substack{\texttt{Localto}-\\ \texttt{GlobalB_3D_u}}} \underbrace{\left(N^A JhF^{-\mathsf{T}}_{iI}N_I\right)\Big|_{X(\xi(\mathbf{gp}))}}_{\texttt{shbu}\times\texttt{traction}} \underbrace{\left|\frac{d\phi^f}{d\xi}(\xi(\mathbf{gp}))\right|}_{\texttt{Jb_em}} \underbrace{\underbrace{\left|\frac{d\gamma^f}{dg}(\mathbf{gp})\right|}_{\texttt{da}} \underbrace{\mathrm{gwt}}_{\substack{\texttt{gw(igaussb)}\\ \times\texttt{gw(jgaussb)}}}}_{\texttt{gwt}} ,
\end{aligned}$$

where the functions $\left|\frac{d\phi^f}{d\xi}(\xi)\right|$ and $\left|\frac{d\gamma^f}{dg}(g)\right|$ are the Jacobians of the *surface mappings*

$$G^2 \to \square^f \to \Gamma_0$$

$$G^2_h \to \square^f_h \to \Gamma_{h0}$$

induced by ϕ^e and γ^e, and where the corresponding "Neumann" surfaces for the element and Gaussian spaces are $\square^f_h = (\phi^f)^{-1}(\Gamma_{h0})$ and $G^2_h = (\gamma^f)^{-1}(\square^f_h)$.

4.2 Time discretization of adaptive irreversible strain

I use a simple scheme for time discretization. For the below, n refers to a value at the previously-computed timestep, and $n+1$ indicates a value at the new timestep. Here is the order of the calculations:

$$
\begin{aligned}
\text{postulated strain rate:} \quad & \dot{\lambda}^{\text{irr}}_{n+1} = \dot{\lambda}^{\text{irr}}(\boldsymbol{x}_{n+1}, t_{n+1}) \\
\text{time integration:} \quad & \lambda^{\text{irr}}_{n+1} = \lambda^{\text{irr}}_{n} + \dot{\lambda}^{\text{irr}}_{n+1} \Delta t_{n+1} \\
\text{fiber direction:} \quad & \boldsymbol{m}_{n+1} = \boldsymbol{F}_{n+1}\, \boldsymbol{M} \\
\text{elastic strain:} \quad & \lambda^{\text{el}}_{n+1} = \frac{\lambda_{n+1}}{\lambda^{\text{irr}}_{n+1}}\,, \quad \lambda_{n+1} = \|\boldsymbol{m}_{n+1}\| \\
& s^{\text{el}}_{n+1} = 2\, W'_{\text{fib}}\big((\lambda^{\text{el}}_{n+1})^2\big) \\
\text{collagen Cauchy stress scalar:} \quad & a_{n+1} = s^{\text{el}}_{n+1} (\lambda^{\text{el}}_{n+1})^2 / J_{n+1}\,, \quad J_{n+1} = \det \boldsymbol{F}_{n+1} \\
\text{collagen Cauchy stress tensor:} \quad & \boldsymbol{\sigma}^{\text{fib}}_{n+1} = (a_{n+1})(\hat{\boldsymbol{m}}_{n+1} \otimes \hat{\boldsymbol{m}}_{n+1}), \quad \hat{\boldsymbol{m}}_{n+1} = \boldsymbol{m}_{n+1} / \|\boldsymbol{m}_{n+1}\|
\end{aligned}
$$

The update for the pseudoelastic limit comes from the postulated formula for the flow rule $\dot{\lambda}^{\text{irr}}_{n+1} = \langle \phi_{n+1} \rangle / \tau_{\text{relax}}$ where $\phi_{n+1} = \sigma_{n+1}/k_{n+1} - 1$. Solving for k_{n+1} gives

$$
\begin{aligned}
\text{pseudoelastic limit:} \quad k_{n+1} &= \begin{cases} \sigma_{n+1}/(\dot{\lambda}^{\text{irr}}_{n+1}\tau_{\text{relax}} + 1) & \text{if } \dot{\lambda}^{\text{irr}}_{n+1} > 0\,, \\ k_n & \text{otherwise.} \end{cases} \\
\dot{k}_{n+1} &= (k_{n+1} - k_n)/\Delta t^{n+1} \\
\text{irreversible hardening:} \quad \dot{k}^{\text{irr}}_{n+1} &= \dot{\lambda}^{\text{irr}}_{n+1} H^{\text{irr}} \\
\text{lesion progression:} \quad \dot{k}^{\text{les}}_{n+1} &= \dot{k}^{\text{irr}}_{n+1} - \dot{k}_{n+1} \\
&= \dot{k}^{\text{irr}}_{n+1} - \sigma_{n+1}/(\dot{\lambda}^{\text{irr}}_{n+1}\tau_{\text{relax}} + 1) \\
&= \dot{k}_{\text{les}}(\sigma_{n+1}, \dot{\lambda}^{\text{irr}}_{n+1},\ \boldsymbol{x}_{n+1}, t_{n+1}) \\
\text{time integration:} \quad k^{\text{el}}_{n+1} &= k^{\text{el}}_n + \dot{k}^{\text{el}}_{n+1}\Delta t_{n+1} \\
k^{\text{irr}}_{n+1} &= k^{\text{irr}}_n + \dot{k}^{\text{irr}}_{n+1}\Delta t_{n+1}\,.
\end{aligned}
$$

4.2.1 Consistent tangent for time-discretized problem

Computing a consistent tangent is complicated, but useful for Newton–Raphson convergence. Briefly, consider the 2nd Piola–Kirchhoff stress as a function of the square of the elastic part of the strain: $\boldsymbol{S} = \boldsymbol{S}(\lambda^2_{\text{el}}) = \boldsymbol{S}(\lambda^2/\lambda^2_{\text{irr}})$. This makes usage of the chain rule easier. (The notation here for squares of strains is crude but effective: $\lambda^{\text{el}\,2}_{n+1} = \lambda^{\text{el}}_{n+1}\lambda^{\text{el}}_{n+1}$ and $\lambda^{\text{irr}\,2}_{n+1} = \lambda^{\text{irr}}_{n+1}\lambda^{\text{irr}}_{n+1}$.)

Suppose I am at timestep t_{n+1}. Suppose the amount of irreversible strain at the previous timestep was λ^{irr}_n, and that I am in the case where there is no additional irreversible strain this timestep. That is to say, $\lambda^{\text{irr}}_{n+1} = \lambda^{\text{irr}}_n$, and

$$
\lambda^{\text{el}}_{n+1} = \lambda_{n+1}/\lambda^{\text{irr}}_{n+1} = \lambda_{n+1}/\lambda^{\text{irr}}_n\,.
$$

Conveniently, λ_n^{irr} is a constant at time t_{n+1}. Then the algorithm calls for a 2nd Piola–Kirchhoff stress of

$$\boldsymbol{S}_{n+1}^{\text{algo}} = \boldsymbol{S}(\lambda_{n+1}^{\text{el}\,2}) = \boldsymbol{S}(\lambda_{n+1}^2/\lambda_n^{\text{irr}\,2})\,.$$

Then its derivative with respect to $\boldsymbol{C}_{n+1}$ becomes

$$\begin{aligned}
2\frac{\partial \boldsymbol{S}_{n+1}^{\text{algo}}}{\partial \boldsymbol{C}} &= 2\frac{d\boldsymbol{S}(\lambda_{n+1}^{\text{el}\,2})}{d(\lambda_{n+1}^{\text{el2}})}\,\frac{\partial(\lambda_{n+1}^{\text{el}\,2})}{\partial \boldsymbol{C}} \\
&= 2\boldsymbol{S}'(\lambda_{n+1}^{\text{el}\,2})\,\frac{\partial}{\partial \boldsymbol{C}}(\lambda_{n+1}^2/\lambda_n^{\text{irr}\,2}) \\
&= 2\boldsymbol{S}'(\lambda_{n+1}^{\text{el}\,2})\,\frac{1}{\lambda_n^{\text{irr}\,2}}(\boldsymbol{M}_n \otimes \boldsymbol{M}_n) \\
&= 2\boldsymbol{S}'(\lambda_{n+1}^{\text{el}\,2})\,\frac{1}{\lambda_n^{\text{irr}\,2}}(\boldsymbol{M}_n \otimes \boldsymbol{M}_n) \\
&= 2\boldsymbol{S}'(\lambda_{n+1}^{\text{el}\,2})\,\frac{1}{\lambda_{n+1}^{\text{irr}\,2}}(\boldsymbol{M}_n \otimes \boldsymbol{M}_n)\,.
\end{aligned}$$

In the case of adaptive irreversible strain, the new irreversible strain amount is prescribed. In the case of non-adaptive irreversible strain, compute "trial" stress using the amount of irreversible strain from the last timestep:

$$\begin{aligned}
\boldsymbol{S}_{n+1}^{\text{tr}} &= \boldsymbol{S}(\lambda_{n+1}^2/\lambda_n^{\text{irr}\,2}) \\
\sigma_{n+1}^{\text{tr}} &= \boldsymbol{m}_{n+1}\cdot\left(\boldsymbol{F}_{n+1}\boldsymbol{S}_{n+1}^{\text{tr}}\boldsymbol{F}_{n+1}^{\mathsf{T}}\right)\boldsymbol{m}_{n+1} \\
&= (\boldsymbol{F}_{n+1}\boldsymbol{M}_{n+1})\cdot\boldsymbol{F}_{n+1}\boldsymbol{S}_{n+1}^{\text{tr}}\boldsymbol{F}_{n+1}^{\mathsf{T}}(\boldsymbol{F}_{n+1}\boldsymbol{M}_{n+1}) \\
&= (\boldsymbol{C}_{n+1}\boldsymbol{M}_{n+1})\cdot(\boldsymbol{S}_{n+1}^{\text{tr}}\boldsymbol{C}_{n+1}\boldsymbol{M}_{n+1})\,.
\end{aligned}$$

Then there is additional irreversible strain when

$$\begin{aligned}
\alpha_{n+1} &= \left\langle \frac{\sigma_{n+1}^{\text{tr}}}{k_{n+1}^{\text{tr}}} - 1 \right\rangle = \left(\frac{\sigma_{n+1}^{\text{tr}}}{k_{n+1}^{\text{tr}}} - 1\right) > 0\,. \\
\lambda_{n+1}^{\text{irr}} &= \lambda_n^{\text{irr}} + \alpha_{n+1}(\Delta t_n/\tau_{\text{relax}}) \\
k_{n+1}^{\text{irr}} &= k_n^{\text{irr}} + \alpha_{n+1}(\Delta t_n/\tau_{\text{relax}})H_{n+1}^{\text{irr}}\,. \\
\boldsymbol{S}_{n+1} &= \boldsymbol{S}(\lambda_{n+1}^2/\lambda_n^{\text{irr}\,2})\,.
\end{aligned}$$

The derivative of the algorithmic 2nd P–K tensor becomes

$$\begin{aligned}
\mathbb{C}^{\text{algo}}_{n+1} &= 2\frac{\partial \boldsymbol{S}^{\text{algo}}_{n+1}}{\partial \boldsymbol{C}_{n+1}} = 2\frac{d\boldsymbol{S}(\lambda^{\text{el}\,2}_{n+1})}{d(\lambda^{\text{el}2}_{n+1})}\,\frac{\partial(\lambda^{\text{el}\,2}_{n+1})}{\partial \boldsymbol{C}_{n+1}} \\
&= 2\boldsymbol{S}'(\lambda^{\text{el}\,2}_{n+1})\,\frac{\partial}{\partial \boldsymbol{C}_{n+1}}(\lambda^2_{n+1}/\lambda^{\text{irr}\,2}_{n+1}) \\
&= 2\boldsymbol{S}'(\lambda^{\text{el}\,2}_{n+1})\left[\frac{1}{\lambda^{\text{irr}\,2}_{n+1}}(\boldsymbol{M}_n\otimes\boldsymbol{M}_n) - 2\frac{\lambda^2}{(\lambda^{\text{irr}}_{n+1})^3}\underbrace{\left(\frac{\Delta t_n}{\tau_{\text{relax}}}\right)}_{\ll 1}\left(\frac{1}{k^{\text{tr}}_{n+1}}\right)\left(\frac{\partial\sigma^{\text{tr}}}{\partial \boldsymbol{C}_{n+1}}\right)\right] \\
&\approx 2\boldsymbol{S}'(\lambda^{\text{el}\,2}_{n+1})\,\frac{1}{\lambda^{\text{irr}\,2}_{n+1}}(\boldsymbol{M}_n\otimes\boldsymbol{M}_n)\,. \qquad (34)
\end{aligned}$$

The approximation in the last line yields the same formula as for the earlier case of no new irreversible strain. The approximation is best when $0 < \Delta t_n \ll \tau_{\text{relax}}$. The other terms do not go to zero with a decrease in Δt_n, nor do they blow up. In addition, computation of the term $\partial\sigma^{\text{tr}}/\partial \boldsymbol{C}_{n+1}$ is costly.

Using this slightly inconsistent tangent works well.[3]

[3] Newton convergence even with the consistent tangent can still have problems due to the discontinuity introduced by the bracket $\langle\cdot\rangle$ in the definition of α. To solve this, I round off the corner of the bracket, like so:
Suppose

$$\begin{aligned}
&R \geqslant 0 \\
&a = R\cot(3\pi/8) \\
&b = a\cos(\pi/4) \\
&y = \sqrt{R^2-(x+a)^2}\,.
\end{aligned}$$

The radius of the fillet is R, the arclength to be swept is $\pi/4$, and the fillet lies within the interval $(-a, b)$.

$$\langle x\rangle_R = \begin{cases} 0 & x \leqslant -a \\ R-y & -a < x < b \\ x & x \geqslant b\,, \end{cases}$$

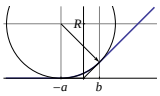

$$\frac{d\langle x\rangle_R}{dx} = \begin{cases} 0 & x \leqslant -a \\ \frac{a+x}{y} & -a < x < b \\ 1 & x \geqslant b\,. \end{cases}$$

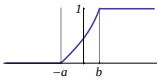

The final curve is C^1. To minimize the effect of the rounded bracket on the elastic regime, take $R \ll 1$. I are reassured of the friendliness of the rounded bracket by its behavior in the limit: as $R \to 0$, $\langle\cdot\rangle_R \to \langle\cdot\rangle_0 = \langle\cdot\rangle$, both pointwise and in mean. For this smoothing to have practical value, the (possibly adaptive) step size should create increments $(\alpha_{n+1} - \alpha_n)$ smaller than $b + a$ when α_n is near the fillet.

4.3 Newton-Raphson scheme

The BVP (GNR, G) is nonlinear; $\boldsymbol{F}$, $\boldsymbol{S}$, and $J = \det \boldsymbol{F}$ all depend on the motion $\boldsymbol{\varphi}^h$ (as does $\boldsymbol{M}^k_{\text{ref}}$, used below). To solve equations (33), I use the Newton-Raphson technique.

The Newton-Raphson scheme for this problem becomes

1. Choose relative and absolute error tolerances ε_{rel}, $\varepsilon_{\text{abs}} > 0$, a norm $\|\cdot\|$ of the residual, and begin with iteration number $\nu = 0$. Choose an initial guess $\left(\boldsymbol{U}^B_j\right)^\nu$ for the displacement.

2. Build the residual $\left(\boldsymbol{R}^A_i\right)^\nu$ (the residual in the i-th direction at node A) by evaluating equation (38) at guess $\left(\boldsymbol{U}^B_j\right)^\nu$.
   Build $\left(\frac{\partial \boldsymbol{R}^A_i}{\partial \boldsymbol{U}^B_j}\right)^\nu$ in the same way.

3. Suppose there is a solution to the following linear finite-dimensional problem and solve the expression for $\left(\Delta \boldsymbol{U}^B_j\right)^\nu$:

$$\left(\frac{\partial \boldsymbol{R}^A_i}{\partial \boldsymbol{U}^B_j}\right)^\nu \left(\Delta \boldsymbol{U}^B_j\right)^\nu = -\left(\boldsymbol{R}^A_i\right)^\nu . \tag{35}$$

4. Update the guess to $\left(\boldsymbol{U}^B_j\right)^{\nu+1} = \left(\boldsymbol{U}^B_j\right)^\nu + \left(\Delta \boldsymbol{U}^B_j\right)^\nu$. Increment ν.

5. Repeat steps 2–4 until $\left\|\left(\boldsymbol{R}^A_i\right)^\nu\right\| < \varepsilon_{\text{abs}}$, or $\left\|\left(\boldsymbol{R}^A_i\right)^\nu\right\| / \left\|\left(\boldsymbol{R}^A_i\right)^0\right\| < \varepsilon_{\text{rel}}$.
   When it does, define $\boldsymbol{U}^B_j$ as $\left(\boldsymbol{U}^B_j\right)^\nu$.

6. Obtain the displacement $\boldsymbol{U} = \boldsymbol{N}^B \boldsymbol{U}^B$, motion $\boldsymbol{\varphi}_t(\boldsymbol{X}) = \boldsymbol{U}(\boldsymbol{X}) + \boldsymbol{X}$, and deformation gradient

$$\boldsymbol{F} = \frac{\partial \boldsymbol{U}}{\partial \boldsymbol{X}} + \boldsymbol{I} = \frac{\partial \boldsymbol{N}^B}{\partial \boldsymbol{X}} \boldsymbol{U}^B + \boldsymbol{I} .$$

4.4 Data recovery procedure

Interesting data values such as stresses, mass growth, and fiber directions will only be calculated exactly at the gauss points on each element (or face). In order to extrapolate these values to the nodes (control points), I will use a least squares approximation technique. This method is used for computational efficiency at the expense of accuracy. The computed values are used for visualization only.

Suppose $f_i(\boldsymbol{X})$ is the i-th component of some vector-valued function $\boldsymbol{f}(\boldsymbol{X}) = f_i(\boldsymbol{X})\boldsymbol{e}_i$, defined on the reference configuration Ω_0, and whose exact values are known only at Gauss points: $f_i(\boldsymbol{X}(\boldsymbol{\xi}(\mathbf{gp}))) = f_i^{\mathbf{gp}}$.

Values of $\boldsymbol{f}(\boldsymbol{X})$ typically represent interesting data for the current configuration, and may perhaps be more properly represented as $\boldsymbol{f}(\boldsymbol{X}, t)$, but let us drop the time dependence for the sake of clarity; t shall not change in what follows. The same procedure will be applied at each timestep.

The goal of the stress recovery procedure is to find real values f_i^B for each node B and direction i such that the approximation $f_i^h(\boldsymbol{X}) = \boldsymbol{N}^B(\boldsymbol{X})f_i^B$ interpolates the exact values known at gauss points: $f_i^h(\boldsymbol{X}(\boldsymbol{\xi}(\mathbf{gp}))) = f_i^{\mathbf{gp}}$.

Converting to weak form as above gives an equation for each node A and direction i; namely,

$$\left(\boldsymbol{N}^A, \boldsymbol{N}^B f_i^B\right)_{\Omega_0} = \left(\boldsymbol{N}^A, f_i\right)_{\Omega_0},$$

leading to the Newton-Raphson equation

$$\left(\boldsymbol{N}^A, \boldsymbol{N}^B \delta_{ij}\right)_{\Omega_0} \left(\Delta f_j^B\right) = -\left(\boldsymbol{N}^A, \boldsymbol{N}^B f_i^B - f_i\right)_{\Omega_0}.$$

(See equation (35).) Approximating the integrals with Gaussian integration leads to something like (36) in Figure 18.

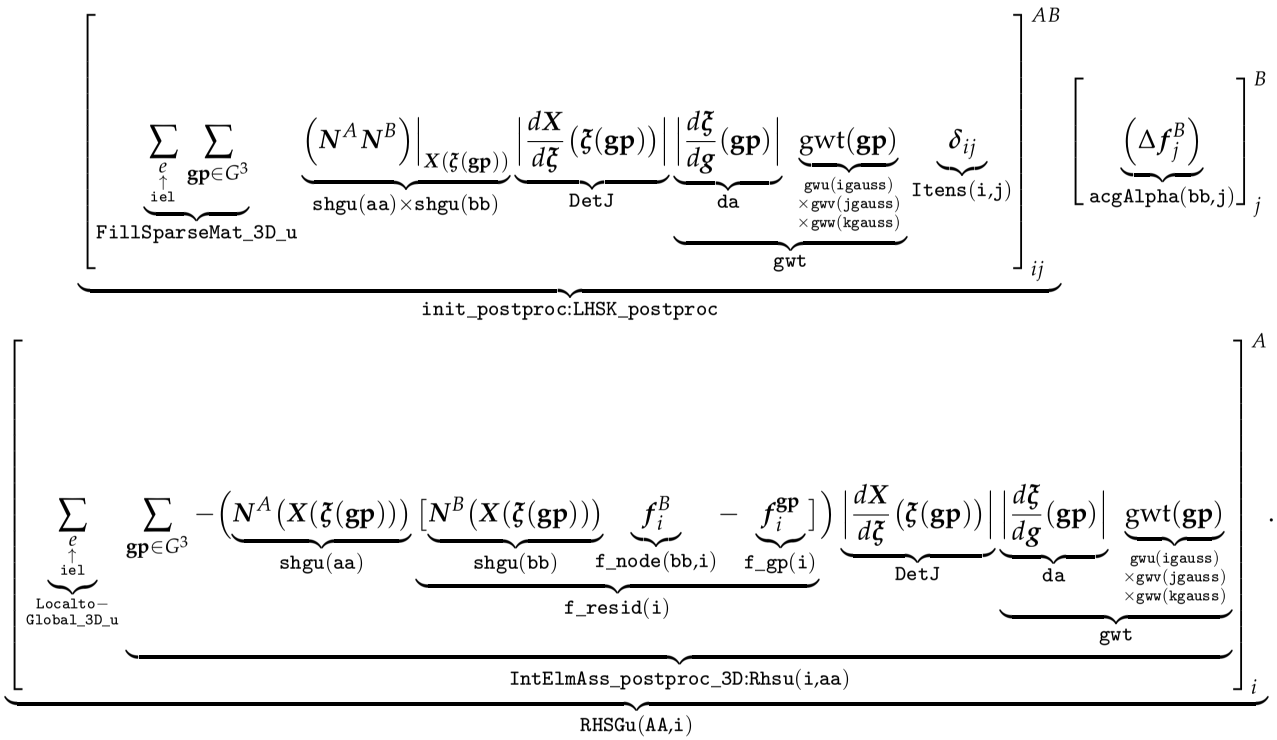

(36)

Figure 18: Gaussian integrals with variables indicated from the codebase. The terms are written in brackets with their free indices repeated outside the bracket for clarity to emphasize the matrix structure. Conveniently, equation (36) only requires knowledge of function values at arguments which have already been computed. Even better, the mass matrix here is constant with respect to the function being reconstructed and the current configuration; it only needs to be computed once *per mesh*. This is a considerable time savings as compared with reconstructing the entire GNR framework at each node.

The process for recovery of boundary data is identical, with the change that integrals are performed over faces (Γ_0) instead of volumes (Ω_0). See Figure 19.

4.5 Derivative of the residual $\boldsymbol{R}_i^A$

Taking the derivative of $\boldsymbol{R}_i^A$ with respect to $\boldsymbol{U}_j^B$ gives the following, where $\mathbb{C} = 2\,\partial \boldsymbol{S}/\partial \boldsymbol{C}$.

$$\boldsymbol{R}_i^A = \left(\frac{\partial \boldsymbol{N}^A}{\partial \boldsymbol{X}_J},\ \boldsymbol{F}_{iI}\boldsymbol{S}_{IJ}\right)_{\Omega_0} - \left(\boldsymbol{N}^A,\ Jh\boldsymbol{F}_{iI}^{-\mathsf{T}}\boldsymbol{N}_I\right)_{\Gamma_{h0}} . \tag{38}$$

$$\begin{aligned}\frac{\partial \boldsymbol{R}_i^A}{\partial \boldsymbol{U}_j^B} = &\left(\frac{\partial \boldsymbol{N}^A}{\partial \boldsymbol{X}_J},\ \delta_{ij}\frac{\partial \boldsymbol{N}^B}{\partial \boldsymbol{X}_I}\boldsymbol{S}_{IJ} + \boldsymbol{F}_{iI}\mathbb{C}_{IJKL}\boldsymbol{F}_{jL}\frac{\partial \boldsymbol{N}^B}{\partial \boldsymbol{X}_K}\right)_{\Omega_0} \\ &- \left(\boldsymbol{N}^A,\ Jh\left(\boldsymbol{F}_{Kj}^{-1}\frac{\partial \boldsymbol{N}^B}{\partial \boldsymbol{X}_K}\boldsymbol{F}_{Ii}^{-1} - \boldsymbol{F}_{Ij}^{-1}\frac{\partial \boldsymbol{N}^B}{\partial \boldsymbol{X}_K}\boldsymbol{F}_{Ki}^{-1}\right)\boldsymbol{N}_I\right)_{\Gamma_{h0}} .\end{aligned} \tag{39}$$

Let us confirm this result. It is important to have every index verifiably correct to recognize typos and debug code.

I slowly build up to the derivatives of the strain energy functions, the residual of a linear momentum equation, and viscoplasticity equations. I use a mix of vector notation and index notation. While vector notation is often elegant and beautiful, some expressions are insufficiently described without explicit indices. I also use the Einstein summation convention. In the summation convention, there is an implied sum over repeated indices:

$$\boldsymbol{F}\boldsymbol{S}\boldsymbol{F}^{\mathsf{T}} = \sum_{i=1}^{3}\sum_{I=1}^{3}\sum_{J=1}^{3}\sum_{j=1}^{3} \boldsymbol{F}_{iI}\,\boldsymbol{S}_{IJ}\,\boldsymbol{F}_{Jj}^{\mathsf{T}}\,(\boldsymbol{e}_i \otimes \boldsymbol{e}_j) = \boldsymbol{F}_{iI}\,\boldsymbol{S}_{IJ}\,\boldsymbol{F}_{Jj}^{\mathsf{T}}\,(\boldsymbol{e}_i \otimes \boldsymbol{e}_j) .$$

The first equality demonstrates the conversion from vector to index notation; the second equality demonstrates the Einstein summation convention; $\boldsymbol{e}_i$ for $i = 1, 2, 3$ are the basis vectors.

$$\underbrace{\left[\underbrace{\sum_{\substack{f\\ \uparrow\\ \texttt{ifac}}}^{\texttt{FillSparseMat\_3D\_u}}\sum_{\mathbf{gp}\in G^2}}_{\texttt{init\_postprocb:LHSK\_postprocb}}\underbrace{\left(N^A N^B\right)\Big|_{X(\xi(\mathbf{gp}))}}_{\texttt{shbu(aa)}\times\texttt{shbu(bb)}}\underbrace{\left|\frac{dX}{d\xi}(\xi(\mathbf{gp}))\right|}_{\texttt{DetJb}}\underbrace{\left|\frac{d\xi}{dg}(\mathbf{gp})\right|}_{\texttt{da}}\underbrace{\underbrace{\mathrm{gwt}(\mathbf{gp})}_{\substack{\texttt{gw(igaussb)}\\ \times\texttt{gw(jgaussb)}}}}_{\texttt{gwt}}\underbrace{\delta_{ij}}_{\texttt{Itens(i,j)}}\right]_{ij}^{AB}\left[\underbrace{\left(\Delta f_j^B\right)}_{\texttt{acgAlpha(bb,j)}}\right]_j^B}$$

$$=\underbrace{\left[\underbrace{\sum_{\substack{f\\ \uparrow\\ \texttt{ifac}}}^{\substack{\texttt{Localto}-\\ \texttt{Global\_3D\_u}}}\sum_{\mathbf{gp}\in G^2}}_{\texttt{RHSGu(AA,i)}}\underbrace{-\Big(\underbrace{N^A(X(\xi(\mathbf{gp})))}_{\texttt{shbu(aa)}}\underbrace{\left[\underbrace{N^B(X(\xi(\mathbf{gp})))}_{\texttt{shbu(bb)}}\underbrace{f_i^B}_{\texttt{f\_nodeb(bb,i)}}-\underbrace{f_i^{\mathbf{gp}}}_{\texttt{f\_gpb(i)}}\right]}_{\texttt{f\_resid(i)}}\Big)\underbrace{\left|\frac{dX}{d\xi}(\xi(\mathbf{gp}))\right|}_{\texttt{DetJb}}\underbrace{\left|\frac{d\xi}{dg}(\mathbf{gp})\right|}_{\texttt{da}}\underbrace{\underbrace{\mathrm{gwt}(\mathbf{gp})}_{\substack{\texttt{gw(igaussb)}\\ \times\texttt{gw(jgaussb)}}}}_{\texttt{gwt}}}_{\texttt{FaceAssembly\_postproc\_3D:Rhsu(i,aa)}}\right]_i^A}\quad . \tag{37}$$

Figure 19: Recovery of boundary data on nodes. Internal nodes are given Dirichlet conditions. (Otherwise, $\left(N^A, N^B\delta_{ij}\right)_{\Gamma_0}$ is not a full rank matrix.) The equations used are identical to Figure 18 on page 70, except integrals are performed over faces instead of volumes.

4.5.1 General formulas

I begin with simple expressions that are needed later.

The derivative of the trace of a matrix A with respect to A:

$$\frac{\partial \operatorname{tr} \boldsymbol{A}}{\partial \boldsymbol{A}_{ij}} = \frac{\partial}{\partial \boldsymbol{A}_{ij}} \boldsymbol{A}_{kk} = \boldsymbol{\delta}_{ik} \boldsymbol{\delta}_{jk} = \boldsymbol{\delta}_{ij} \,. \tag{40}$$

The derivative of the trace of the square of a matrix A with respect to A:

$$\frac{\partial \operatorname{tr}(\boldsymbol{A}^2)}{\partial \boldsymbol{A}_{ij}} = \frac{\partial}{\partial \boldsymbol{A}_{ij}} \left(\boldsymbol{A}_{k\ell} \boldsymbol{A}_{\ell k} \right) = \boldsymbol{\delta}_{ik} \boldsymbol{\delta}_{j\ell} \boldsymbol{A}_{\ell k} + \boldsymbol{A}_{k\ell} \boldsymbol{\delta}_{i\ell} \boldsymbol{\delta}_{jk} = \boldsymbol{A}_{ji} + \boldsymbol{A}_{ji} = 2\, \boldsymbol{A}_{ji} \,. \tag{41}$$

$$\frac{\partial \operatorname{tr}(\boldsymbol{A}^2)}{\partial \boldsymbol{A}} = 2\, \boldsymbol{A}^{\mathsf{T}} \,. \tag{42}$$

It is important to recognize that differentiation with respect to symmetric tensors is *not* the same as differentiation with respect to a nonsymmetric tensor. A symmetrization must occur over the differentiated indices. This will become apparent as the next few formulas emerge.

The derivative of a real-valued function $f(C)$ of a symmetric tensor C with respect to its argument:

$$\frac{\partial f(\boldsymbol{C})}{\partial \boldsymbol{C}_{ij}} = \left[\frac{\partial f(\boldsymbol{A})}{\partial \boldsymbol{A}} \right]_{(ij)} \Big|_{\boldsymbol{A}=\boldsymbol{C}} \,. \tag{43}$$

The derivative of a symmetric tensor C with respect to itself:

$$\frac{\partial \boldsymbol{C}_{kl}}{\partial \boldsymbol{C}_{ij}} = \Big[\delta_{ki}\delta_{lj}\Big]_{kl(ij)} = \frac{1}{2}\left(\delta_{ki}\delta_{lj} + \delta_{kj}\delta_{il}\right) \neq \Big[\delta_{ki}\delta_{lj}\Big]_{klij} . \tag{44}$$

Proof: Taking $f(\boldsymbol{C}) = \boldsymbol{C}_{kl}$ in (43) above,

$$\begin{aligned}\frac{\partial \boldsymbol{C}_{kl}}{\partial \boldsymbol{C}_{ij}} &= \Big[\frac{\partial \boldsymbol{A}_{kl}}{\partial \boldsymbol{A}_{ij}}\Big]_{(ij)}\Big|_{\boldsymbol{A}=\boldsymbol{C}} \\ &= \Big[\delta_{ki}\delta_{lj}\Big]_{kl(ij)}\Big|_{\boldsymbol{A}=\boldsymbol{C}} \\ &= \Big[\delta_{ki}\delta_{lj}\Big]_{kl(ij)} \\ &= \frac{1}{2}\left(\delta_{ki}\delta_{lj} + \delta_{kj}\delta_{il}\right) .\end{aligned}$$

The derivative of the trace of the square of a symmetric matrix C with respect to C:

$$\frac{\partial \operatorname{tr}(\boldsymbol{C}^2)}{\partial \boldsymbol{C}_{ij}} = 2\,\boldsymbol{C}_{(ji)} = 2\boldsymbol{C}_{ij} . \tag{45}$$

The derivative of the determinant of a matrix A with respect to A:

$$\frac{\partial}{\partial \boldsymbol{A}_{ij}} \det \boldsymbol{A} = (\det \boldsymbol{A})(\boldsymbol{A}^{-\mathsf{T}})_{ij} . \tag{46}$$

For a proof of this difficult result, see, for example, Example 1.10 on page 41 of [Holzapfel 2000].

The derivative of the inverse of a (nonsingular) matrix A with respect to A:

$$\frac{\partial A^{-1}_{ji}}{\partial A_{mn}} = -A^{-1}_{jm} A^{-1}_{ni} \,. \tag{47}$$

Proof: First, note that $A^{-1}_{jp} A_{pk} = \delta_{jk}$, and so if $(\,)^{\cdot}$ is some kind of derivative, then taking the $(\,)^{\cdot}$ derivative with respect to both sides and then right multiplying by A^{-1} gives

$$(A^{-1}_{jp})^{\cdot} A_{pk} + A^{-1}_{jp} (A_{pk})^{\cdot} = 0$$

$$(A^{-1}_{jp})^{\cdot} A_{pk} A^{-1}_{ki} + A^{-1}_{jp} (A_{pk})^{\cdot} A^{-1}_{ki} = 0$$

$$(A^{-1}_{jp})^{\cdot} \delta_{pi} + A^{-1}_{jp} (A_{pk})^{\cdot} A^{-1}_{ki} = 0 \,.$$

Using $(\,)^{\cdot} = \partial / \partial A_{mn}$, I see

$$(A^{-1}_{ji})^{\cdot} + A^{-1}_{jp} (A_{pk})^{\cdot} A^{-1}_{ki} = 0$$

$$\frac{\partial A^{-1}_{ji}}{\partial A_{mn}} + A^{-1}_{jp} \delta_{pm} \delta_{kn} A^{-1}_{ki} = 0$$

$$\frac{\partial A^{-1}_{ji}}{\partial A_{mn}} = -A^{-1}_{jm} A^{-1}_{ni} \,.$$

The derivative of the inverse of a (nonsingular) symmetric matrix C with respect to C:

$$\frac{\partial C^{-1}_{ji}}{\partial C_{mn}} = -\frac{1}{2} (C^{-1}_{jm} C^{-1}_{ni} + C^{-1}_{im} C^{-1}_{nj}) \,. \tag{48}$$

Proof: For each i and j, apply (47) and (44), using $f(\boldsymbol{C}) = \boldsymbol{C}^{-1}_{ji}$. The symmetrization occurs over m and n, but not i or j:

$$\begin{aligned}
\frac{\partial \boldsymbol{C}^{-1}_{ji}}{\partial \boldsymbol{C}_{mn}} = \frac{\partial f(\boldsymbol{C})}{\partial \boldsymbol{C}_{mn}} &= \Big[\frac{\partial f(\boldsymbol{A})}{\partial \boldsymbol{A}}\Big]_{(mn)}\Big|_{\boldsymbol{A}=\boldsymbol{C}} \\
&= \Big[\frac{\partial \boldsymbol{A}^{-1}_{ji}}{\partial \boldsymbol{A}_{mn}}\Big]_{(mn)}\Big|_{\boldsymbol{A}=\boldsymbol{C}} \\
&= \Big[-\boldsymbol{A}^{-1}_{jm}\boldsymbol{A}^{-1}_{ni}\Big]_{(mn)}\Big|_{\boldsymbol{A}=\boldsymbol{C}} \\
&= -\frac{1}{2}\big(\boldsymbol{A}^{-1}_{jm}\boldsymbol{A}^{-1}_{ni} + \boldsymbol{A}^{-1}_{im}\boldsymbol{A}^{-1}_{nj}\big)\Big|_{\boldsymbol{A}=\boldsymbol{C}} \\
&= -\frac{1}{2}\big(\boldsymbol{C}^{-1}_{jm}\boldsymbol{C}^{-1}_{ni} + \boldsymbol{C}^{-1}_{im}\boldsymbol{C}^{-1}_{nj}\big)\,.
\end{aligned}$$

4.5.2 Elasticity formulas

The derivative of the determinant $J^2 = \det \boldsymbol{C}$ with respect to $\boldsymbol{C} = \boldsymbol{F}^{\mathsf{T}}\boldsymbol{F}$:

$$\frac{\partial J^2}{\partial \boldsymbol{C}} = J^2\boldsymbol{C}^{-1}\,. \tag{49}$$

Proof: Equation (46) gives us $\dfrac{\partial J^2}{\partial \boldsymbol{C}} = \dfrac{\partial \det \boldsymbol{C}}{\partial \boldsymbol{C}} = (\det \boldsymbol{C})\boldsymbol{C}^{-\mathsf{T}} = J^2\boldsymbol{C}^{-1}$.

The derivative of the determinant $J = \det \boldsymbol{F}$ with respect to $\boldsymbol{C} = \boldsymbol{F}^{\mathsf{T}}\boldsymbol{F}$:

$$\frac{\partial J}{\partial \boldsymbol{C}} = \frac{1}{2}J\boldsymbol{C}^{-1}\,. \tag{50}$$

Proof: Observing $\frac{\partial J^2}{\partial \boldsymbol{C}} = 2J\frac{\partial J}{\partial \boldsymbol{C}}$ and equating it with (49) yields the result quite neatly.

The derivative of the inverse $J^{-1} = 1/(\det \boldsymbol{F})$ with respect to $\boldsymbol{C} = \boldsymbol{F}^{\mathsf{T}}\boldsymbol{F}$:

$$\frac{\partial J^{-1}}{\partial \boldsymbol{C}} = -\frac{1}{2J}\boldsymbol{C}^{-1} \,. \tag{51}$$

The derivative of the deformation gradient $\boldsymbol{F}$ with respect to displacement $\boldsymbol{U}$:

$$\frac{\partial \boldsymbol{F}_{iI}}{\partial \boldsymbol{U}_j^B} = \frac{\partial \boldsymbol{N}^B}{\partial \boldsymbol{X}_I}\boldsymbol{\delta}_{ij} \,. \tag{52}$$

Proof: First, note that

$$\boldsymbol{F}_{iI} = \frac{\partial}{\partial \boldsymbol{X}_I}\boldsymbol{\varphi}_i = \frac{\partial}{\partial \boldsymbol{X}_I}(\boldsymbol{I} + \boldsymbol{U}_i) = \boldsymbol{\delta}_{iI} + \frac{\partial \boldsymbol{U}_i}{\partial \boldsymbol{X}_I} \,,$$

and I am writing $\boldsymbol{N}^A = \boldsymbol{N}^A(\boldsymbol{X})$ as the basis functions at each node A:

$$\boldsymbol{U}_i = \boldsymbol{N}^A \boldsymbol{U}_i^A \,.$$

Then

$$\begin{aligned}
\frac{\partial}{\partial \boldsymbol{U}_j^B}\boldsymbol{F}_{iI} &= \frac{\partial}{\partial \boldsymbol{U}_j^B}\left(\boldsymbol{\delta}_{iI} + \frac{\partial \boldsymbol{U}_i}{\partial \boldsymbol{X}_I}\right) = 0 + \frac{\partial}{\partial \boldsymbol{U}_j^B}\frac{\partial}{\partial \boldsymbol{X}_I}\boldsymbol{U}_i = \frac{\partial}{\partial \boldsymbol{X}_I}\frac{\partial}{\partial \boldsymbol{U}_j^B}\boldsymbol{U}_i \\
&= \frac{\partial}{\partial \boldsymbol{X}_I}\frac{\partial}{\partial \boldsymbol{U}_j^B}(\boldsymbol{N}^A \boldsymbol{U}_i^A) = \frac{\partial}{\partial \boldsymbol{X}_I}\boldsymbol{N}^A\frac{\partial}{\partial \boldsymbol{U}_j^B}\boldsymbol{U}_i^A = \frac{\partial \boldsymbol{N}^A}{\partial \boldsymbol{X}_I}\boldsymbol{\delta}_{ij}\boldsymbol{\delta}_{AB} \\
&= \frac{\partial \boldsymbol{N}^B}{\partial \boldsymbol{X}_I}\boldsymbol{\delta}_{ij} \,.
\end{aligned}$$

The derivative of the inverse of $\boldsymbol{F}$ with respect to displacement:

$$\frac{\partial \boldsymbol{F}^{-1}_{Ii}}{\partial \boldsymbol{u}^B_j} = -\boldsymbol{F}^{-1}_{Ij}\frac{\partial \boldsymbol{N}^B}{\partial \boldsymbol{X}_K}\boldsymbol{F}^{-1}_{Ki} \ . \tag{53}$$

Using $(\ )^{\cdot} = \partial/\partial \boldsymbol{u}^B_j$ as in the proof of (47), and equation (52), I see that

$$\frac{\partial \boldsymbol{F}^{-1}_{Ii}}{\partial \boldsymbol{u}^B_j} = -\boldsymbol{F}^{-1}_{Ip}\frac{\partial \boldsymbol{N}^B}{\partial \boldsymbol{X}_K}\boldsymbol{\delta}_{pj}\boldsymbol{F}^{-1}_{Ki} = -\boldsymbol{F}^{-1}_{Ij}\frac{\partial \boldsymbol{N}^B}{\partial \boldsymbol{X}_K}\boldsymbol{F}^{-1}_{Ki} \ .$$

The derivative of the determinant $J = \det \boldsymbol{F}$ with respect to displacement:

$$\frac{\partial J}{\partial \boldsymbol{u}^B_j} = J(\boldsymbol{F}^{-\mathsf{T}})_{jQ}\,\frac{\partial \boldsymbol{N}^B}{\partial \boldsymbol{X}_Q} \ . \tag{54}$$

Proof: This follows easily from the formula (46) for the derivative of the determinant function.

In particular,

$$\frac{\partial J}{\partial \boldsymbol{u}^B_j} = \frac{\partial J}{\partial \boldsymbol{F}_{pQ}}\frac{\partial \boldsymbol{F}_{pQ}}{\partial \boldsymbol{u}^B_j} = J(\boldsymbol{F}^{-\mathsf{T}})_{pQ}\,\boldsymbol{\delta}_{pj}\,\frac{\partial \boldsymbol{N}^B}{\partial \boldsymbol{X}_Q} \ ,$$

giving the desired result.

The derivative of the Cauchy-Green strain tensor $\boldsymbol{C} = \boldsymbol{F}^{\mathsf{T}}\boldsymbol{F}$

with respect to $\boldsymbol{F}$:

$$\frac{\partial \boldsymbol{C}_{KL}}{\partial \boldsymbol{F}_{pQ}} = \frac{\partial}{\partial \boldsymbol{F}_{pQ}}(\boldsymbol{F}_{iK}\boldsymbol{F}_{iL}) = \boldsymbol{\delta}_{pi}\boldsymbol{\delta}_{QK}\boldsymbol{F}_{iL} + \boldsymbol{F}_{iK}\boldsymbol{\delta}_{pi}\boldsymbol{\delta}_{QL} = \boldsymbol{\delta}_{QK}\boldsymbol{F}_{pL} + \boldsymbol{F}_{pK}\boldsymbol{\delta}_{QL}\,. \tag{55}$$

The derivative of the Second Piola-Kirchhoff tensor $\boldsymbol{S}$

with respect to displacement:

$$\frac{\partial \boldsymbol{S}_{IJ}}{\partial \boldsymbol{u}^B_j} = \mathbb{C}_{IJKL}\boldsymbol{F}_{jL}\frac{\partial \boldsymbol{N}^B}{\partial \boldsymbol{X}_K}\,. \tag{56}$$

Proof: Note that $\mathbb{C}_{IJKL}$ is equal to $\partial \boldsymbol{S}_{IJ}/\partial \boldsymbol{E}_{KL} = 2\,\partial \boldsymbol{S}_{IJ}/\partial \boldsymbol{C}_{KL}$. Then use the above formulas to achieve

$$\frac{\partial \boldsymbol{S}_{IJ}}{\partial \boldsymbol{u}^B_j} = \frac{\partial \boldsymbol{S}_{IJ}}{\partial \boldsymbol{C}_{KL}}\frac{\partial \boldsymbol{C}_{KL}}{\partial \boldsymbol{F}_{pQ}}\frac{\partial \boldsymbol{F}_{pQ}}{\partial \boldsymbol{u}^B_j} = \frac{1}{2}\mathbb{C}_{IJKL}\left(\boldsymbol{F}_{jL}\frac{\partial \boldsymbol{N}^B}{\partial \boldsymbol{X}_K} + \boldsymbol{F}_{jK}\frac{\partial \boldsymbol{N}^B}{\partial \boldsymbol{X}_L}\right).$$

But $\mathbb{C}$ enjoys minor symmetry (generously provided by the symmetry of $\boldsymbol{C}$): $\mathbb{C}_{IJKL} = \mathbb{C}_{IJLK}$. Thus renaming index K as L and index L as K gives

$$\begin{aligned}
\frac{\partial \boldsymbol{S}_{IJ}}{\partial \boldsymbol{u}^B_j} &= \frac{1}{2}\mathbb{C}_{IJKL}\left(\boldsymbol{F}_{jL}\frac{\partial \boldsymbol{N}^B}{\partial \boldsymbol{X}_K}\right) + \frac{1}{2}\mathbb{C}_{IJLK}\left(\boldsymbol{F}_{jK}\frac{\partial \boldsymbol{N}^B}{\partial \boldsymbol{X}_L}\right) \\
&= \frac{1}{2}\mathbb{C}_{IJKL}\left(\boldsymbol{F}_{jL}\frac{\partial \boldsymbol{N}^B}{\partial \boldsymbol{X}_K}\right) + \frac{1}{2}\mathbb{C}_{IJKL}\left(\boldsymbol{F}_{jL}\frac{\partial \boldsymbol{N}^B}{\partial \boldsymbol{X}_K}\right) \\
&= \mathbb{C}_{IJKL}\left(\boldsymbol{F}_{jL}\frac{\partial \boldsymbol{N}^B}{\partial \boldsymbol{X}_K}\right).
\end{aligned}$$

Then by plugging in the results above, I directly derive

The derivative of the residual

$$\boldsymbol{R}_i^A = \left(\frac{\partial \boldsymbol{N}^A}{\partial \boldsymbol{X}_J},\ \boldsymbol{F}_{iI}\boldsymbol{S}_{IJ}\right)_\Omega - \left(\boldsymbol{N}^A,\ Jh\boldsymbol{F}_{Ii}^{-1}\boldsymbol{N}_I\right)_\Gamma$$

with respect to displacement:

$$\begin{aligned}\frac{\partial \boldsymbol{R}_i^A}{\partial \boldsymbol{U}_j^B} = &\left(\frac{\partial \boldsymbol{N}^A}{\partial \boldsymbol{X}_J},\ \delta_{ij}\frac{\partial \boldsymbol{N}^B}{\partial \boldsymbol{X}_I}\boldsymbol{S}_{IJ} + \boldsymbol{F}_{iI}\mathbb{C}_{IJKL}\boldsymbol{F}_{jL}\frac{\partial \boldsymbol{N}^B}{\partial \boldsymbol{X}_K}\right)_\Omega \\ &- \left(\boldsymbol{N}^A,\ Jh\left(\boldsymbol{F}_{Ii}^{-1}\frac{\partial \boldsymbol{N}^B}{\partial \boldsymbol{X}_K}\boldsymbol{F}_{Kj}^{-1} - \boldsymbol{F}_{Ij}^{-1}\frac{\partial \boldsymbol{N}^B}{\partial \boldsymbol{X}_K}\boldsymbol{F}_{Ki}^{-1}\right)\boldsymbol{N}_I\right)_\Gamma .\end{aligned} \tag{57}$$

Chapter 5

Building smooth meshes for isogeometric analysis

In the context of this work, the term "model" refers to a mathematical representation of the *geometry* of a given object. In particular, the representation—the model—must be a representation on which one can perform computations. This restriction distinguishes modeling from visualization, which can rely on the observer's ability to extract information from a representation that is obscured. Visual representations can tolerate high levels of noise, registration mismatches, confounding of nearby objects, and imprecise measurements. Models for computation cannot. Objects I model for this work will be either organs in the body (a section of artery or perhaps a heart) or idealized shapes reminiscent of such organs.

Reference to a modeling "pipeline" indicates a specific procedure of modeling an organ from noninvasive medical imaging data.

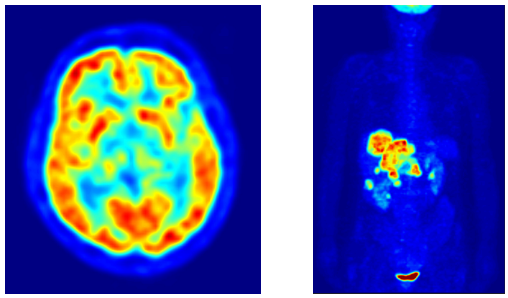

Figure 21: Representative images from PET scans. PET scans show organ function. As with CT or MR, PET can show three dimensional data. See, for example, `https://en.wikipedia.org/wiki/File:PET-MIPS-anim.gif`. [Langner 2010]

5.1 Choosing medical image modalities

There are many medical imaging technologies available for engineering analysis. Carefully choosing a format which is conducive to the analysis to be done is important, and translating engineering terminology and needs into clinical terminology takes many discussions. Here I explore various imaging technologies and their uses in engineering analysis and their suitability for this work in particular.

5.1.1 Positron Emission Tomography (PET)

PET scans provide physiological information about the organ in question (usually the heart, brain, or cancerous tumors): "Which parts are getting blood, and how much do they get?" or "We think you have tumor X. Tracer Y, we find, concentrates primarily in type X tumors. We will inject tracer Y, then take a picture." Physiological information (ie, "Is this tissue metabolically active?") is as opposed to anatomical information (ie, "What tissue is right here?").

A radioactive isotope is incorporated with special sugars that concentrate in the desired tissues, and is injected into the bloodstream. The sugars go to the right places, be-

Modality	spatial resolution (mm) (approx.)	temporal resolution (ms) (approx.)	primary advantages	primary disadvantages
MR	$1 \times 1 \times 2$	30–50	good soft tissue contrast; 6D/7D information; freely orientable field of view; allows blood velocity data; **safe, nontoxic**	time-consuming; expensive; scanning ability impared by arrhythmia and irregular breathing; contraindications exist (e.g.: pacemakers, pregnancy)
CT	$0.6 \times 0.6 \times 1$	100–150	fast acquisition time; high spatial resolution; high dynamic range; **clinical standard for many applications**	moderate soft tissue contrast; high radiation dose; nephrotoxic contrast agents; low temporal resolution; no velocity data
Ultrasound	1×2 $(\times 8)$	30–50	fast, simple, inexpensive, portable, safe, nontoxic; allows velocity data	poor soft tissue contrast; acoustic window limitations; low spatial resolution

Table 20: Comparison of imaging modalities for arteries. I chose MR for initial imaging for its good resolution, and because it is safe and nontoxic, thus good for experimental use. I chose CT for patient-specific modeling because it is a clinical standard for aneurysm diagnosis.

cause after fasting the body (healthy tissue) isn't able to process the sugars, while cancerous tissue can!

The isotope decays, emitting a positron. When the positron strikes an electron, they annihilate, emitting two gamma particles that travel in exactly opposite directions. ($e^+ + e^- = 2\gamma$.) Detectors backsolve to find the decaying isotope's position. Integrating and normalizing gives images something like Figure 21.

Diseased metabolism and tumors are immediately apparent with abnormal distribution of the isotope. This is the hallmark of good visualization: that it doesn't take a doctorate to understand the image's basic revelations.

PET is capable of good quality images—its resolution is ~5mm. It has some data resolution limitations:

- Positrons can travel a few millimeters before finding an electron.
- The gamma rays are not detected as exactly 180 degrees apart. This occurs if one of the gamma rays is deflected into another detecting sensor. In this case, the machine will mis-calculate the annihilation location.
- Detector resolution is itself limited.

A somewhat recent improvement for tumor detection in PET scanning is to include a CT scanner in the same device. (Not all PET imaging techniques use CT.) The CT scan provides anatomical information, and the fact that they are acquired together permits easy registration of the two datasets. A physician thus can tell clearly what anatomy produced the bright or dim spot, rather than guess based on experience. This isn't always easy: for instance, it's subtle but crucial to know whether a tumor is above or below the diaphragm.

Software clinicians use to read PET/CT scans display both the PET and CT image side by side; and there are two cursors, hovering over the same spot in each image.

From an oncological perspective, good tracers are highly nontrivial to create. All of these things must be accomplished:

- binding the tracer to a sugar (or other metabolically active material)
- finding a sugar that is taken up by a cancerous tumor, or, more commonly:

  finding a type of tumor that takes up your sugar (the tumor should be one I can't already image better another way)
- developing a procedure (such as fasting for 24 hours) which causes the sugar to be taken up selectively by the tumor
- constructing a detector sensitive enough for your application
- mass-producing the above solution.

Each of the above tasks is probably worth a PhD or two (or five). The way we do the above for most tumors is pretty interesting, but beyond the scope of this work.

The half-lives of the isotopes used in PET scanning are short:

isotope	half-life (min)	medical applications
Rubidium-82	1.25	cardiac
Oxygen-15	2.1	neuro, some cardiac application
Nitrogen-13	10	cardiac
Carbon-11	20.4	cardiac
Fluorine-18	110	cardiac, neuro, skeletal, esp. for distant cyclotrons

Patients are done "glowing" by the time they leave the facility.

5.1.2 Single Photon Emission Computed Tomography (SPECT)

SPECT imaging, like PET, provides physiologic information of the body by detecting the decay of a radioactive substances. A radioactive isotope is injected into the body,

and the protons emitted when it decays are detected. PET and SPECT are extremely similar, and are therefore used in essentially the same fashion. (For instance, SPECT is also coupled with CT.) Pointless debates occasionally rage over the value or cost of SPECT versus PET, and most institutes will choose to support only one. But every major medical center must have both available, as both are crucial; they use different classes of radiotracers, which are taken up better by different classes of tumors.

5.1.3 Magnetic Resonance Imaging (MRI)

MRI (or MR) is a technique for retrieving anatomical data about the body. "What tissue lies at position (x, y, z)?" (Recall that PET and SPECT illuminate physiologic data about the body. "Is this tissue metabolically active?") MR can acquire fluid velocity data, too, if pressed, and can show displacements of solids (in a limited manner). MR's spatial and temporal resolution is excellent (~1mm^3 spatially and ~40ms temporally, with research devices achieving ~1um^3 spatially), it has enviable soft tissue contrast, is moderately free from artifacts, and is nontoxic. Unfortunately, it's expensive ($3-4M, plus $4-700K/yr in electricity and upkeep), time-consuming, heavy, and loud. (See Table 20 on page 83.)

Major MR departments, especially in competitive environments (defined by geography or research area), often upgrade each machine every three years. The old machines go to other hospitals, other countries, and veterinarians.

MR imaging of the brain creates exceptionally clear images quickly. This is because the brain doesn't move. Cardiac MR suffers from registration artifacts caused by the heart's movement. Only a small portion of the heart can be imaged during the short period of rest between heartbeats, and because the heart doesn't return to exactly the same position each

time, and because people need to breathe (which moves the heart around). I once heard a Cardiac MR researcher quip, "MR is the worst modality for scanning the heart."

Creating a good scan uses tricks and takes a long time (forty-five minutes). The main tricks are detecting the location of the diaphragm and the QRS complex of the electrocardiograph (EKG); when both of them are in just the right place, scanning is done. This is a free-breathing scan, where the patient just lies there, preferably asleep (but usually bored, and sometimes claustrophobic). There are also breathhold scans.

MRI devices work by creating huge magnetic fields around the patient's body, aligning a mere O(.001%) of the protons in the body, and detect the tiny magnetic fields produced as the protons realign with the Earth. MR detects all atoms with an odd number of protons, which means it detects hydrogen. (No other atom with an odd atomic weight occurs in the body in any significant concentration.) The vast majority of hydrogen exists in either water or fat. So we distinguish soft tissues by their relative concentrations of water and fat, and we tune the MR machine's sequences to improve the distinction between the two. Bone and air are easily distinguished, as are blood, muscle, and most other tissues.

The magnetic field together with radiofrequency pulses "tag" the protons with their location in space, and the location is read back a short time later. This is a way of acquiring velocity data (for blood) or mechanical motion (for the heart). For a still image of the heart, the tagging and reading are done while the heart is at rest. Naturally, heart rate control is a routine preparation for MRI. The time interval between tagging and reading is not arbitrary. (For more information, read about "relaxation time" and "T1- and T2-weighted imaging" in any relevant resource. The time intervals used are prescribed by the organ being observed.

As with CT, contrast injection is routinely used to highlight certain anatomy or physiology. Clinically-useful tricks allowed with contrast injection number in the dozens; research tricks in the thousands.

MR, being safe, is a popular research tool. It is generally used for neurologic applications for its soft tissue contrast, where CT and PET/SPECT are entirely lacking. Grey matter is largely water, and white matter is largely fat. For cardiac applications, MR is generally used for anatomic reconstruction, perfusion, and viability.

The fields produced by the machine are believed not to be harmful to humans. That said, pacemakers could malfunction—they are, in fact, an absolute contraindication. Not only could the pacemaker's electronics malfunction temporarily or permanently due to MR, but the changing magnetic field could induce electric current in the pacemaker leads. Either could to improper pacing shocks, causing fatal arrhythmia. Implanted or embedded metal will typically heat up or move, at least a little bit. Pregnant women, as a precaution, should avoid MR, especially in the first trimester; plenty of better-understood alternatives exist.

MR artifacts are anisotropic, colloquially referred to as "graininess." Anisotropic diffusion filtering is the standard fix.

Metal implants disrupt the magnetic field, causing "washout" artifacts. Even a thin wire can create a black cylinder in one's dataset an inch in diameter. Special "MRI-safe" versions of implantable devices are frequently used. A nickel titanium blend, Nitinol, is the frontrunning material.

The huge magnetic fields produced by the magnet switch on and off very rapidly. Especially in high-power magnets, this can cause peripheral nerve stimulation. (The pace-

maker restriction is primarily due to the ability of the magnetic fields to generate pacing-level currents in the pacemaker leads. The pacemaker circuitry itself can also become destroyed.) Patients undergoing MR report twitching sensations, particularly in the extremities.

I had an MRI scan performed for the purpose of creating the model in Figure 1. Myself, I knew when the machine was scanning me, because I could "hear" the changing magnetic field—before it made a noise—through a sensation in the base of my neck. *Bzzt! Bzzt! Bzzt!*

The gradient field is zero at the center of the magnet, and increases linearly with distance along the body axis (or whatever axis one chooses). Therefore, when scanning the brain, these new high-powered magnets can generate current in the heart. This situation is, to put it mildly, arrhythmogenic. It is common around the world to prescribe safety limits on the amount of change $|d\boldsymbol{B}/dt|$ of the magnetic field $\boldsymbol{B}$ per unit time.

The magnetic fields produced by the magnet cause the coils producing them to warp, creating noise. Procedures can be up to 100–130 dB, which is at or above the threshold of pain. (Think of standing fifty feet from a jet engine at takeoff.) New machines are quieter, but patients still wear either earplugs or headphones, bringing the noise level down to that of a nightclub or a busy restaurant. High-quality acoustic insulation, active noise cancellation, and mandated limits on $d\boldsymbol{B}/dt$ all help. Modern MR installations provide virtual reality goggles so patients can watch a movie.

5.2 Segmentation of patient-specific organ geometries

As preliminary efforts, I modeled the heart (Figure 1 on page 2), abdominal aortic aneurysms (Figure 4b on page 8), thoracic cavity (Figure 3 on page 6), coronaries (Figure 24 on page 97), pulmonary arteries (Figure 25 on page 98), and many other organs.

5.3 Heart modeling pipeline

As a preliminary project for this work, I built an accurate (1 mm resolution) 3D model of a living human heart (see Figure 1 on page 2). I collected software tools for physical modeling of medical data, and devised a data flow pipeline to link them into a system for modeling organs in the body (see Figure 7 on page 14).

The work elucidated many challenges involved in modeling organs from noninvasive imaging. It demonstrated the utility of building patient-specific models by emphasizing differences between patients: the branching pattern of the coronaries, location and numbers of pulmonary veins, and the thickness, size, and shape of the left ventricle.

One of the most important challenges in medical image modeling is finding an imaging modality which has the capabilty to provide the information required. Essentially all clinical imaging is either physiologic in nature or designed for visualization. Obtaining a dataset of blood vessles with anatomic data involves either contrast-enhanced CT, which provides only blood boundaries, or MRI, which contains significant noise. In addition, people who are knowledgable of imaging protocols for visualization are usually not knowledgable of the issues in geometric modeling, and vice-versa. And rather than abandon clinical visualization, one must recognize the vast understanding of the human body built with visualizations. Utilizing this in a way that benefits both visualization and modeling communities is key.

Once a data set has been obtained, the challenge is to find segmentation techniques which are both sensitive to the organ being tested and at the same time robust to noise and registration errors inherent in the modality. For instance, cardiac CT requires multiple heartbeats in which to obtain a picture, and multiple datsets are (imperfectly) fused into one. (See §5.6 Coronaries below.) Cardiac MR, on the other hand, has mechanisms to reduce registration issues, but it suffers from a "graininess" that benefits from careful application of anisotropic diffusion filtering.

After the organ being modeled has been located within one's dataset, a geometry can be made to match. Again, each organ and modality requires a separate technique. For the heart shown in Figure 1, manual segmentation was used to create a finite element mesh.

5.4 Rapid prototyping

A triangle mesh from image data was fed into a rapid prototyping machine to create a physical model representing the subject's heart. A physical model is an extremely valuable tool for stimulating innovation in computational modeling. A physical version constructed from the model is one of the few ways to see the organ separated from its surroundings.

It can be used for visualization as a way for physicians to understand the subtle differences a particular patient is presenting which may not have been emphasized with usual methods. For instance, a cardiologist treating a diabetes patient's cold foot will glance at a previously-obtained MRI or CT scan, but make nearly all clinical treatment decisions based on a catheterization. Catheterization has an advantage over MR and CT in that it can show the flow rate, as sites of sluggish flow versus good, fast flow. But it can only provide a 2D projection of the arteries, and the cardiologist rarely makes an effort to observe another an-

gle because s/he can provide good treatment without the added radiation dose. A physical model built from the original MR or CT dataset can give all three dimensions quickly and easily. There is a push lately, with the recognition of vulnerable placques, toward understanding the value of knowing a blockage's three dimensional makeup. A physical model built with rapid prototyping is cheap, easy, and can help physicians give better care.

It is a teaching tool. The physician can use the physical object to point to, when discussing the treatment with the patient or a colleague, and the patient can take it home as a way of continuing to observe the geometry and learn from it. Better patient understanding of treatments and better means of patient-to-friends communication regarding medical care will stimulate and improve common understanding of medicine.

It is an experimental tool since a researcher can use it to simulate different situations that cannot be observed by any reliable technique. Exercise physiology, for instance, is nearly impossible to measure in natural conditions. There are enough difficulties measuring internal blood pressures and flow rates in a person who is still; doing it during exercise or in a patient's daily routine is a problem not likely to be solved soon. Physical experimentation with physiologic variables at exercise levels will improve understanding of the human body.

5.5 Aortas

I applied the heart pipeline (seen in Figure **??**a) to a study of coronary arteries. The data was anatomical data similar to the sort used for cranial arteries, and from them, I built a thoracic aorta, abdominal aortas, and I simulated interventions. The segmentation has been done by hand (from MRI) and with thresholding techniques (from gated CT angiography).

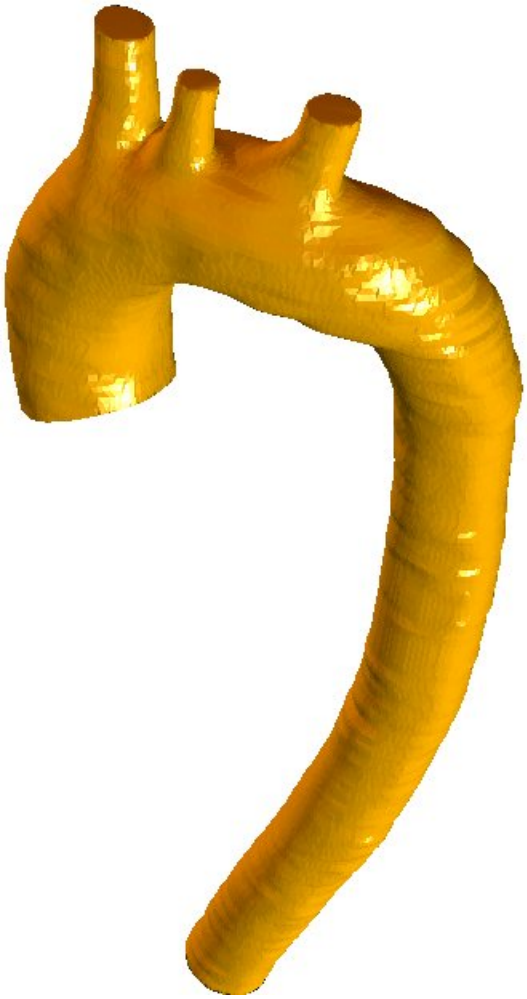

Figure 22: Mesh of thoracic aorta from MRI. Different imaging modalities (CT, MR, etc.) give rise to different segmentation techniques (thresholding, marching cubes, manual segmentation, etc.). This was a triangle mesh segmented by hand, of the authors' own aorta. This mesh was used in [Bazilevs].

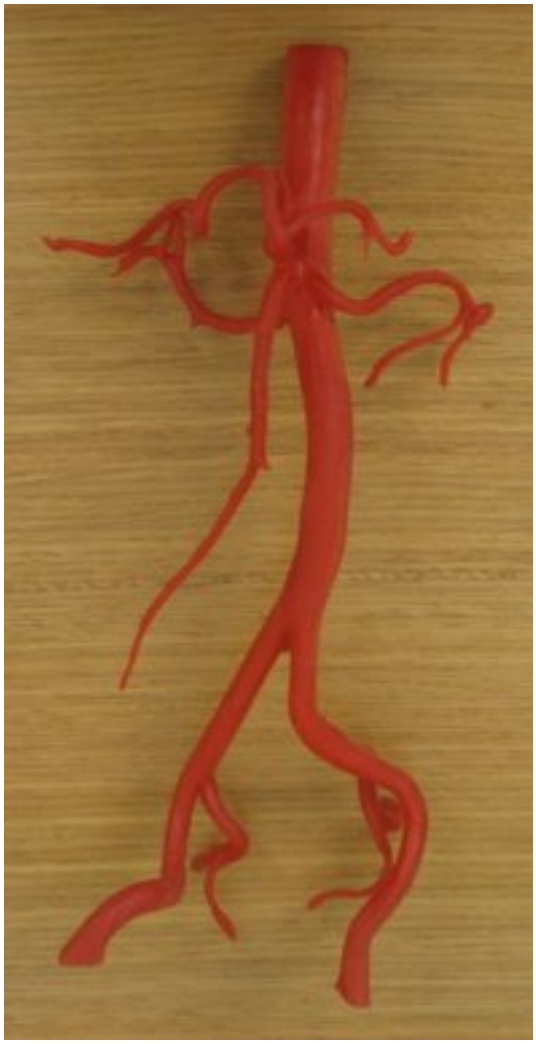

Figure 23: Physical model of an abdominal aorta from CT. This was 3D printed using selective laser sintering (SLS) with a soft rubber-like material. Settings were used such that the material has properties similar to that of arteries. After printing, the artery tree was infused with a coloring and fixing agent to take on a red hue and protect and seal the object's surface. The superior mesenteric artery and celiac artery trunk are visible, as well as the renal arteries and iliacs. More interesting is that placque buildup in the internal iliac and renal arteries is also visible.

Computationally-valid aortic models were built. MRI and (gated) CT are both suitable for building the models. (See Figure 22 and Figure 23 on the previous page.)

I modeled a throacic aorta from 4D phase-contrast MRI data. The segmentation was done by hand with a pen tablet using amira, a commercial software package developed for computing with medical data. The program is pipeline-oriented (See Figure 7b). It has numerous modules for image processing, including the entire Insight Segmentation and Registration Toolkit [itk.org]. Its meshing system takes a 3D data set and an arbitrary selection of pixels (representing the tissue of interest) and outputs a triangular or tetrahedral mesh.

I used amira's smoothing routines to remove wrinkles, then converted the triangle mesh to a computationally-ready hexahedral mesh using in-house software. The solid hexahedral mesh was then summarized by a skeletonization process into a midline and radii. Branches were represented by branches in the midline. The geometry of the ostia was approximated using specialized template pieces.

An experiment was set up using this geometry in which flow comparisons were made between a common-practice medical treatment (placement of left ventricular assist device output into the descending aorta) and a promising alternative (placement in the ascending aorta). The experiment confirmed the researchers' suspicion that the alternate treatment promoted better flow in the aorta throughout the cardiac cycle. It supported the findings of a clinical study comparing outcomes of the two alternatives [Kar 2005]. The result is a convincing argument in favor of performing the alternative treatment.

This demonstrates the utility of applying engineering analysis to clinical problems and the necessity of doing so for physician buy-in to new treatments.

5.6 Coronaries

I used a seed-based segmentation technique. A two-dimensional seed was placed in the first slice, and a region was grown around the seed up to a brightness cutoff; the cutoff was chosen based on the seed pixel's brightness.

To extend the selected region in three dimensions, I used the following approach. The brightest pixel directly below the previous slice's selected region was chosen as the seed for the new slice. A two-dimensional region was grown as before, and the process repeated. I defined the process as complete when the region size went to four pixels or less, or when the new seed point was darker than the previous cutoff. The process completing indicated either the artery had curved away, effectively ended, or there was a registration defect. Manual clean-up was required, as well as smoothing and then a manual distinction between arteries and veins. See Figure 24 on the following page.

The patency of the lumen is good throughout the coronaries and faithfully depicts the geometry of the image, including the image's inaccuracies. Note, for instance, the registration defect in the LAD past the second branch in Figure 24a; though 64-slice CT is fast, it is not fast enough to image the entire heart in one pass. Registration defects in cardiac CT imaging will persist until CT makes at least a fivefold speed increase.

Also notice the jagged lumen in the distal half of the Ramos branch. This shows that that the contrast agent has diffused into the myocardium, obscuring the branch's lumen. This artifact cannot be removed—indeed, the coronary veins are imaged by timing the contrast agent's passage from arteries to myocardium to veins. Two boluses of contrast agent are given so that, in a single imaging pass, the arteries and veins are both lit.

The diffusion artifact could possibly be removed after a few test runs for timing and by using separate imaging passes for the arteries and veins. But this creates two worse problems: compounded registration issues, and a much higher toxicity from both the x-rays and the contrast agent. Also, distinguishing those vessels is not clinically useful; cardiologists let Ramos branches and vessels less than 1 mm fend for themselves.

Tools are being developed to build mesh geometry automatically directly from medical image data.

I use isogeometric analysis technologies, which properly describe idealized geometries, and are good at representing patient-specific organic structures.

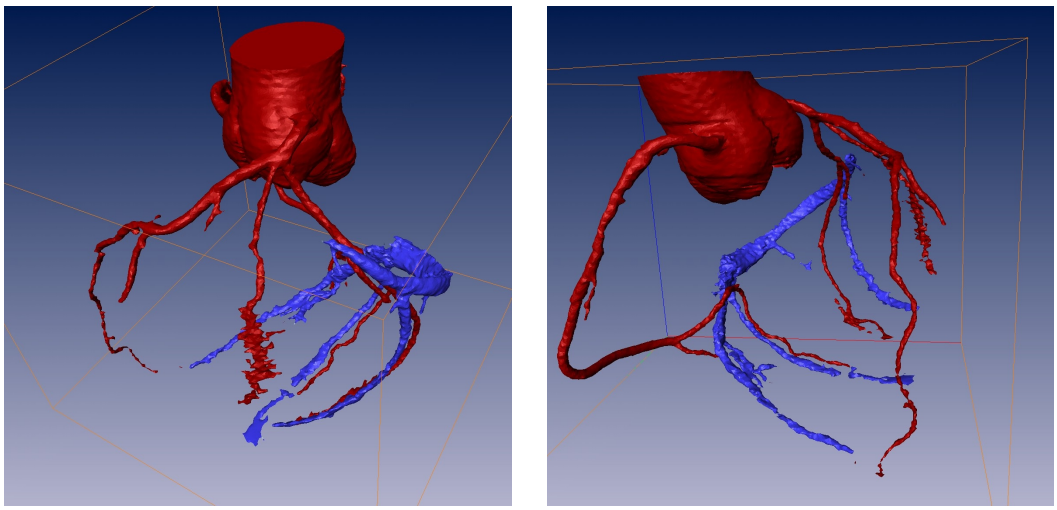

(a) This orientation features the left coronary artery. Visible is the LAD (at left), LCX (at right), and an unusual Ramos branch in the middle. Notice that veins tend to run alongside arteries. This makes them hard to distinguish.

(b) The right coronary artery is visible on the left side of the image, and the large coronary sinus in blue is adjacent to the aortic root.

Figure 24: Subject-specific coronary arteries from gated contrast-enhanced CT. The coronary arteries and aortic root are red, the veins blue. Notice the subject has few major diagonal branches off either the left anterior descending artery (LAD) or left circumflex (LCX); the Ramos branch perfuses the tissue instead.

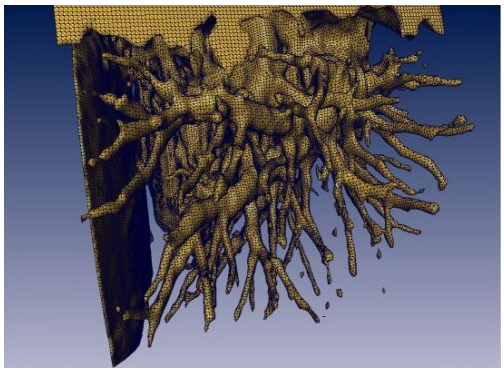

Figure 25: Tetrahedral mesh of pulmonary arteries from MR data using the image processing portion of the pipeline in Figure 7a. Anisotropic diffusion filtering was applied to the MR data. The boundary was defined by a "best fit" to a surface extracted by thresholding. This mesh was built for studying inverse problems in human imaging.

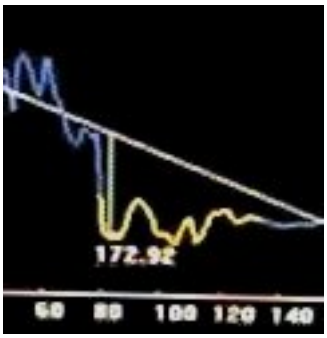

Figure 26: Automatic location of a stenosis in a user-chosen segment of artery with Philips' "Computer-Assisted Aneurysm Analysis" package for their *Allura* 3D-RA, in use at a local hospital. The curve shows actual diameter (in mm) between the endpoints. The section of curve in yellow indicates the stenosis. The point of greatest deviation is marked. Location of aneurysms is analogous.

5.7 Cranial arteries

For cranial arteries, a realistic curved section of artery was built in the computer-aided design package Rhinoceros3D. See Figure 27. MRI data was obtained from a healthy subject at risk for cranial aneurysms. An at-risk cranial artery was selected (posterior communicating artery). The artery lumen was approximated for a section of the artery, and a centerline derived. The model's geometry was built by lofting between proximal and distal diameter measurements.

5.8 Geometry and mesh

There is high bending present at the neck of a saccular aneurysm, so I strive to model tissues with an appropriately low bending stiffness. Also, my numerical method should not introduce artificial bending stiffness. To that end, I choose to use a smaller

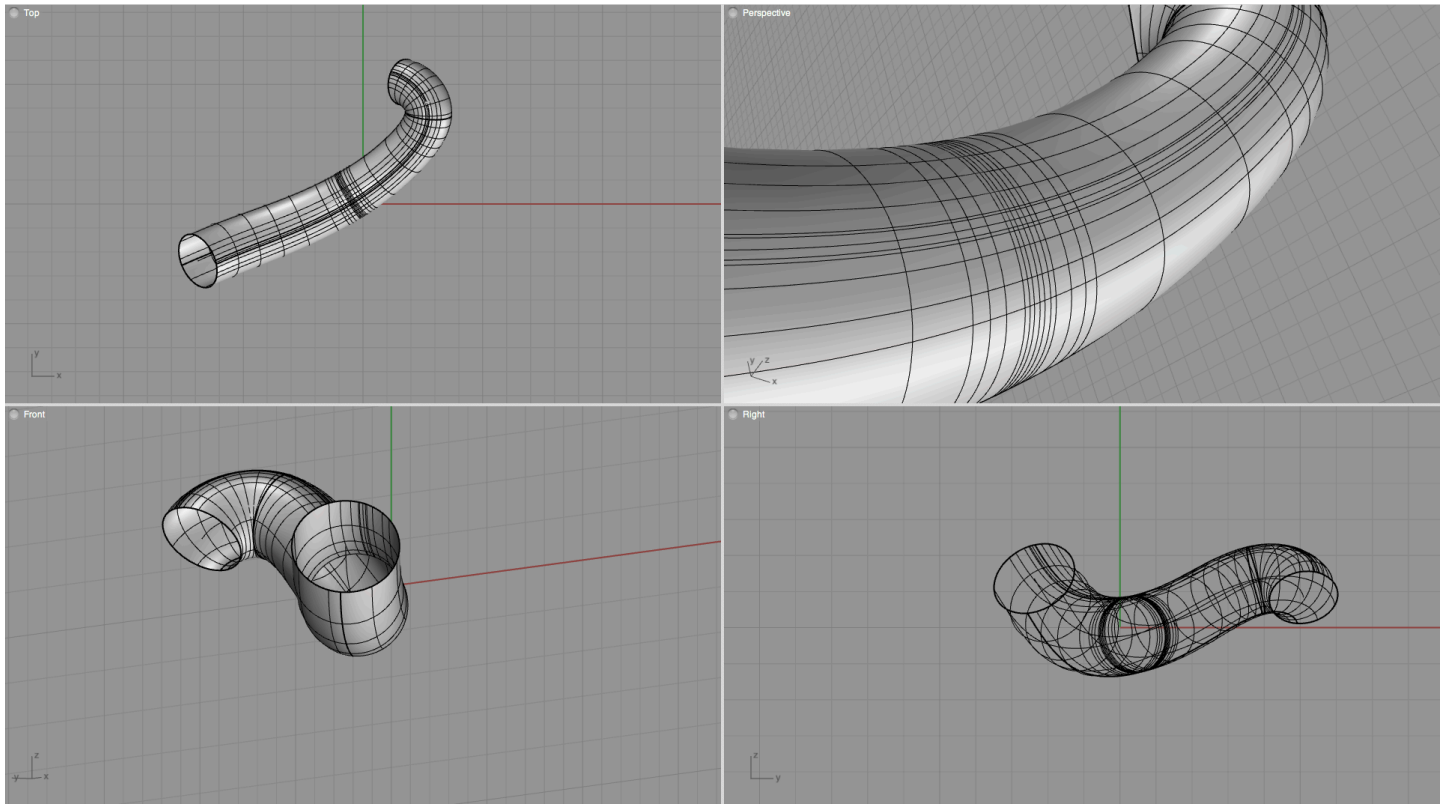

Figure 27: Four views of the healthy geometry. This is a freehand NURBS model using the 3D CAD software package Rhinoceros. The parent artery geometry and aneurysm geometries were identified and made from cranial CT data of the author. Research tools are being developed to fully automate this process.

number of larger elements, with higher degree basis functions. The increased degree increases approximability; the large elements reduces effects due to incompressibility.

- one element in thickness direction (degree 3)
- large, high degree transversal elements (degree 3)
- very high Poisson ratio (.4999)

I used local refinement via hierarchical B-Splines [Evans 2015].

In building my analysis pipeline, I avoid very small aneurysms and very large ones. I concentrate on common, moderately-sized aneurysms, away from bones or branches, within a size range (2–7mm) dominated by physicians' discretion regarding whether to intervene. (See Figure 6.) These aneurysms are easy to identify from a CT scan. A standard technique is to measure the artery diameter's variance from linear. (See Figure 26 on page 98.)

Creating geometries is a crucial aspect of any image-to-computation suite. Professional, nearly fully-automatic methods for locating aneurysms exist (see Figure 26), but few of them allow extraction of the data in a computationally-ready format. Several groups are working toward this end. Fully addressing registration and segmentation is not within the scope of this work, however.

In this work, the aneurysm's location is identified manually, from visual inspection of the CT scan. I then use thresholding to segment the aneurysm and surrounding parent artery.

5.9 Fiber directions

The geometric shape of the artery having been determined, the vector field of fiber directions must be chosen.

Fiber direction is not observable from current CT scanning techniques. I choose a simple direction pattern based on a broad literature of biopsy studies and biomechanics papers. These studies reveal that fiber direction varies in many ways:

1. Fibers lie in a helical pattern, pointing in symmetric directions with respect to the artery axis.
2. It lies in the tangent plane (loosely speaking), which varies with position.
3. It follows motion and deformation of the artery [Baek 2006].
4. It is different depending on which coordinate system is being used.
5. There may be some dispersion of fibers.
6. At a given material point, new fibers are not necessarily placed along the grid lines defined by the time $t = 0$ fiber directions. In fact, through deposition and reuptake, a tissue reorients its fibers to align with directions of stress or strain [Humphrey 2000, Kroon 2007]. In this case, new fibers will make a different angle with respect to the axis than old fibers.
7. It can vary layer by layer, through the thickness of the artery [Kroon 2007].
8. Fibers build a network pattern through cross-linking.

Two additional observations investigated by researchers are

9. Fibers in humans are wavy when relaxed, not straight [Canham 1992, Smith 1981].
10. Fibers in humans are not all aligned perfectly, but have some distribution [Gasser 2012].

I choose two families of fibers pointing at ±45 degrees from the axis of the artery, lying in the tangent plane. Each fiber acts as an independent, one-dimensional structure

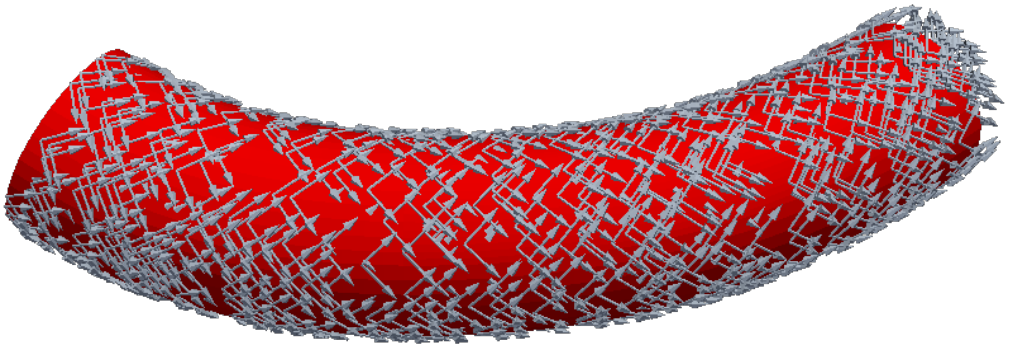

Figure 28: Choice of fiber directions. There are two families, oriented in the tangent plane, ±45 degrees from axial. The pink dot shows the location of the lesion.

which does not change its direction in material coordinates. Fiber directions are exactly defined, with no dispersion or deposition/reuptake. See Figure 28.

The material is a continuum—fibers are not considered as individual proteins, but are instead considered as densely packed within the artery wall. They are modeled as a term within the material's strain energy function 19.

This is a simple and effective choice based on the obervation that my model is not very sensitive to fiber direction. Also, some of the observations above create complications; for example, thickness-dependent orientations could introduce hard-to-interpret internal stresses in the artery.

Chapter 6

Results

I have created the first simulation of saccular aneurysm initiation and development from a healthy artery geometry. Simulation results consistently show an aneurysm with a clearly-defined neck. The simulation begins with a healthy artery; no localized change in thickness is assumed, as in [Eriksson 2009].

The simulated aneurysm demonstrates behaviors similar to clinically-observed aneurysms: the diseased tissue becomes thin and distended from the parent artery, forming a steadily-growing saccular aneurysm. My simulation gives insight into the mechanical environment of aneurysms. I quantified forces and stresses experienced for a realistic aneurysm development. There are complex stress profiles within the neck region that include both extension and compression. See Figure 34.

I began with a CT scan of a healthy subject who was potentially at risk for aneurysm disease. I designed a realistic artery geometry from the CT scan. I selected a location for a lesion likely to grow an aneurysm. I simulated an aneurysm from the lesion's location in multiple ways: first, by prescribing the deformation; second, by specifying an inelastic strain rate. In each case, I quantified forces and stresses associated with the aneurysm.

The profiles of variables in the simulated etiology below provides a method for researchers to understand saccular aneurysms within their own work. I begin such an exploration in § 3.10.1 Alternative growth theories.

I discovered that I can create saccular aneurysm geometries with existing constitutive models. I also found my model of saccular aneurysm behavior is not very sensitive to changes in the strain energy function (Equation (19)) or its material parameters. This is surprising given a rich literature of novel contitutive models and lack of saccular aneurysm results with these models. My model is sensitive to loading conditions, the size and shape of the initial lesion, the rate at which inelastic strain proceeds, and the bending stiffness of the tissue.

My model is consistent with clinical understanding of observed aneurysms. I observe

- significant stiffness difference between healthy and diseased tissue,
- huge strain in the aneurysm dome,
- complex stress patterns within the neck region during aneurysm initiation
  - extension in the direction pointing around the neck's circumference,
  - compression in the direction pointing toward the center of the lesion,
- increased muscular contraction can maintain tone at the base of the aneurysm,
- small focal lesions can lead to large aneurysms.

These results show a successful method for simulating realistic geometries using predictive modeling tools on top of existing constitutive arterial models.

I found that thin-walled arteries formed a saccular aneurysm along a wide range of material parameters. The lesion was defined by local changes to Young's modulus and strain rate; a Winkler term was not used. By contrast, for realistic-thickness arteries only a narrow range of material parameters formed saccular aneurysms. In this case the lesion additionally required a Winkler term.

Thin walls, a Winkler term, and reduced Young's modulus all effect a lower bending stiffness. In my simulations, combinations of these led to saccular aneurysms, suggesting bending stiffness is inversely related to likelihood of saccular aneurysm formation. I suggest that future research and experiments quantify bending stiffness of artery tissue in and around aneurysms.

6.1 Displacement-based calculations

In order to understand the time history of stresses in arteries, I built the capability to perform a displacement-based calculation. This type of simulation allows the calculation of forces and stresses throughout the disease progression. By looking at this data, an understanding of the environment that gives rise to aneurysms can be formed.

I created a realistic saccular aneurysm development from a healthy subject at risk for an aneurysm.

My approach here is to simulate an aneurysm, where I prescribe the deformation and compute the forces and stresses that result. This reveals time histories of parameters which have the capability to produce saccular aneurysms. The model was investigated and improved by changing values of material constants. I specified material parameters as initial values for the forward problem. In this fashion, improvements were made to the model so that the prescribed deformation induces physiologic stresses.

One-dimensional verification tests led to running test simulations of a straight cylindrical artery with an axisymmetric lesion. See Figure 29. The lesion is a band in the middle of the artery. The results led to observations that argued in favor of utilizing a Winkler foundation force within my model.

I used traction-based calculations in order to test the use of this Winkler foundation to model external forces and other phenomena. Simulations have been performed with axisymmetric lesions and with focal lesions.

A series of tests was run to explore a few aspects of the model. In the first test (Figure 29a), a large lesion was postulated and a Winkler term was used. This simulation produced the first successful computation of a saccular aneurysm.

In the second test (Figure 29c), no Winkler term was used. Notice the artery tissue "slides" outward from the neck region. The forces involved are illustrated earlier in Figure 15 on page 46. The ends of the artery are fixed in place (a choice of boundary condition which simplifies the calculation), so the artery buckles.

There is no support at the neck and a saccular aneurysm is *not* formed! Effects like this may hinder Biomechanics simulations from creating a saccular aneurysms. This phenomena illustrates an incomplete understanding of the forces and stresses at the neck region, strength of tissue in the dome, and basal tone.

This is an axisymmetric lesion, and the lessons learned here apply to saccular aneurysms as well.

6.2 Problem setup for realistic artery calculations

I used an artery geometry created from the process in Chapter 5. In that process, I began with the CT scan of a healthy subject, and finished with the smooth geometry pictured in Figure 31 on page 110. I postulated a smooth lesion in the location of the aneurysm.

I used the initial value problem of § 4.1. Boundary conditions are constant internal blood pressure, a small or zero external pressure (modeled after the intracranial pressure

(a) Initial configuration. A thick-walled cylinder with roller boundary conditions and a constant internal pressure. The ends are fixed in the axial direction.

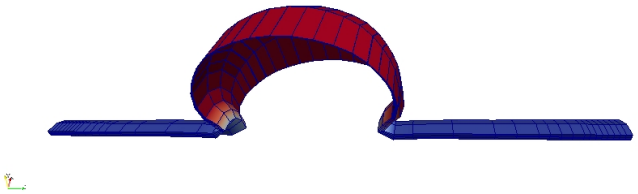

(b) Case 1: Axisymmetric lesion showing a defined neck.

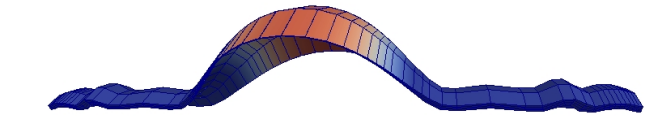

(c) Case 2: The above simulation, but without a Winkler term. The lack of support at the neck causes a *fusiform* aneurysm to form. Supporting forces and/or stresses at the neck should be present, or else tension forces in the dome or parent artery are too high.

(d) Case 3: Smaller, stable lesion with Winkler term. The aneurysm stabilizes due to bending stiffness.

Figure 29: A series of simulations with an axisymmetric lesion, exploring the use of the Winkler foundation term. The lesion is defined as a reduction in the pseudoelastic limit k, and (if used) a reduction in the Winkler coefficient q. Color displays the amount of lesion, from no lesion (blue) to full lesion (red).

and cerebral spinal fluid pressure in the brain), and clamped inlet and outlet (as in Figure 17). I used the adaptive constitutive model from § 3.8, and assumed the geometry was initially stress-free. The stress-free geometry was loaded slowly by the boundary pressures, before the lesion was applied.

6.3 Lesion specification for artery calculations

It is not known where surface area expansion (strain) occurs in saccular aneurysms. It could occur broadly in the dome, focally in a region, or even in the ring-shaped region of the neck. Most research indicates strain occurs focally where jets of blood flow impinge on the aneurysm wall, and broadly within the dome otherwise. This is the assumption I use for specifying lesions. I use a small-sized region for a lesion, because many saccular aneurysms have narrow necks. These aneurysms are assumed to have formed from this small region. (See Figure 31.)

The lesion location was defined as a small spherical region. Spatially, the lesion is defined by two concentric spheres, where material outside them both is completely healthy; material inside both is completely diseased; and material in between decays as a C^1 cubic function of space; see Figure 30a.

The temporal progression of disease is a scalar function. The artery starts completely healthy everywhere. After inflation, the lesion becomes gradually more diseased.

All of the rest of the artery is considered healthy at all times. The spatio-temporal lesion is the product of the two functions; see Figure 30b.

(a) Cubic decay function for defining the spatial location of the lesion. I define the lesion by two concentric spheres: The artery wall within the inner sphere is considered diseased tissue (blue); the artery outside the outer sphere is healthy tissue (red); in between is a piecewise C^1 smooth, cubic function.

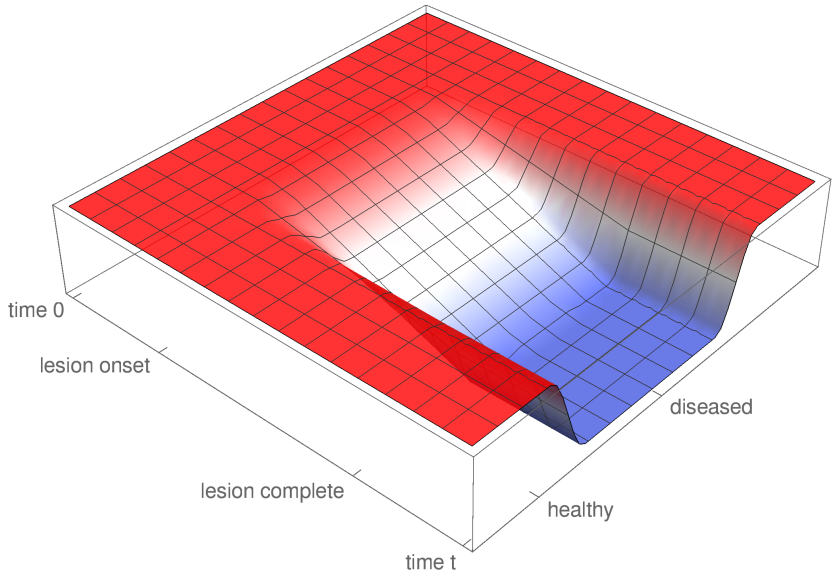

(b) Example of a space-time function for defining a lesion. This example is the product of the spatial function in (a) and a linearly-decaying function in time.

Figure 30: Cartoon describing the definition of a lesion for this work. In this cartoon, the lesion is one-dimensional in space. (In an artery, the lesion is a three-dimensional function of space.) The healthy region is colored red, the diseased region is blue.

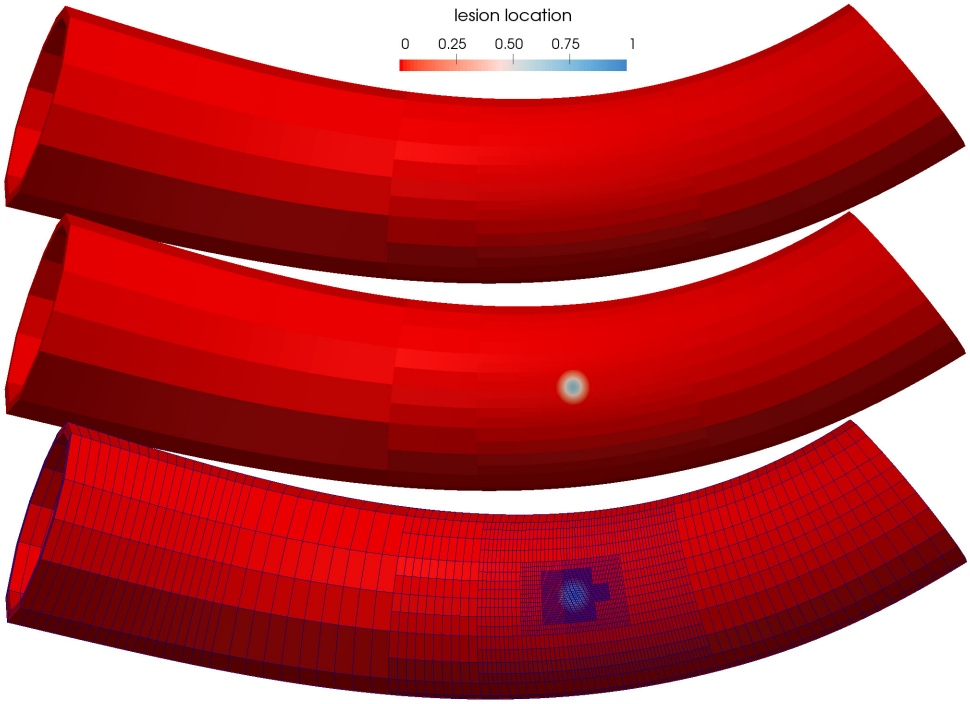

Figure 31: The dot indicates the postulated location of the postulated aneurysm, shown on the healthy artery geometry. The top image shows the artery, the middle shows the lesion, and the bottom image shows the local mesh refinement in the lesion region. (The facets in the image are to highlight local mesh refinement. The geometry is G^2 cubic, circumferentially and axially.)

6.4 Material Parameters

The geometries were built as in §5.7 on page 98. The goal was to apply physiologic forces to the model to grow saccular aneurysm geometries from healthy configurations.

The inlet and outlet of the artery were fixed in space, creating a boundary layer that was far away from the lesion region.

Loading conditions were applied gradually, before the simulation was begun. This consisted of blood pressure at 100 mmHg (internal loading) and cerebral spinal fluid pressure (external loading) at amounts ranging from 0–10 mmHg, depending on the calculation. A full list of material parameters is seen in Table 32.

6.5 Growth-driven calculations

Using the passive growth models of § 3.7 was sufficient for simulating stable focal lesions, but not for saccular aneurysms. An additional assumption was made: that the pseudoelastic yield stress is not chosen *a priori*, but can be dependent upon the fiber stress and growth rate.

In particular, I supposed the irreversible growth rate followed behaviors of observed aneurysms. In an initially healthy thick-walled artery, I followed these stages, seen in Figure 34:

1. The artery was inflated to normal pressures.
2. A lesion was initiated (reduced Young's modulus and Winkler coefficient)..
3. Irreversible growth was initiated ($\dot{\lambda} > 0$, and σ/k increasing).[1]

[1] The scalar $\sigma = \sigma(\boldsymbol{x}, t)$ is the (one-dimensional) Cauchy stress of collagen fibers. The scalar $k = k(\boldsymbol{x}, t)$ is the pseudoelastic limit for those same fibers. Separate values (σ^1, σ^2, k^1, k^2) are used for fiber families 1, 2.

parameter		value	notes
Poisson's ratio	ν	0.4995	Aneurysmal tissue is very thin; $\nu \to 0.5$ helps Newton convergence guesses avoid local $J < 0$.
Young's modulus	E	168 kPa (thin) 31.3 kPa (thick)	[Messas 2013], [Scott 1972] measured "elastance," equal to E times artery thickness.
density	ρ	1 kg/L	Density of water.
collagen stiffening coefficient	c_1	1.658 kPa	[Wulandana 2005]; for my c_1 and c_2, see equation (21).
collagen stiffening coefficient	c_2	12.7	[Wulandana 2005], modified since I do not use pre-stress.
fiber relaxation timescale	τ_{relax}	70 days	[Humphrey(1) 2002].
timestep	Δt	0.2–1 days	Chosen so that $\frac{\Delta t}{\tau_{\text{relax}}} \ll 1$.
mesh Bezier degree		3 (cubic)	Cubic in all directions (axial, circumferential, and radial).
artery diameter		2.30–1.85 mm	Gradual taper, proximal to distal.
artery thickness		0.15 mm	[Humphrey(2) 2002], intima–media thickness of posterior communicating artery.
artery length		7.5 mm	
lesion size		0.30 mm	Sphere outer radius.
lesion size		0–0.27mm	Sphere inner radius.
Winkler stiffness	q	666.7 kg/s^2	Healthy tissue, thick-walled arteries.
strain hardening rate	H_{irr}	0 kPa	Exploration of strain hardening $H_{\text{irr}} > 0$ and strain softening $H_{\text{irr}} < 0$ is a subject of current research.
lesion softening rate	H_{les}	-100	Arbitrary large number.
blood pressure	p_{BP}	100 mmHg	Classic average for a healthy human.
intracranial pressure	p_{brain}	-15 to 15 mmHg	[Albeck 1991]: 7–15 mmHg (laying down). [Chapman 1990]: -15 to -10 mmHg (standing).

Table 32: Values of material parameters, constant for all simulations. More discussion is given in the text.

material	spring constant	notes
radial artery dilation during the cardiac cycle	600–900 g/s^2	[Wei 2012]
toy Slinky	840 g/s^2	helical spring steel
Winkler term	0–66.67 kg/s^2	thick, healthy tissue
car shock	$\sim$5000 kg/s^2	

Table 33: Spring constants for various materials. These can be used to understand the size of the Winkler term. I use a large Winkler stiffness for artery tissue with a thicker muscular layer, and near zero Winkler stiffness for artery tissue with little or no muscular layer. Little medical data is available, because *in vivo* material stiffness is difficult to measure.

4. Irreversible growth was slowed and stopped (σ/k decreasing).

5. Irreversible growth was re-initiated.

They mimic clinical observations for saccular aneurysms. In clinical terminology, I can describe the steps as

1. A normal, healthy artery.

2. Disease processes are initiated by cellular changes in the artery wall.

3. A visible aneurysm begins to develop.

4. The aneurysm becomes stable. Most aneurysm diagnosis occurs at this stage.

5. The aneurysm becomes unstable. Around 10% of diagnosed saccular aneurysms go unstable.

The final geometry for the thick-walled artery can bee seen in Figure 36. A cross section shows the artery becomes thin in the aneurysmal region (Figure 37). The healthy artery is 0.15 mm thick (normal for the posterior communicating artery), and the aneurysmal region is roughly 0.01 mm think. The neck is about one-third of a millimeter in

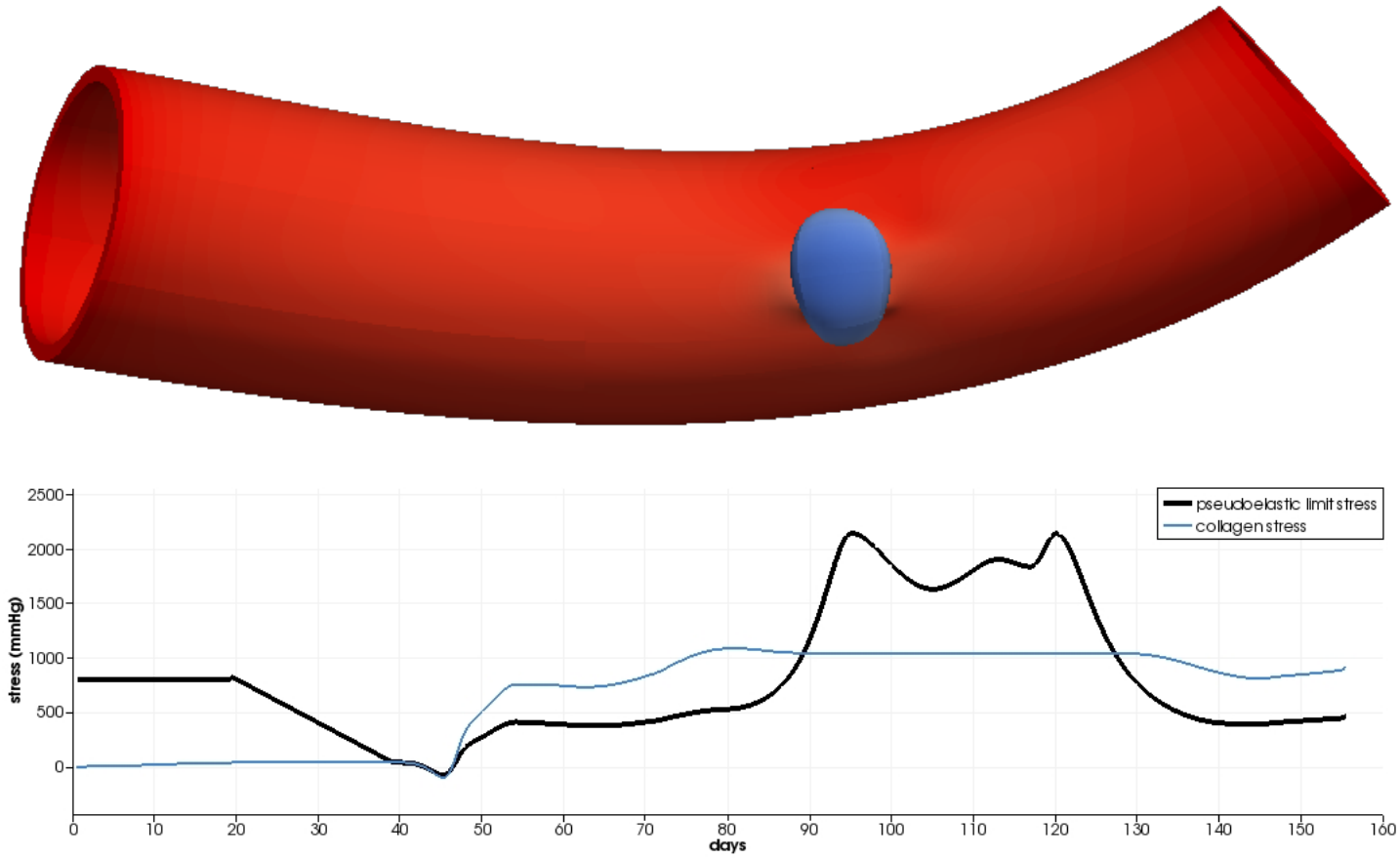

Figure 34: Simulated saccular aneurysm grown from a healthy, realistic geometry. Shown are the collagen fiber stress and pseudoelastic limit stress over time, for a point in the center of the dome of the artery (pink dot). The pseudoelastic limit is not determined *a priori*, but is a function of fiber stress. Interestingly, for my growing saccular aneurysm, the limit decreases initially but then rises significantly afterward, to chase the rising Cauchy stress. This implies a complex degradation/healing profile; the material is at first strain softening, then hardening in a continuous curve. Facets visible in the artery are a visualization artifact; the artery is smooth (C^2 cubic shape functions). More graphs are shown in Figure 35.

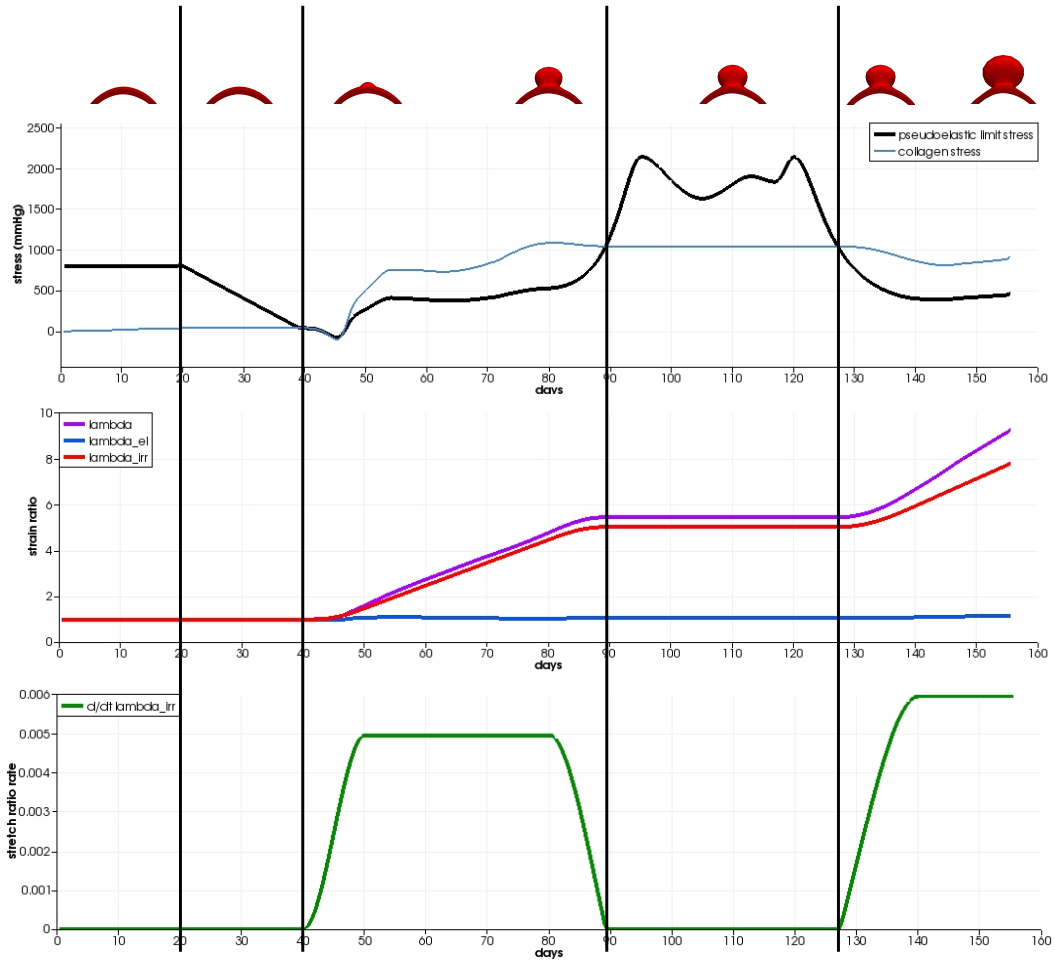

Figure 35: Simulation results for the thick-walled artery, showing relationships between k, σ, λ_{irr}, and $\dot{\lambda}_{\text{irr}}$. (a) The top graph shows pseudoelastic limit k (black) and Cauchy stress σ (blue) of collagen fibers. (b) The middle graph shows the stretch ratios. The purple curve λ is the product of the blue curve λ_{el} and the red curve λ_{irr}. The elastic stretch λ_{el} is nearly 1 throughout and plays a negligible role in aneurysm development; this is consistent with biological understanding of aneurysms. (c) The bottom graph shows the time rate of change of λ_{irr}. This determines when the aneurysm grows. The simulated aneurysm is shown cross-sectionally, with the proximal and distal artery cropped from view. (The artery's axis points into the page.) Notice from the images that the aneurysm grows during those times when $\dot{\lambda}_{\text{irr}} > 0$ (early and late aneurysm images are shown), and not when $\dot{\lambda}_{\text{irr}} = 0$ (one image shown) which is true when the Cauchy stress is lower than the limit stress.

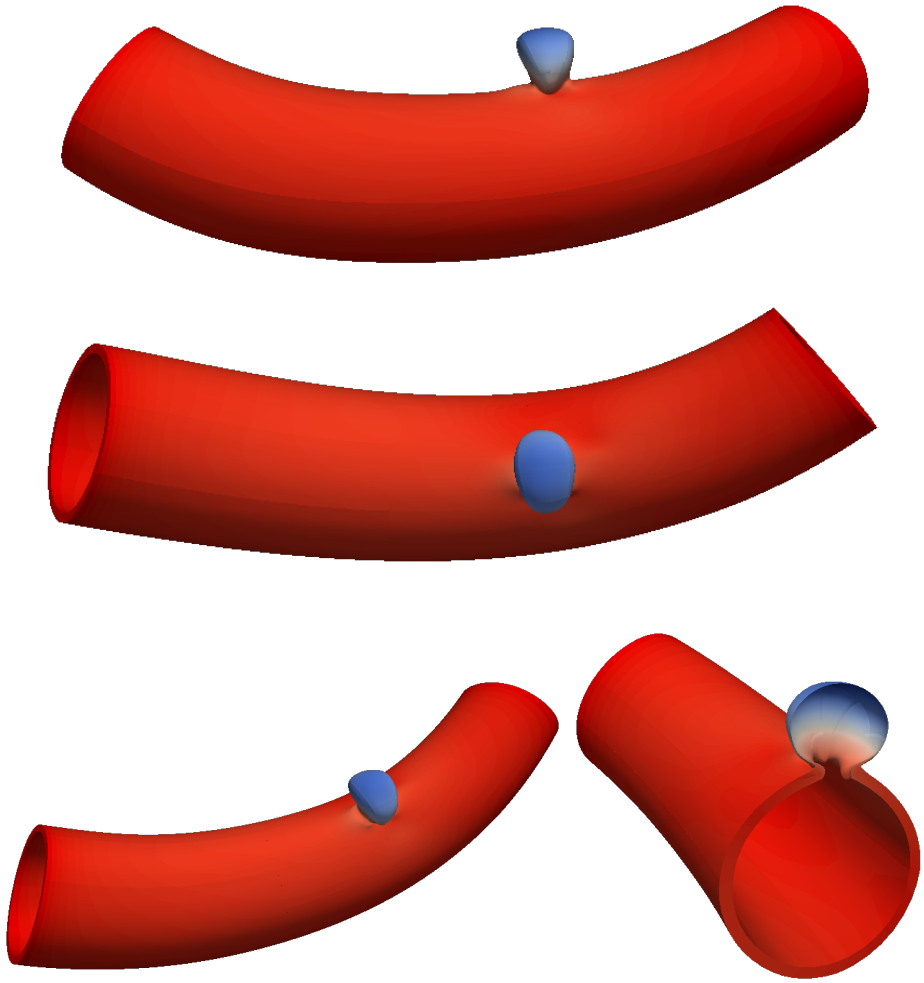

Figure 36: Final saccular aneurysm geometry from a few camera angles. The artery is colored by surface area strain, in the plane perpendicular to the thickness direction. The strains are large, ranging from 0.5 (compression) to around 93. The fourth image shows an axial cut through the aneurysm.

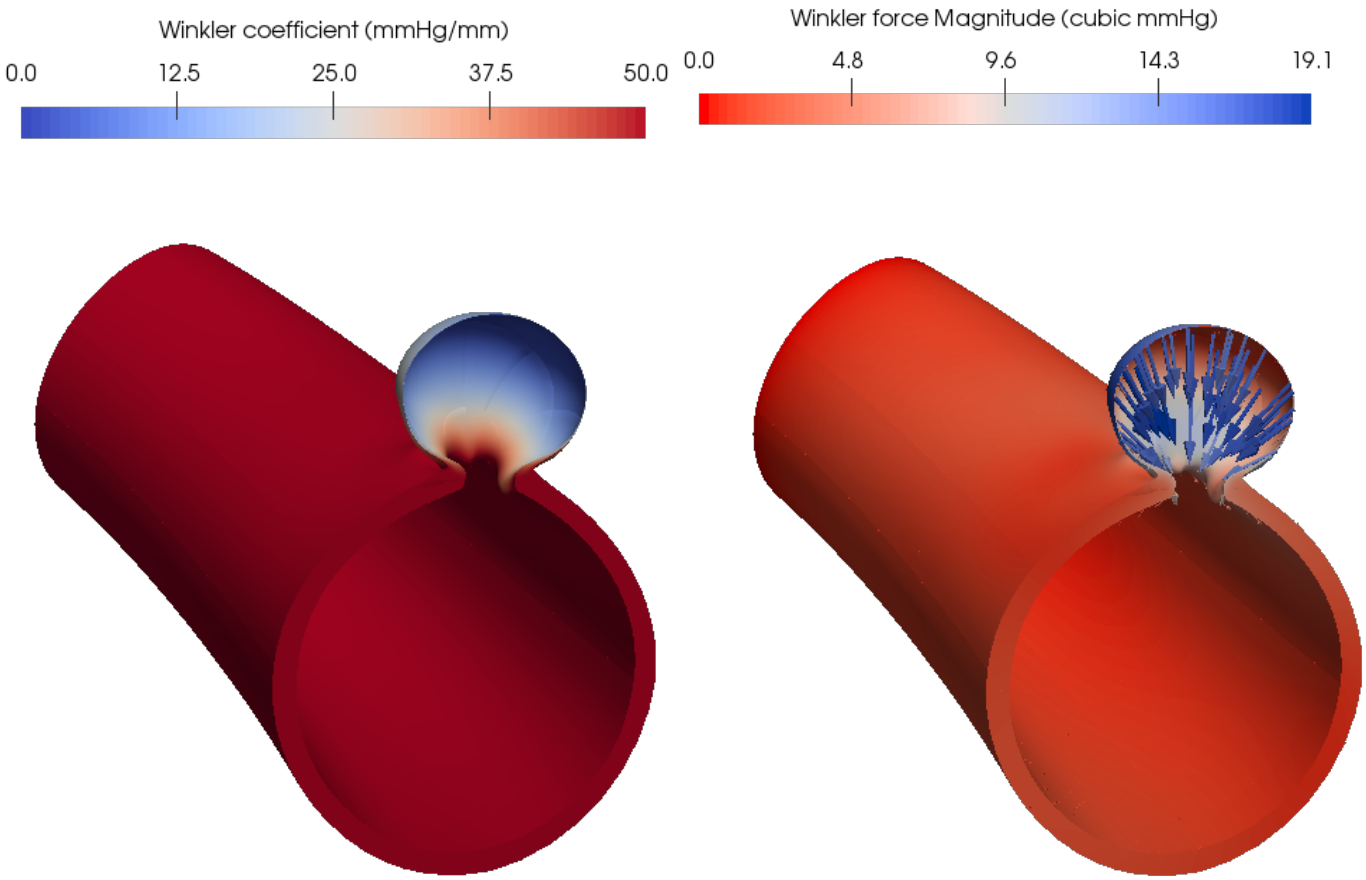

Figure 37: Axial cut of the saccular aneurysm, for the thick-walled artery. Red shows the healthy artery value, and blue is the most diseased value. 1 mm^3Hg = 1/7500.6 N = 13.32 dynes. On the left is the Winkler coefficient used (which also defines the lesion), and on the right is the resulting Winkler force. The Winkler force is small, even at its maximum of 19 mm^3Hg = 253 dynes.

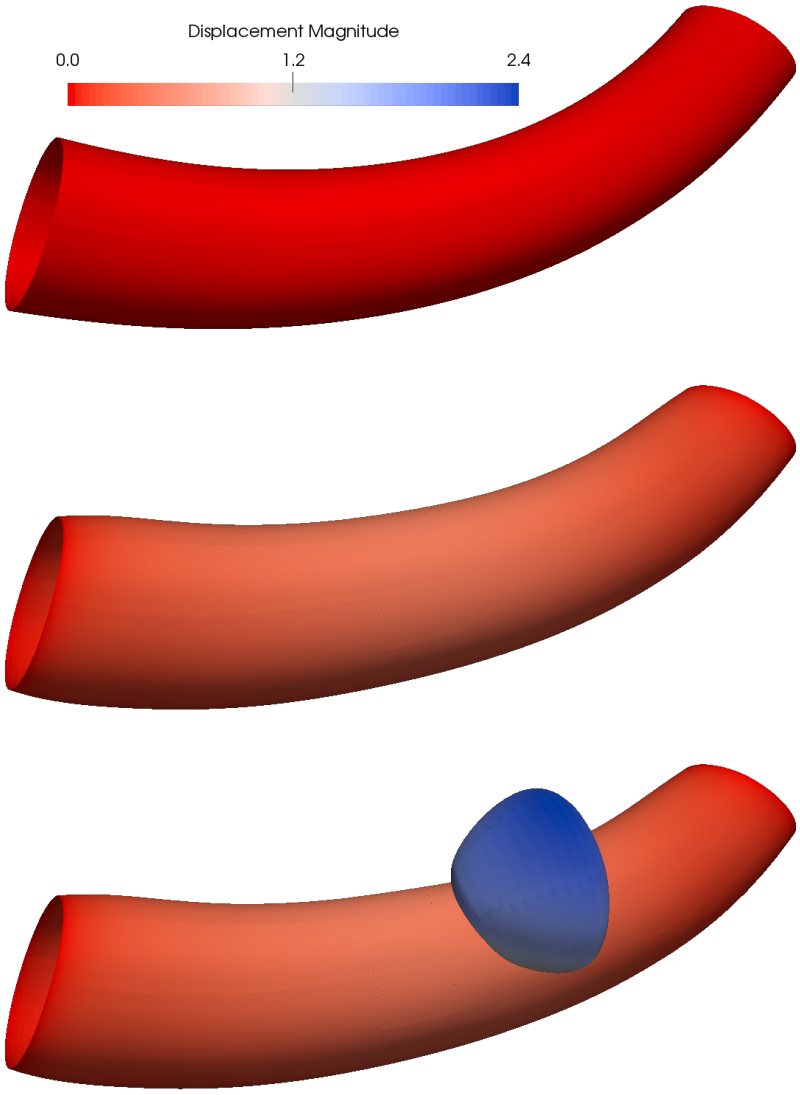

Figure 38: Simulation for a thin-walled artery. Compared to the thick-walled simulation, Young's modulus was increased (see Table 32), and there was no Winkler term. The resulting aneurysm was larger.

diameter. The dome is roughly 1.14 mm wide (perpendicular to the artery axis), 0.84 mm long (along the artery axis), and 0.90 mm in total height. The healthy Winkler coefficient is 66.67 kg/s^2, or 50 mm^{3}Hg/mm. In the diseased region, it is reduced to a minimum of 0.3 mm^{3}Hg/mm.[2] The force exerted by the Winkler term is small: less than 20 mm^{3}Hg (equal to 0.0267 N).

I also performed a simulation with a thin-walled artery, to demonstrate the model without a Winkler term. See Figure 38. In this case, Young's modulus was higher to account for the artery's thinness; otherwise, material parameters and time-varying inputs were kept the same.

6.6 Discussion

I developed a simulation tool for saccular aneurysms from common constitutive models by adding two major features. First, I use local changes in material parameters to represent weakening of the artery wall. Second, I use a growth model of adaptive irreversible strain to represent adverse collagen remodeling. Due to internal blood pressure, these cause expansion and buckling of the arterial wall. The model is highly sensitive to changes in material parameters related to these features.

My choices for parameters to define the lesion were motivated by kinematic arguments. A saccular aneurysm deformation could not be achieved without localized changes to some properties. For my simulations, I chose to reduce bending stiffness, to increase lengths of collagen fibers, and add a Winkler foundation force in thick-walled arteries.

[2] The unit mm^{3}Hg is the force exerted by gravity of one cubic millimeter of mercury, equal to 1/7500.6 Newtons. For example, a blood pressure of 120 mmHg on a 1 mm x 1 mm patch of artery exerts a force of 120 mm^{3}Hg. The unit mm^{3}Hg/mm is a spring constant unit for a spring requiring one mm^{3}Hg of force per millimeter of displacement.

These local changes correspond to biological processes which are not fully understood. Insight into biology can be gained by building biological models that conform to the kinematic requirements revealed by my work.

My observations suggest bending stiffness is a dominant factor in determining whether a simulation forms a saccular aneurysm. Wall thickness, Young's modulus, and Winkler force all affect bending stiffness, and some combination of these was necessary in all saccular aneurysm simulations I performed. Adaptive irreversible strain relies on buckling of the artery wall, which is also dominated by bending stiffness.

On the biological side, bending stiffness is controlled by vascular tone, inflammation, and elastin degradation, among other factors. Tissue surface area enlargement is controlled by changes in the collagen fiber network. Experiments can be devised to measure these material responses and re-inform my kinematic simulations.

Particularly, better understanding of the strain rate for collagen growth $\dot{\lambda}_{\text{irr}}$ and elastin degradation $\dot{k}_{\text{les}}$ can improve simulation results. These two variables in the model line up neatly with stages of observed aneurysm development. My simulations have highlighted them as a path for biological and kinematic cross-communication.

The dome of the simulated aneurysm has a surface area of about four square millimeters, from a lesion approximately one-third of a square millimeter. This is an increase of area of factor of around 12. The thickness starts at 0.15mm and is simulated to thin out to about 0.01mm. These are big changes for a tissue, and raise the question of what is happening to the material physically to allow such a change.

My model considers the material as a continuum, and does not track individual mechanisms of fiber strain. Those mechanisms could be: straightening of relaxed, wavy

fibers; overstrain and breaking of fibers; remodeling of fibers; etc. None of these mechanisms can be observed *in vivo*. Thus I cannot speculate on the physical changes a growing aneurysm experiences, whether from experiment, observation, or simulation. I can say my simulation shows enlargement profiles consistent with observations.

6.7 Suggested experiments

The profile of k_{les} is a phenomenological model, capturing mechanical effects of the phenomenon of degradation and aging. The analysis in Section §3.8 describes how to compute a profile of k_{les} which, as I saw in this chapter, gives rise to a realistic saccular aneurysm. Thus k_{les} has the capability to produce at least one class of saccular aneurysm shapes. It may be the case that different k_{les} profiles correspond to different lifestyle choices. Future work will help ascertain the manner and extent of its capabilities.

Several interesting questions regarding k_{les} immediately arise.

Question: Is k_{les} rich enough to describe large classes of observed/observable data?

Question: If material properties are kept constant, could k_{les} alone be enough to describe the range of observable behavior?

Question: Is k_{les} completely hidden from scrutiny, or is it measurable?

Question: How does changing features or properties of k_{les} (such as time or space derivatives) give rise to different classes of aneurysms? Put another way, can different classes of aneurysms be usefully classified in terms of properties of k_{les}?

Experiment: Could an experiment be run where material properties are kept the same, but disease initiation (representing k_{les}) is changed? Possible variables: age, sex, health history (e.g., diabetes), lifestyle, smoking history, family history, artery tortuosity.

Goal: Expand understanding of k_{les} effects and its ability to grow a wide range of aneurysm geometries.

6.8 Future work

This work demonstrates a process for simulating initiation and evolution of saccular aneurysms. Future projects could involve simulating different lesion shapes: circular (used throughout Chapter 6) of various sizes, ring-shaped, a misshapen blob, circle-to-ring (where growth occurrs in the neck region), circle-to-dome (where growth occurs only in the dome), crescent; and differences through thickness (only outer layers, or only inner layers, or more on inside or outside).

A membrane model could be devised from the current model. A membrane model of fibers would display resistance to shear; my model displays resistance to shear via the "background material."

More attention can be paid to muscular and elastin degradation. Particularly, research should investigate space-time profiles of degradation of muscle and elastin within cranial arteries with age, including development of localized regions of degradation. The localized degradation of artery walls is the main postulated initiator of disease in arterial mechanics, but little published research attempts to give primary elastin degradation profiles. Most research postulates elastin degradation is secondary to another factor such as wall shear stress, tortuosity, or a head injury.

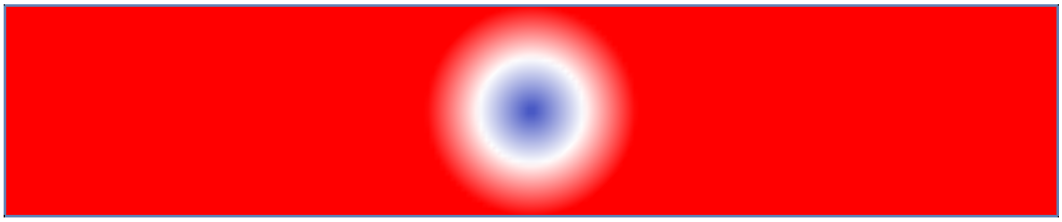

(a) Cartoon of a theoretical isolated lesion. Red is healthy; blue is diseased. Clear, simplified lesion functions like this are interesting for basic research, but they miss nuances of irregular aging.

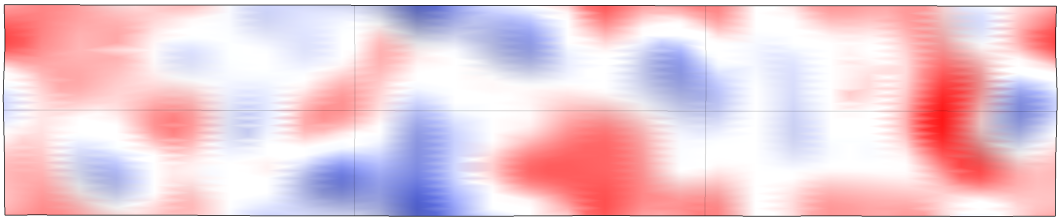

(b) Cartoon of a postulated realistic profile of elastin degradation in arteries. Color depicts health of elastin. Like with skin, elastin in arteries degrades irregularly, with natural variations. It is likely that these natural variations ultimately determine aneurysm locations.

Figure 39: Examples of elastin degradation and/or lesion profiles. Attention paid to experimental measurements of these profiles will provide benefits to simulation and prediction.

Some researchers and clinicians suggest without proof that some people are born with a propensity for localized degradation of arterial tissue.[3] Autopsy studies should quickly reveal whether this is the case.

There is no reason to believe degradation is constant in space, and natural variation will certainly play a role in localized weakness and increased susceptibility to aneurysm formation. Aneurysms are often thought of as single spots of diseased tissue within an otherwise perfectly healthy artery, as in Figure 39a. Rather, they are more like Figure 39b.

To build better models of artery aging, one can study other similar tissues: skin and arteries are layered tissues with collagen and elastin fibers—and skin is more observable. Elastin degradation in aging skin shows similar patterns to elastin degradation in artery

[3] Aneurysms have been observed in uninjured adolescents and toddlers.

walls. Degradation occurs, but not at constant rates. This is noticeable when focal skin lesions occur (e.g., liver spots, freckles, cherry angioma, melanoma) There is variance in the nature and extent of degradation; this variance can be measured experimentally, and statistical distributions in both time and space can be built that faithfully model natural aging processes. These space–time model of skin could be used to determine space–time profiles for k_{les}.

Patients with one cranial aneurysm are at high risk of having multiple aneurysms [Mizoi 1989]. This suggests degradation is global; that is, degradation in one region implies degradation in other regions. Assessing the manner and extent of degradation will improve prediction of aneurysm disease. For instance, an important question to answer is, does the variance and magnitude of degradation produced by the model comport with the frequency and magnitude of formed aneurysms?

Experiment: For one or more subjects in the International Study of Unruptured Intracranial Aneurysms [ISUIA 2003], perform an autopsy, including careful examination of cerebral arteries. An analysis and quantification of artery tissue makeup (layers, elastin degradation, muscular layer, collagen makeup, etc.) especially near aneurysms and in apparently healthy tissue. Much can be learned from patients who do not die of aneurysm-related illnesses.

Chapter 7

Stages of aneurysm development

When connecting two disparate fields, we often want to answer questions posed in one field with techniques built in the other. For example, questions in history such as "Did these two cultures engage in trade?" can be satisfactorily answered by studies in anthropology: "Do we find artifacts from both cultures in the same place?" Or perhaps photography can help explain life's struggles: a well-encapsulated image often elucidates and refines how people think. In this work, I utilize techniques of kinematics to describe soft tissues, and to understand initial stages of disease.

A person connecting fields should consider how to clarify the initial question to a specific issue. It should also create an analogy between the fields that allows them to state the clarified issue in terms of the second field. Techniques in the second field can be applied in order to explain or solve the issue. The explanation should be able to be transferred back into terms of the first field via the analogy linking the two fields.

For myself, I wanted to address intracranial aneurysms. Three major questions arise when presented with a patient who has aneurysms: How did this aneurysm develop? How will it progress in the future? And how can we prevent others from getting aneurysms?

I have tried to answer the first question.

In so doing, I have clarified the question into specific issues, and created analogies for translating understanding from medicine to engineering and back. I created a pipeline

for building patient-specific geometric models of arteries from medical image data. I have a tool for visualizing the simulated aneurysm to supplement physician understanding.

7.1 The Stages

My model is primarily driven by the relationship between two particular variables, pseudoelastic limit k and fiber stress σ. These quantities have important physical interpretations. At each point in the artery wall, the fiber stress is the current stress felt by the tissue. It represents the mechanical loading required of artery walls. The pseudoelastic limit is the maximum stress the artery can experience without irreversible damage. It represents a kind of maximum load limit for the artery.

This model of describing arteries is simple and has far-reaching implications. Properties of the difference of σ and k create natural descriptors for stages of aneurysm disease. See Figure 41.

The progression in time of σ and k will vary, and they may cross each other. For a healthy artery, k is bigger than σ. This is the situation for people who do not suffer from an aneurysm. (Stage 0.)

In some people, k falls. It falls so far that it drops below σ. At this moment, an aneurysm starts to form. (Stage 1 begins.)

The model has now created a rare and beautiful thing: a mathematical description of a clinical finding. When k stays greater than σ, the artery appears healthy. When $\sigma > k$, an aneurysm forms. (Stage 2.) In this case there is a visible aneurysm. For as long as $\sigma > k$, the aneurysm will continue to enlarge.

In most people with diagnosed aneurysms, the aneurysm is stable. Thus k must have risen back above σ. (Stage 2.) There must be some healing mechanism. My model dictates that k must be increasing for this to occur.

An immediate healing mechanism following a decay mechanism is consistent with biological understanding. Biological mechanisms have competing pathways which balance. Immediately after an artery is injured, both clotting factors and anti-clotting factors respond. A similar phenomenon occurs with cell depolarization: sodium channels open to allow positive charge to rush into the cell, and potassium channels open to allow positive charge to rush out. In hormone replacement therapy, progestin is given to balance estrogen. Pain stimulates analgesic responses.

In my model, I represent the dominance of healing by increasing k. When k increases to become larger than σ, the aneurysm becomes stable. (Stage 3.)

Most aneurysms are diagnosed at this stage: they grew, but became stable.

An important question to be answered is whether the aneurysm will enlarge or remain stable. Roughly ten percent do not remain stable. For these aneurysms, under my model, k decays again below σ; in some cases, σ grows. I would like to be able to predict which ninety percent will remain stable. These patients do not need annual followup scans, which are both expensive and scary.

In the event of further enlargement, k will be less than σ again (back to Stage 2). The aneurysm may enlarge slowly or quickly (Stage 2), may cause symptoms (Stage 4), or may hemorrhage (Stage 5). A person experiencing symptoms often feels dizziness or sudden, debilitating pain. Emergency surgery may be required.

Stage	mathematical description of $k - \sigma$	clinical description
Stage 0	positive	healthy artery
Stage 1	positive, decreasing	preclinical lesion
Stage 2	negative	growing (preclinical) aneurysm
Stage 3	was negative, now positive	stable aneurysm
Stage 4	negative	symptomatic aneurysm
Stage 5	negative	hemorrhagic aneurysm

Table 40: Descriptions of stages. See also Figure 41.

Refined notions of health and disease emerge from the Stages. I can identify decay of the artery as any time k is decreasing, or equivalently, when the derivative of k is negative. Similarly, healing dominates when k increases. It may be appropriate to say healing processes also occur, but are not dominant, when k is concave upward. Under this model, an aneurysm is enlarging if and only if $k < \sigma$. An aneurysm is stable if and only if $k \geqslant \sigma$. I can answer many such questions from the connections between mathematics and medicine. (See Figure 43 and Table 40.)

The aneurysm development I have just described is encapsulated in Figure 41. It follows typical clinical presentation of aneurysms. Looking back over the aneurysm development, I have built a direct analogy beween clinical findings and mathematical statements. The analogy is compelling enough that I can suggest the search for a new clinical finding: a "subclinical lesion". Structural weakening within the artery wall probably begins before deformation. The point at which this occurs significantly I can define as a subclinical lesion. The artery appears healthy, but disease has already begun. Mathematically, I describe this as the point at which the pseudoelastic limit begins to fall markedly.

In this case, the derivative of k is negative. It is at this stage that I hope to build preventive treatment strategies to save lives, economic burden, and reduce disease. (See Figure 2.)

This concept is a valuable outcome of the biomechanical formulation built for the current work. It recognizes two sensitive parameters in the model—pseudoelastic limit and Cauchy stress—which dictate the progression of disease.

The results of my saccular aneurysm growth follows the same pattern, which can been seen by drawing the Stages of Figure 41 upon the presentation of Figure 35. These are combined in Figure 42.

7.2 Mathematical connection to clinical presentation

There are many interesting crossover concepts embedded within the graphic in Figure 41.

For instance, a physician will ask, "Is this aneurysm stable?" The row of boxes in the graphic show stability occurs in two regions: in Stages 0 and 1, and in Stage 3. These stages are described mathematically as any time $k < \sigma$.

Similarly, the situation where $k \geqslant \sigma$ implies an aneurysm is unstable—Stages 2, 4, and 5. Other corresponding physician/mathematician questions are shown in Figure 43.

It leads to a necessary and sufficient condition:

> Under this model,
> an aneurysm is stable
> if, and only if,
> the pseudoelastic limit is larger than the Cauchy stress.

Also:

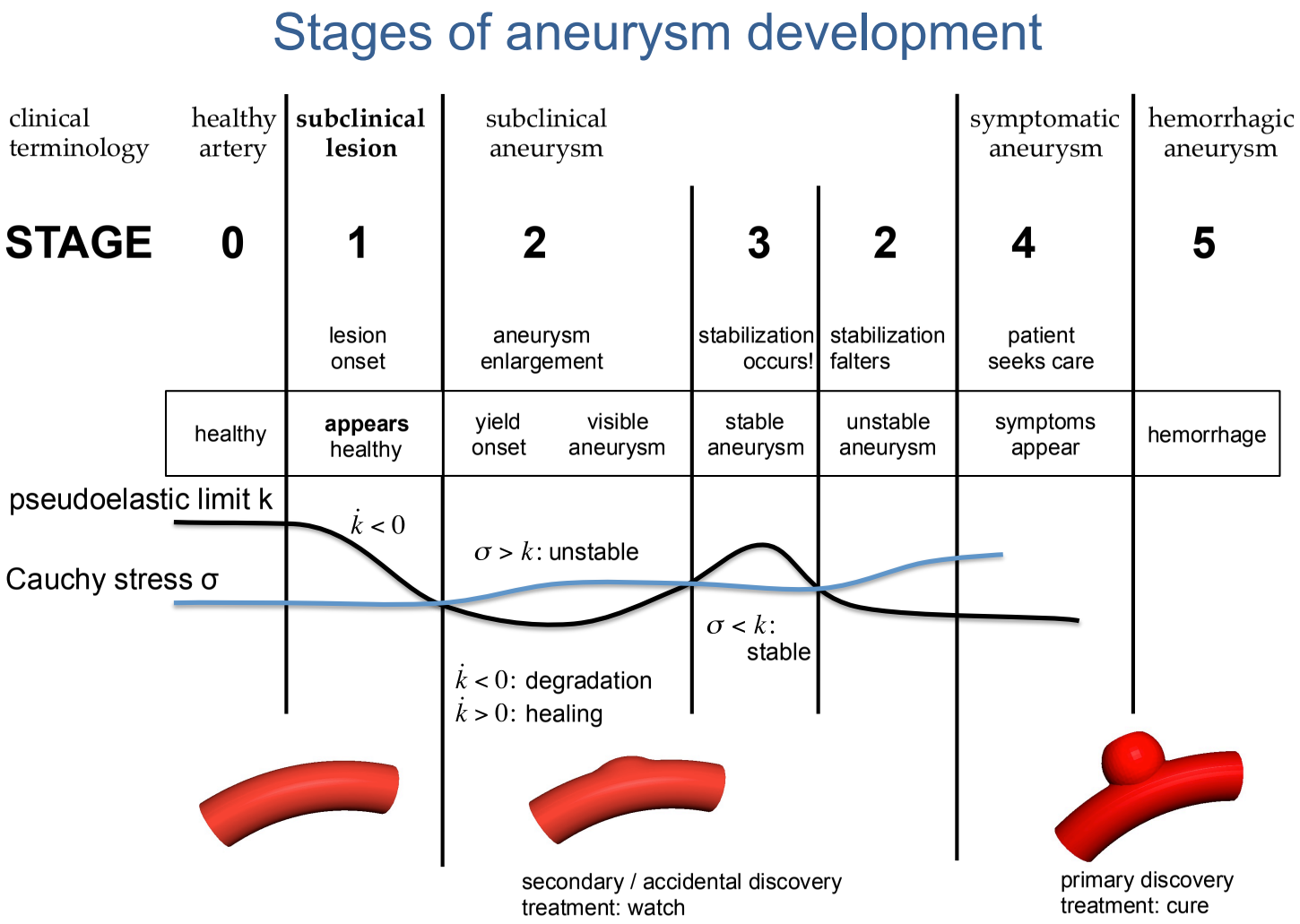

Figure 41: Stages of aneurysm development. Mathematical features of the difference between the pseudoelastic limit and Cauchy stress—slope, concavity, and sign—indicate clinical presentations in the aneurysm produced. Particulary novel is Stage 1, the recognition of a "subclinical lesion" indicating early, unmeasurable presentations of the disease. Understanding this stage is crucial for prevention.

Simulated Aneurysm

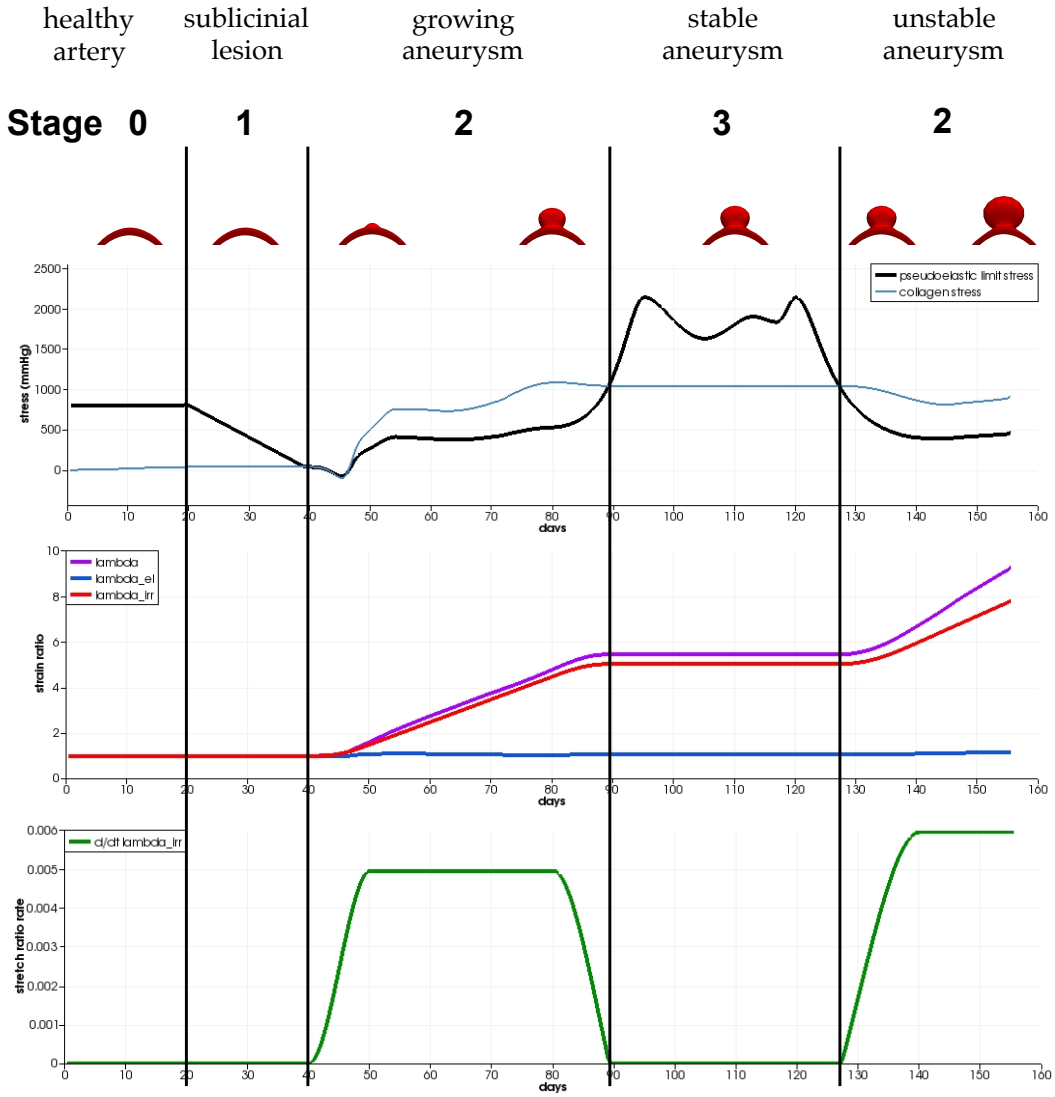

Figure 42: Simulation data with Stages of aneurysm development. As predicted by the model, the simulation results directly show a connection between mathematics driving the simulation and clinical terminology. This figure is a combination of Figures 35 and 41. It shows that I have developed a simulation tool which can predict realistic saccular aneurysm development from patient-specific data—the first-ever model to do so.

Physician's question	Mathematical question	Relevant observation
"Is this aneurysm **stable**?"	"Is $k \geqslant \sigma$?"	"Yes, in Stages 0, 1, and 3."
"Is this aneurysm **unstable**?"	"Is $k < \sigma$?"	"Yes, in Stages 2, 4, and 5."
"Is the artery **healing**?"	"Is k increasing?"	"Healing could also occur when k is concave up."
"Is the artery **degenerating**?"	"Is k decreasing?"	"Degeneration could also occur when k concave down."
"Is the artery **healthy**?"	"Is $k > \sigma$ always?"	"Probably, if σ is within normal limits."
"Is the artery **diseased**?"	"Was $k < \sigma$ ever?"	"Probably, if σ is outside normal limits (either high or low)."
"Should I intervene?"	**"A risk analysis tool is needed."**	"The totality of symptoms should be considered."

Table 43: Physicians and engineers can engage in a common dialogue through the story inherent in the stages of aneurysm disease. Mathematical features of the present model suggest descriptions with clinical relevance. Exploring the validity of these suggestions requires a conversation between engineers and physicians. Connecting disparate but relatable fields is the primary goal of all interdisciplinary research.

An aneurysm is present
if, and only if,
the Cauchy stress ever exceeded the pseudoelastic limit.

Similar questions arise when asking, "What is a precursor to aneurysm disease?" The answer, in this model, is "When the pseudoelastic limit first begins to fall." Many popular biomechanical models instead suggest that if there is no deformation, there is no disease is present; that an artery's disease state can be determined completely from the deformation. I have found a valuable connection to create a model which can model cellular changes within an aneurysm wall. As the graphic indicates, I see a recognizable Stage of subclinical lesion development which is a precursor to disease.

A subclinical lesion
in an apparently healthy artery
is a precursor to aneurysm disease.

In Medicine, it is accepted that there may be precursors to disease, but there is no safe method to detect or measure them. The Stages graphic gives one: it suggests a direction for studying this precursor of disease. It suggests measurement of the pseudoelastic limit and changes therein are methods for *early detection and prevention of aneurysms.*

The model provides summary concepts—pseudoelastic limit, fiber strength, subclinical lesion—which biomechanical engineers and physicians can use to engage in an ongoing dialog of alternatives. If the model is correct, it provides necessary and sufficient conditions that bridge fields.

The stages of aneurysm development shown in Figure 41 have shown promise. They give a mathematical definition of clinical findings. They encourage conversations between medical professionals and engineers researching tissue mechanics.

The next step is to continue those conversations. In this work, the stages will be presented to clinicians and researchers. The concepts can be improved to encourage buy-in from both fields. Buy-in from disparate parties is best achieved by engaging them in the development process. Many avenues for connecting to physicians are discussed in Chapter 8.

Chapter 8

Cardiovascular Engineering at UT

Engagement of the medical community in cardiovascular engineering is well underway. Ongoing long-term collaboration and access at institutions in Austin and Texas have been developed. Hospitals, device companies, clinical practices, and the state government have all been instrumental.

One of the most importnt aspects of connecting two major fields is arranging for experts in each field to spend time in the environment of the other. For instance, Engineering faculty and students need to learn some medicine, and experience medicine as it is practiced by physicians. Physicians, for their part, need to take time from their practice to learn how they approach problems.

Here at UT, I have done this in several ways: by offering Engineering graduate courses in medicine, taught by physicians; by giving students access to hospital laboratories and operating rooms; by joint Engineering–Medicine seminar series; and by offering office space and resources to practicing physicians in Engineering buildings.

Crossover of engineers into hospitals needs to be a daily occurrence. At present, it is a singular experience.

8.1 Cardiology courses at UT

Graduate-level courses dedicated to understanding and/or modeling of the cardiovascular system are rare at UT.

8.1.1 *Clinical Cardiology*

One of my first methods for engaging local physicians in engineering consultation came from the creation of a seminar course in Mechanical Engineering, *Clinical Cardiology*, taught by H Kent Beasley MD and myself. The course is now in its tenth year. It is wildly popular. It features seminars from Kent Beasley, Noninvasive Cardiologist at Capital Medical Clinic for over 45 years (now retired), and nationally-renowned cardiologists from most cardiac specialties: catheterization, electrophysiology, heart failure, robotic surgery, stem cell therapy, vascular surgery, valve replacement, etc.

Presentations are designed to teach someone untrained in medicine about care and treatment of cardiac patients. They are designed to engage the audience and stimulate new ideas for how their interests can help improve treatment of heart disease.

Additionally, they allow physicians the chance to meet and collaborate with young researchers on projects within the hospital. One of my students worked with a heart failure specialist on evaluating so-called "left ventricular assist devices" (LVAD). LVADs are mechanical devices that aid a failing heart in pumping blood to the brain and body. The are used in patients with heart failure, who might otherwise be candidates for a heart transplant. Thus they are so-called "bridge-to-transplant" therapies.

LVADs are implanted in people both old and young. Many people over the age of 60 suffer from chronic heart failure and eventually need more help than medical therapy can provide. Even some young people develop heart failure, frequently from a bacterial infection destroying their valves.

Over a few decades of research, trials, and improvements, LVADs have become effective therapies, giving patients a good quality of life. In fact, because LVADs are so

effective, and because there are so few hearts available for transplant, many patients choose to keep the LVAD as a permanent solution.

Heart transplants are serious endeavors: the initial surgery has risks, and a long recovery period; 1-year survival rate is only about 88%; 5-year survival is about 70%; life expectancy is 8.5 years. Medical management of transplant patients is challenging. Patients become used to their LVAD, and many come to like it. Some patients remove themselves from the transplant list. The LVAD becomes an "end of life" therapy.

One such person comes each year to speak to the class. He is now about 40 years old.[1] As a young man in his low thirties, he was suddenly diagnosed with heart failure. Unbenownst to him, he had had a bacterial infection which degraded his tricuspid valve completely. Regurgitation naturally followed and his heart overworked itself attempting to maintain blood flow. It quickly gave out.

He was a strong candidate for a transplantable heart. He had an LVAD placed as a "bridge to transpant" therapy. Physicians expected it to last 3–5 years. His physicians' mean wait time for a heart was eighteen months. He was sure to receive a new heart.

But he did not. After two years of living with his LVAD, no compatible hearts had appeared. By then he had found a comfortable routine. He was able to wash himself just fine, stay active, keep a job, and he had a good quality of life.

He chose to remove himself from the transplant list. The drawbacks of an LVAD were acceptable to him, and he no longer wanted to take on the drawbacks of a transplanted heart. He has had an LVAD for about 8 years. It shows no signs of stopping! It is a

[1] Some details have been changed.

deeply emotional discussion to interact with someone who has chosen to let the success or failure of a mechanical device determine how long *and how well* they live.

It is also heartwarming to hear that such a device exists. We should invent more: improved management of heart failure patients is crucial to the future of healthcare. Heart failure is the most important cardiovascular issue to be solved today [Carpentier 2007].

The long-term care of a heart failure patient is challenging. A patient will typically see a heart failure specialist once or twice per year; and also and also be hospitalized with an acute condition once or twice per year; and also their primary care physician must consider their heart failure in every diagnosis and treatment, no matter now mundane. As the number of heart failure patients grows this creates a huge demand for predictive treatment strategies of all types, not just for LVADs.

Another guest speaker each year is a surgeon who speaks on his specialty, vascular hemodynamics, and also his three voluntary tours of duty in Germany as a military surgeon treating fresh battle wounds from soldiers fighting in Iraq and Afghanistan. It's a surprise to go to Germany to operate on soldiers wounded in the Middle East. It means that some presumably intelligent, well educated military administrator decided it would be a good idea to station the battlefield surgery team *seven thousand miles away from the battlefield!*

Figure 44: Forward surgical team in Asia prepares for a mission, 2011. Photo by U.S. Air Force Senior Airman Cassandra Locke [Locke 2011].

In fact, it's a brilliant idea that has saved thousands of lives. Twenty battlefield medics travel in humvees, directly behind battlefield lines, and set up a 900-square-foot hospital facility with four ventilator-equipped recovery beds and two operating tables. They can go from driving to open surgery in less than an hour. The teams travel as light as possible. For instance, they do not use an x-ray machine. Broken bones are detected by feel.

They stabilize wounded as quickly as possible—in under two hours—and immediately ship them out—often still anesthetized—to the next medical team at the next level of care. Anyone requiring more than three days' treatment goes to Germany, anyone requiring more than thirty days goes to Walter Reed or San Antonio. Once the system was in full swing, the average time to reach Germany was two days, the U.S. in less than four.

It's similar to the idea of arriving at a hospital and going first to the Emergency Room, then the Intensive Care Unit, and then to a bed on a floor. Except they're ten thousand miles apart, and the Emergency Room follows you around.

Figure 45: Forward surgical team in Kuwait, 2005. Two intensive care recovery beds are shown. Photo courtesy U.S. Army Captain Herman Allison [Allison 2005].

The novelty of the idea lies in separating the necessary surgery into separate surgeries. The main surgery team needs too much equipment and support to be close to the battlefield. The battlefield surgeon's role is only to stabilize the patient. He

doesn't even try to finish the surgery. Yet both surgical teams have to work in harmony with very little patient workup. This is a huge change from typical Western healthcare.

To see how it's worked, consider that in each of the Korean War, the Vietnam War, and the Gulf War, we saved 75% of wounded US soldiers. In Iraq and Afghanistan, we saved 90%.

None of this required new technology: nothing more than aggressive first-line treatment within five minutes, and a trust that the team at the next level can care for your patient as well as you, has saved ten thousand lives.

Many issues arose, some of them perfect for a Cardiovascular Engineering design team. Perhaps due to the lengthy air travel, there were high rates of pulmonary embolism and deep vein thrombosis. Five percent of the soldiers who went to Walter Reed contracted a pulmonary embolism. Engineers could design a new inferior vena cava filter, and perhaps eliminate this issue. [Gawande 2004]

These teams travel light. Software is light. What can computational medicine provide for acute care? This actually raises an important observation. Most predictive computational medicine is designed around chronic conditions. The fields of acute care and especially emergency care are ripe for predictive modeling.

8.1.2 *Pathophysiology and Epidemiology of Cardiovascular Disease*

Another course developed was *Pathophysiology and Epidemiology of Cardiovascular Disease*, taught by Tate Erlinger MD and myself. The course was taught from 2006 to 2013. Dr. Erlinger is Medical Director at Seton Health Alliance and Vice President of Clinical Effectiveness and Care Redesign within the Center for Experience and Effectiveness. While teaching the course, he was also formerly Director of Research Administration Infection

Prevention & Epidemiology at Seton Family of Hospitals, Chief Medical Officer for a local health insurance agency, and State Epidemiologist for Texas Department of State Health Services.The course appeals to engineers, kinesiologists, and nurses. It provides insight into the assessment of cardiovascular disease, reading studies published in medical literature, and understanding ways of effectively introducing technology into medical practice. An example is illustrative.

There were many studies—such as [Illingworth 2000]—which pharmaceutical companies used to argue massive overindulgence in statin use. This meta-study seems to show lower LDL indicates lower coronary heart disease (CHD) risk, which had already been established as true. Pharmaceutical companies argue low density lipoprotein (LDL) levels should be pushed as low as possible, because no minimum safe level of LDL has been observed, and patients naturally want the lowest CHD risk possible. Statins are well-tolerated, have comparatively few side effects, and they seem not to have many negative interactions with other medications. Pharmaceutical companies aggressively push increased statin dosage.

But none of the studies showed that increasing dosage had increased benefit. They only showed getting a nominal dose was better than getting no dose; and that people whose LDL happened to be lower had fewer CHD events. There is no reason to think LDL levels should be a target. The treatment guidelines said that if LDL was above a certain amount, giving a statin was shown to have benefit. The treatment guidelines did *not* say that if LDL was above a certain amount, *giving enough drugs to push the LDL level down as far as possible* was shown to have benefit.

The meta-analysis statin manufacturers used is an observational study. Study subjects weren't randomized to pre-determined LDL values; they were randomized to a given statin dosage. So we can only say for certain that statins are better than placebo at lowering risk. But we never ran the study of randomizing people to achieve certain LDL values (regardless of how much exercise or how much dosage it took to get there). And until we do, the guidelines will only be to give a statin based on reducing overall CVD risk.

Certain study subjects may have achieved lower LDL levels, and also had better outcomes, and that correlation may have been compelling; but we did not confirm that causing the LDL to go lower than what the subject happened to have achieved would continue to improve that subject's outcome.

None of the studies targeted LDL and pushed their patients to a certain LDL level. None of the studies said to keep driving patients' LDL levels down further and further. But that's what physicians did. That's what drug salesmen harangued physicians to do. According to misinterpreted findings and aggressive advice, many physicians increased statin dosage until patients reached certain LDL targets.

This is not an unreasonable mistake to make. Comparisons of LDL and CHD show LDL distributions of people with and without CHD are surprisingly similar [Castelli 1996]. Also, there is increased risk of CHD with higher levels of LDL [Martin 1996]. There is an exponential increase in risk, even at low levels of risk. No matter what one's LDL level was, or how much it had been treated, it seems that lowering further is always better. And federal policies inadvertently promoted this kind of thinking. Lowering the nation's average cholesterol level became a priority, one that saved tens of thousands of lives per year.

An overly-aggressive interpretation was so pervasive that in 2013, the new recommendations by the National Heart, Lung, and Blood Institute were released, ATP IV. It reminded everyone not to lose sight of the proper target: ten-year risk. ATP IV reminded physicians not to move LDL to certain targets, but to use statins—as only one part of an entire treatment plan—in order to minimize ten-year risk of heart attack, according to a certain reasonable formula. That is, physicians should treat patients to control their level of cardiovascular risk, based upon an estimated 10-year risk or a lifetime risk of cardiovascular disease.

In fact, *The New York Times* went further: they pointed out that the usual non-drug LDL-lowering therapies—diet, exercise even in small amounts, stopping smoking—remain superior to drug therapies [Abramson 2013]. Where is the billion-dollar industry behind these treatments? Why do health insurers ignore them?

In the class, I give students an understanding of clinical trials and what they actually tell us, so they can avoid this kind of mistake. When we understand how health indicators are measured, we can understand how to improve them.

I discuss gaps in measurement technology. For example, I do not have a model for how the placenta works! Fetal heart rate is the only measurement of overall fetal health. There is no noninvasive way to measure blood pressure of a fetus, nor any measure of blood nutrients. Consider that pregnancy is the single most common reason for admission to a hospital, and that blood pressure is by far the single most commonly measured indicator of health. A good computer model for placenta would be an overnight billion-dollar industry.

8.1.3 *Cardiovascular Dynamics*

This course, ME 385J topic 5, emphasized the design and application of electrical and mechanical devices for cardiac intervention. It has not been offered in over fifteen years. It would be an excellent followup to *Clinical Cardiology*.

8.1.4 *Hospital Interfaces*

ME 385J topic 11, was taught by Thomas Runge MD, who held a Clinical Professorship in the School of Engineering and was the first cardiologist in Austin. His class was the first course in the country to give graduate Biomechanical Engineering students at chance to observe everyday workings of hospital laboratories. Students would shadow Dr. Runge and other physicians on their rounds at a local hospital. While demonstrating hospital life and introducing students to patients and letting them share their stories, he explained medicine from a healthcare perspective. (*Clinical Cardiology* explains medicine from a surgical or interventional perspective.) Among other topics, he discussed the engineering implications of providing electricity, clean water, breathable gases, wastewater removal, and sterilization for a large hospital. The scalability requirements and the life-threatening prospect of less than 99.9% uptime of utilities is a modern day accomplishment. [Baker 2008]

This was done at the nearby Brackenridge hospital, a central Austin trauma center. Future courses could be developed at Brackenridge, the new Dell Medical Center, or at Heart Hospital of Austin.

8.2 Faculty and student access to observe medical procedures

Following in the footsteps of *Hospital Interfaces*, the Department of Mechanical Engineering and the Institute for Computational Engineering and Sciences at UT have developed additional means for teaching Engineers the day-by-day vagaries of healthcare.

The programs have been folded into the courses described above, but they are important and difficult to create and maintain, and they deserve additional discussion. Until UT's School of Engineering sets up an official long-term contract with the two nearby hospital systems, there will be barriers to student engineers collaborating with physicians.

8.2.1 Preceptorship at Heart Hospital of Austin

A second important feature of the *Clinical Cardiology* course is the establishment of a preceptorship at Heart Hospital of Austin, a campus of St. David's Medical Center. Thanks to the efforts of Kent Beasley, myself, and many others, students are able to visit the Heart Hospital to observe surgical procedures such as catheterization, cardiac bypass, and robotic surgery.

This is an ongoing opportunity that has developed a collegial environment whereby practicing physicians are aware of engineering research, educated in various ongoing projects, and interested in assisting. A friendly, collaborative atmosphere is crucial to success.

The preceptorship is enabled through an agreement with St. David's HealthCare. Students are allowed to visit the hospital for up to 8 hours.

Ideally, The University of Texas at Austin and St. David's HealthCare would create a long-term institutional agreement to allow student observers. However, when St. David's HealthCare bought Heart Hospital of Austin, St. David's asked UT to sign an onerous boilerplate contract meant for student visitors who participate in patient care—

e.g., nursing students who perform blood draws. UT rejected the contract, putting the course in jeopardy. Subsequently, ICES and Dr. Beasley went to great effort to achieve a tentative agreement from UT and St. David's representatives to draw up an appropriate contract.

8.2.2 Cardiology rounds at Brackenridge Hospital

In order to learn cardiology, I followed physicians on rounds at Brackenridge Hospital as part of the Residency Program at The University of Texas Medical Branch, particularly under David W. Hayes MD, Chief of Staff at University Medical Center at Brackenridge. It was an opportunity similar in nature to the *Hospital Interfaces* course mentioned above. On these rounds, I went through case studies, visited with patients, observed stress echocardiography, read EKGs, and observed surgical procedures. I saw many common hospital Primarily, I helped set up a pathway for other engineering students and professors to learn clinical cardiology. That pathway led to *Clinical Cardiology* and the Heart Hospital of Austin preceptorship.

8.3 Physician access to engineering research

Face time spent between engineers and physicians is crucial to joint success. As engineers, we need to be creative to find ways to encourage physicians to spend time away from their practice working on long-term projects. This is especially true as it is logistically difficult and time-consuming for visitors to enter campus.

8.3.1 Seminar series

There are a few ongoing seminar series devoted to connecting engineers with physicians. One of these is the Computational Medicine Spring Lecture Series, in its first

year [ICES 2015]. Seminars are presented by engineering professors and attended by both academics and local physicians. In coming seminars, physicians will present seminars on medical care and issues that can be addressed by engineering technologies.

These seminars are distinct from *Clinical Cardiology* seminars, in that the thurst is to bring the application of computational medicine closer to clinical practice. It highlights emerging or longstanding issues in clinical care, and facilitates discussion of research directions for addressing these issues.

Another important aspect of the seminars is it brings engineers and physicians together in ongoing discussions of medicine and engineering. Seeds from such discussions grow into improved healthcare.

8.3.2 Continuing Medical Education

One way to provide value for physicians is through Continuing Medical Education (CME). CME is a process by which physicians learn new techinques and stay current with medical developments. Many states (including Texas) require CME for physicians to maintain licensure. The University of Texas at Austin – University Health Services is accredited by Texas Medical Association to provide CME. University Health Services could work with the Institute for Computational Engineering and Sciences so that Computational Medicine seminars provide CMEs for attendees. There could be dedicated CME seminars presenting engineering advancements in medicine.

Chapter 9

Conclusions

The biggest challenge to simulating behavior of tissues (or any phenomenon) is and always will be modeling. Researchers must determine relevant behavior, create constitutive laws to describe that behavior, establish conditions under which the laws are valid, and assess the manner and extent of their validity. Knowing how a given tissue behaves and knowing ways in which these behaviors can be represented in Biomechanical theory is the primary focus of every modeler.

This work fills three roles that meet this challenge: it is intended as an improvement over current best practices in arterial modeling; as a means for combining the entire image data–to–simulation pathway; and for building a viable parameter space.

I have also worked to connect engineers with physicians to improve healthcare strategies. The Stages concept in this work provides a common language with which biomechanical engineers can communicate with physicians. Using the model, questions in one field can be translated into equivalent questions in another. This work serves as a new strategy to improve early detection and treatment of aneurysms.

Computer simulation can provide improved medical treatment if stakeholders from all relevant fields work together to build a multidisciplinary framework to discover solutions. I have provided a bridge between fields. Through direct results and their inevitable application to other areas, continued work in this area will have an impact on the biomechanical literature and medical practice.

I created a pipeline of tools for simulations, using patient-specific geometries from medical image data. I constructed novel constitutive models for fiber behavior. I have built the first simulation of saccular aneurysm initiation and enlargement from a healthy artery. I identified stages of aneurysm disease that connect clinical findings with mathematical relations. I identified sensitive parameters within the model which explain the model's behavior. I used these findings to propose novel experiments which can explore the disease process to help determine risk of aneurysm enlargement.

Bibliography

[Abramson 2013] J.D. Abramson, R.F. Redberg, "Don't Give More Patients Statins," *The New York Times*, November 13, 2013, `http://www.nytimes.com/2013/11/14/opinion/dont-give-more-patients-statins.html`.

[A.D.A.M., Inc. 2007] A.D.A.M., Inc., "Cerebral Aneurysm," *MedlinePlus Medical Encyclopedia*, 2006, `http://www.nlm.nih.gov/medlineplus/ency/imagepages/17031.htm`, retrieved on December 2, 2007.

[Albeck 1991] M.J. Albeck, S.E. Børgesen, F. Gjerris, J.F. Schmidt, P.S. Sørensen, "Intracranial pressure and cerebrospinal fluid outflow conductance in healthy subjects," *Journal of Neurosurgery*, **74**(4):597–600, 1991, doi: 10.3171/jns.1991.74.4.0597.

[Allison 2005] H. Allison, United States Army, 2005.

[Antman 2005] S.S. Antman, J.E. Marsden, and L. Sirovich, editors, *Nonlinear Problems of Elasticity*, Springer-Verlag, New York, 2005.

[Baker 2008] L. Baker, S.A. Greninger, W. Powers Jr, "In Memoriam: Thomas Marschall Runge," *The University of Texas at Austin*, Office of the General Faculty & Faculty Council, 2007, `http://www.utexas.edu/faculty/council/2007-2008/memorials/runge.html`

[Baek 2006] S. Baek, K.R. Rajagopal, J.D. Humphrey, "A Theoretical Model of Enlarging Intracranial Fusiform Aneurysms," *Journal of Biomedical Engineering*, **128**(11):142–149, February 2006, doi: 10.1115/1.2132374.

[Baek 2007] S. Baek, A. Valentín, J.D. Humphrey, "Biochemomechanics of cerebral vasospasm and its resolution: II. Constitutive relations and model simulations," *Annals of Biomedical Engineering*, **35**(9):1498–1509, 2007, doi: 10.1007/s10439-007-9322-x.

[Bazilevs 2006] Y. Bazilevs, V.M. Calo, Y. Zhang, and T.J.R. Hughes, "Isogeometric fluid-structure interaction analysis with applications to arterial blood flow," *Computational Mechanics*, **38**:310–322, 2006, doi: 10.1007/s00466-006-0084-3.

[Beck 2006] J. Beck, S. Rohde, J. Berkefeld, V. Siefert, A. Raabe, "Size and location of ruptured and unruptured intracranial aneurysms measured by 3-dimensional rotational angiography," *Surgical Neurology*, **65**:18–27, 2006, doi: 10.1016/jsurneu.2005.05.019.

[Canham 1992] P.B. Canham, P. Whittaker, S.E. Barwick, M.E. Schwab, "Effect of pressure on circumferential order of adventitial collagen in human brain arteries," *Canadian Journal of Physiology and Pharmacology*, **70**(2): 296–305, February 1992.

[Carpentier 2007] A.F. Carpentier, C. Rose, "A conversation with Dr. Alain F. Carpentier," *Charlie Rose*, PBS, KLRU, Austin, Texas, 25 December 2007, `http://charlierose.com/shows/2007/12/25/1/a-conversation-with-dr-alain-f-carpentier`.

[Cebral(1) 2005] J.R. Cebral, M.A. Castro, S. Abbanaboyina, C.M. Putman, D. Millan, A.F. Frangi, "Efficient Pipeline for Image-Based Patient-Specific Analysis of Cerebral Aneurysm Hemodynamics: Technique and Sensitivity," *IEEE Transactions on Medical Imaging*, **24**:457–467, April 2005, doi: 10.1109/tmi.2005.844159.

[Cebral(2) 2005] J.R. Cebral, M.A. Castro, J.E. Burgess, R.S. Pergolizzi, M.J. Sheridan, C.M. Putman, "Characterization of cerebral aneurysm for assessing risk of rupture by using patient-specific computational hemodynamics models," *American Journal of Neuroradiology*, **26**(10):2550–2559, November–December 2005.

[Chapman 1990] P.H. Chapman, E.R. Cosman, M.A. Arnold, "The relationship between ventricular fluid pressure and body position in normal subjects and subjects with shunts: a telemetric study," *Neurosurgery*, **26**(2):181–189, 1990.

[Ciarlet 1988] P. Ciarlet, *Mathematical Elasticity*, Elsevier, 1988.

[Cottrell 2006] J.A. Cottrell, A. Reali, Y. Bazilevs, and T.J.R. Hughes, "Isogeometric analysis of structural vibrations," *Computer Methods in Applied Mechanics and Engineering*, **195**:5257–5296, 2006.

[Cottrell 2009] J.A. Cottrell, T.J.R. Hughes, Y. Bazilevs, *Isogeometric analysis: Toward Integration of CAD and FEA*, Wiley, Chichester, 2009.

[Castelli 1996] W. Castelli, "Lipids, risk factors and ischaemic heart disease," *Atherosclerosis*, **124**:S1–S9, July 24, supplement, 1996, PubMedID: 8831910.

[deBotton 2006] G. deBotton, I. Hariton, E.A. Socolsky, "Neo-Hookean fiber-reinforced composites in finite elasticity," *Journal of the Mechanics and Physics of Solids*, **54**(3):533–559, March 2006, doi: 10.1016/j.jmps.2005.10.001.

[Dispensa 2007] B.P. Dispensa, D.A. Saloner, G. Acevedo-Bolton, A.S. Achrol, L. Jou, C.E. McCulloch, S.C. Johnston, R.T. Higashida, C.F. Dowd, V.V. Halbach, N.U. Ko, M.T. Lawton, A.J. Martin, N. Quinnine, W.L. Young, "Estimation of fusiform intracranial aneurysm growth by serial magnetic resonance imaging," *Journal of Magnetic Resonance Imaging*, **26**:177–183, July 2007, PubMedID: 17659544.

[Draney 2004] M.T. Draney, F.R. Arko, M.T. Alley, M. Markl, R.J. Herfkens, N.J. Pelc, C.K. Zarins, C.A. Taylor, "Quantification of vessel wall motion and cyclic strain using cine phase contrast MRI: In vivo validation in the porcine aorta," *Magnetic Resonance in Medicine*, **52**(2):286–295, August 2004.

[Englund 1998] R. Englund, P. Hudson, K. Hanel, A. Stanton, "Expansion rate of small abdominal aortic aneurysms," *Australian and New Zeland Journal of Surgery*, **68**(1):21–24, January 1998.

[Eriksson 2009] T. Eriksson, M. Kroon, G.A. Holzapfel, "Influence of Medial Collagen Organization and Axial In Situ Stretch on Saccular Cerebral Aneurysm Growth," *Journal of Biomechanical Engineering*, **131**:101010-1–7, October 2009, doi: 10.1115/1.3200911.

[Evans 2015] E.J. Evans, M.A. Scott, X. Li, D.C. Thomas, "Hierarchical T-splines: Analysis-suitability, Bézier extraction, and application as an adaptive basis for isogeometric analysis," *Computer Methods in Applied Mechanics and Engineering*, **284**:1–20, 2015.

[Folsom 1994] A.R. Folsom, J.H. Eckfeldt, S. Weitzman, J. Ma, L.E. Chambless, R.W. Barnes, K.B. Cram, R.G. Hutchinson, for the Atherosclerosis Risk in Communities (ARIC) Study Investigators, "Relation of Carotid Artery Wall Thickness to Diabetes Mellitus, Fasting Glucose and Insulin, Body Size, and Physical Activity," *Stroke,* **25**(1):66–73, January 1994, doi: 10.1161/01.STR.25.1.66.

[Fung 1993] Y.C. Fung, *Biomechanics: Mechanical Properties of Living Tissues*, Springer-Verlag, New York, 1993, ISBN 0-387-97947-6.

[Gasser 2006] T.C. Gasser, R.W. Ogden, G.A. Holzapfel, "Hyperelastic modelling of arterial layers with distributed collagen fibre orientations," *Journal of the Royal Society Interface*, **3**:15–35, 2006, doi: 10.1098/rsif.2005.0073.

[Gasser 2012] T.C. Gasser, S. Gallinetti, X. Xing, C. Forsell, J. Swedenborg, J. Roy, "Spatial orientation of collagen fibers in the abdominal aortic aneurysm's wall and its relation to wall mechanics," *Acta biomaterialia,* **8**(8):3091–3103, 2012.

[Gawande 2004] A. Gawande, "Casulaties of War—Military Care for the Wounded from Iraq and Afghanistan," The New England Journal of Medicine, **351**(24):2471–2475, 2004, `https://www.nejm.org/doi/pdf/10.1056/NEJMp048317`.

[Gleason 2007] R.L. Gleason, E. Wilson, J.D. Humphrey, "Biaxial biomechanical adaptations of mouse carotid arteries cultured at altered axial extension," *Journal of Biomechanics*, **40**:766–776, 2007, doi: 10.1016/j.jbiomech.2006.03.018.

[Gonzalez 2008] O. Gonzalez, A.M. Stuart, *A First Course in Continuum Mechanics*, Cambridge University Press, 2008.

[Heiss 1991] G. Heiss, A.R. Sharrett, R. Barnes, L.E. Chambless, M. Szklo, C. Alzola, and the ARIC Investigators. "Case-control analysis of atherosclerosis and established risk factors," *American Journal of Epidemiology* **134**: 250–256, 1991.

[Hariton 2007] I. Hariton, G. deBotton, T.C. Gasser, G.A. Holzapfel, "Stress-driven collagen fiber remodeling in arterial walls," *Biomechanics and Modeling in Mechanobiology*, **6**:163–175, 2007, doi: 10.1007/s10237-006-0049-7.

[HIPAA] United States Department of Health and Human Services, "Health Information Privacy," `https://www.hhs.gov/ocr/privacy`.

[Holzapfel 2000] G.A. Holzpafel, *Nonlinear Solid Mechanics*, Wiley & Sons, New Jersey, 2000.

[TJRH 1987] T.J.R. Hughes, "Efficient and Simple Algorithms for the Integration of General Classes of Inelastic Constitutive Equations Including Damage and Rate Effects: Application to the Cap Model for Soils and Concrete," *Algorithms for the Integration of Inelastic Constitutive Equations Including Rate and Damage*, Ft. Belvoir Defense Technical Information Center, Stanford, CA, February 1987.

[TJRH(1) 2005] T.J.R. Hughes, J.A. Cottrell, Y. Bazilevs, "Isogeometric analysis: CAD, finite elements, NURBS, exact geometry, and mesh refinement," *Computer Methods in Applied Mechanics and Engineering*, **194**:4135–4195, 2005.

[TJRH(2) 2005] T.J.R. Hughes, F. Nugen, "Patient-Specific Mathematical Models of the Heart for Simulation-Based Medical Planning," *ICES Report 05-26*, Institute for Computational Engineering and Sciences, The University of Texas at Austin, 2005, `https://www.ices.utexas.edu/research/reports/2005/0526.pdf`.

[Humphrey 2000] J.D. Humphrey, P.B. Canham, "Structure, Mechanical Properties, and Mechanics of Intracranial Saccular Aneurysms," *Journal of Elasticity*, **61**:49–81, 2000.

[Humphrey(1) 2002] J.D. Humphrey, K.R. Rajagopal, "A Constrained Mixture Model for Growth and Remodeling of Soft Tissues," *Mathematical Models and Methods in Applied Sciences*, **12**(3):407–430, March 2002, doi: 10.1142/s0218202502001714.

[Humphrey(2) 2002] J.D. Humphrey, *Cardiovascular Solid Mechanics: Cells, Tissues, and Organs*, Springer-Verlag, Berlin Heidelberg New York, 2002.

[ICES 2015] "ICES hosts Spring Computational Medicine Lectures," Dec. 7, 2015, retrieved from https://www.ices.utexas.edu/about/news/393/.

[Ikari 2005] Y. Ikari, N. Masakazu, J.-Y. Kim, Y. Morino, T. Tanabe, "The physics of guiding catheters for the left coronary artery in transfemoral and transradial interventions," *Journal of Invasive Cardiology*, **17**(12):636–641, December 2005.

[Illingworth 2000] D.R. Illingworth, "Management of hypercholesterolemia," *Med Clin North Am*, **84**(1):23–42, January, 2000. PubMedID: 10685126.

[itk.org] *National Library of Medicine Insight Segmentation and Registration Toolkit*, Insight Software Consortium, http://www.itk.org.

[Ivanov 2014] D. Ivanov, A. Dol, O. Pavlova, A. Aristambekova, "Modeling of human circle of Willis with and without aneurisms," *Acta of Bioengineering and Biomechanics*, **16**(2):121–129, 2014, doi:10.5277/abb140214.

[Jou 2005] L.-D. Jou, G. Wong, B. Dispensa, M.T. Lawton, R.T. Higashida, W.L. Young, D. Saloner, "Correlation between lumenal geometry changes and hemodynamics in fusiform intracranial aneurysms," *American Journal of Neuroradiology*, **26**(9):2357–2363, October 2005, PubMedID: 16219845.

[Kar 2005] B. Kar, R.M. Delgado, O.H. Frazier, I.D. Gregoric, M.T. Harting, Y. Wadia, T.J. Myers, R.D. Moser, J. Freund, "The effect of LVAD investigation aortic outflow-graft placement on hemodynamics and flow—implantation technique and computer flow modeling," *Texas Heart Institute Journal*, **32**(3):294–298, 2005.

[Kroon 2007] M. Kroon, G.A. Holzapfel, "A model for saccular cerebral aneurysm growth by collagen fibre remodeling," *Journal of Theoretical Biology*, **247**:775–787, March 2007, doi: 10.1016/j.jtbi.2007.03.009.

[Langner 2010] J. Langner, "PET-image.jpg" and "File:PET-MIPS anim frame.PNG," https://en.wikipedia.org/wiki/File:PET-image.jpg and https://commons.wikimedia.org/wiki/File:PET-MIPS_anim_frame.PNG, 2010.

[Lasheras 2007] J.C. Lasheras, "The Biomechanics of Arterial Aneurysms," *Annual Review of Fluid Mechanics*, **39**:293–319, 2007, doi: 10.1146/annurev.fluid.39.050905.110128.

[Locke 2011] C. Locke, "Operation Enduring Freedom," United States Air Force, 051013-F-4469L-001.JPG, http://www.af.mil/News/Photos.aspx?igphoto=2000578164, 2011.

[Lu 2013] J. Lu, S. Hu, M.L. Raghavan, "A shell-based inverse approach of stress analysis in intracranial aneurysms," *Annals of Biomedical Engineering*, **41**(7):1501–1515, July 2013.

[Lubarda 2002] V.A. Lubarda, A. Hoger, "On the mechanics of solids with a growing mass," *International Journal of Solids and Structures*, **39**:4627–4664, 2002, doi: 10.1016/S0020-7683(02)00352-9.

[Lynch 2006] P.J. Lynch, C.C. Jaffee, "Heart left ventricular aneurysm short axis view," `http://commons.wikimedia.org/wiki/Image:Heart_left_ventricular_aneurysm_sa.jpg`, Center for Advanced Instructional Media, Yale University School of Medicine, 2006; retrieved on December 2, 2007.

[Martin 1996] M.J. Martin, S.B. Hulley, W.S. Browner, L.H. Kuller, D. Wentworth, "Serum cholesterol, blood pressure, and mortality: implications from a cohort of 361,662 men," *The Lancet*, **2**(8513):933–936, October 25, 1996. PubMedID: 2877128.

[Messas 2013] E. Messas, M. Pernot, M. Couade, "Arterial wall elasticity: State of the art and future prospects," *Diagnostic and Interventional Imaging*, **94**(5):561–569, 2013, doi: 10.1016/j.diii.2013.01.025.

[Mizoi 1989] K. Mizoi, J. Suzuki, T. Yoshimoto, "Surgical treatment of multiple aneurysms: review of experience with 372 cases," *Acta Neurochirurgica (Wien)*, Jan–Feb, **96**(1–2):8–14, 1989.

[Nader-Sepahi 2004] A. Nader-Sepahi, M. Casimiro, J. Sen, N.D. Kitchen, "Is aspect ratio a reliable predictor for intracranial aneurysm rupture?", *Neurosurgery*, **54**(6):1343–1348, June 2004, doi: 10.1227/01.neu.0000124482.03676.8B.

[Netter 2003] F. Netter, *Atlas of Human Anatomy, Third Edition*, Icon Learning Systems, Teterboro, New Jersey, 2003.

[Obbink-Huizer 2014] C. Obbink-Huizer, J. Foolen, C.W.J. Oomens, M.A. Borochin, C.S. Chen, C.V.C. Bouten, F.P.T. Baaijens, "Computational and experimental investigation of local stress fiber orientation in uniaxially and biaxially constrained microtissues," *Biomechanics and Modeling in Mechanobiology*, **13**(5):1053–1063, 2014.

[Pena 2014] E. Pena, "Computational aspects of the numerical modelling of softening, damage and permanent set in soft biological tissues," *Computers & Structures*, **130**:57–72, 2014.

[Saez 2014] P. Saez, E. Pena, M.A. Martinez, "A Structural Approach Including the Behavior of Collagen Cross-Links to Model Patient-Specific Human Carotid Arteries," *Annals of Biomedical Engineering*, **42**(6):1158–1169 (2014).

[Saez 2015] P. Saez, E. Pena, J. M. Tarbell, M.A. Martinez, "Computational model of collagen turnover in carotid arteries during hypertension," *International Journal for Numerical Methods in Biomedical Engineering*, **31**:e02705 (2015).

[Saloner 2005] D. Saloner, personal communications through J.D. Humphrey.

[Schmid 2013] H. Schmid, A. Grytsan, E. Poshtan, P.N. Watton, M. Itskov, "Influence of differing material properties in media and adventitia on arterial adaptation—application to aneurysm formation and rupture," *Computer Methods in Biomechanics and Biomedical Engineering*, **16**(1):33–53, 2013.

[Scott 1972] S. Scott, G.G. Ferguson, M.R. Roach, "Comparison of the Elastic Properties of Human Intracranial Arteries and Aneurysms," *Canadian Journal of Physiology and Pharmacology*, **50**(4):328–332, 1972, PubMedID: 5038350.

[Simo, Hughes 1998] J.C. Simo, T.J.R. Hughes, *Computational Inelasticity*, Springer, New York, 1998.

[Smith 1981] J.F.H. Smith, P.B. Canham, J. Starkey, "Orientation of collagen in the tunica adventitia of the human cerebral artery measured with polarized light and the universal stage," *Journal of Ultrastructure Research*, **77**(2):133–145, 1981.

[de Souza Neto 2008] E.A. de Souza Neto, D. Perić, D. Owens, *Computational Methods for Plasticity: Theory and Applications*, Wiley & Sons, United Kingdom, 2008.

[Starke 2014] R.M. Starke, "Vascular Smooth Muscle Cells in Cerebral Aneurysm Pathogenesis," *Translational Stroke Research*, **5**(3):338–346, 2014.

[Taber 2000] L.A. Taber, R. Perucchio, "Modeling Heart Development," *Journal of Elasticity*, **61**:165–197, 2000.

[Taber 2001] L.A. Taber, "Biomechanics of Cardiovascular Development," *Annual review of Biomedical Engineering*, **3**:1–25, 2001, doi: 10.1146/annurev.bioeng.3.1.1.

[Taylor 1998] C.A. Taylor, T.J.R. Hughes, and C.K. Zarins, "Finite Element Modeling of Blood Flow in Arteries," *Computer Methods in Applied Mechanics and Engineering*, **158**:155–196, 1998.

[Taylor 2003] C.A. Taylor, personal communications.

[Taylor 2007] C.A. Taylor, A. Figueroa, personal communications.

[Wei 2012] C.-C. Wei, S.-W. Huang, C.-T. Bau, "Using the spring constant method to analyze arterial elasticity in type 2 diabeticpatients," *Cardiovascular Diabetology*, **11**(39), 2012, doi: 10.1186/1475-2840-11-39.

[Wicker 2008] B.K. Wicker, H.P. Hutchens, Q. Wu, A.T. Yeh, J.D. Humphrey, 2008 "Normal basilar artery structure and biaxial mechanical behaviour". *Comput. Methods Biomech. Biomed. Eng.* **11**:539–551, doi:10.1080/10255840801949793.

[Winkler 1867] E. Winkler, "Die Lehre von der Elasticitaet und Festigkeit – mit besonderer Rücksicht auf ihre Anwendung in der Technik, für polytechnische Schulen, Bauakademien, Ingenieure, Maschinenbauer, Architekten, etc.," Verlag H. Dominicus, Prague, 1867.

[ISUIA 2003] D.O. Wiebers, J.P. Whisnant, J. Huston 3rd, I. Meissner, R.D. Brown Jr, D.G.Piepgras, G.S. Forbes, K. Thielen, D. Nichols, W.M. O'Fallon, J. Peacock, L. Jaeger, N.F. Kassell, G.L. Kongable-Beckman, J.C. Torner, International Study of Unruptured Intracranial Aneurysms Investigators, "Unruptured intracranial aneurysms: natural history, clinical outcome, and risks of surgical and endovascular treatment," *The Lancet*, **362**(9378):103–110, July 12, 2003, PubMedID: 12867109.

[Wulandana 2005] R. Wulandana, A.M. Robertson, "An inelastic multi-mechanism constitutive equation for cerebral arterial tissue," *Biomechanics and Modeling in Mechanobiology*, **4**(4):235–248, 2005, doi:10.1007/s10237-005-0004-z.

[Zaorsky 2011] N. Zaorsky, "The most common sites of intracranial saccular aneurysms," `https://commons.wikimedia.org/wiki/File:Wikipedia_intracranial_aneurysms_-_inferior_view_-_heat_map.jpg`

[Zeller 1998] P.J. Zeller, T.C. Skalak, "Contribution of Individual Structural Components in Determining the Zero-Stress State in Small Arteries," *J Vasc Res*, **35**(1):8–17, 1998.

Description of Symbols and Abbreviations

$\mathcal{B}$ material body

$\partial\mathcal{B}$ boundary of $\mathcal{B}$

$\mathbb{C}$ elasticity tensor

$\chi_A(x)$ characteristic function on the set A

$\frac{\partial}{\partial t}|_{\boldsymbol{X}}$ material derivative

δ_{ij} delta function; $\delta_{ij} = 1$ if $i = j$, 0 otherwise

E Young's modulus

$g(\boldsymbol{X}, t)$ essential boundary condition, applied to Γ_{inlet} and Γ_{outlet}

Γ_g domain of essential boundary conditions (in the reference system); the material's position is prescribed on this boundary; $\Gamma_g = \Gamma_{\text{inlet}} \cup \Gamma_{\text{outlet}}$

Γ_h domain where the natural boundary conditions are applied (in the reference system); external pressures are prescribed on this boundary; $\Gamma_h = \Gamma_{\text{interior}} \cup \Gamma_{\text{exterior}}$

$h(\boldsymbol{X}, t)$ natural boundary condition, applied to Γ_{interior} and Γ_{exterior}

$H^1(\Omega_0)$ Sobolev space

J ratio of current volume to reference volume; $J(\boldsymbol{X}, t) = \det F(\boldsymbol{X}, t)$

k-fiber: fiber from family $k = 1, 2$; the distinction between the two fiber families is the directions in which they point; the families are otherwise treated identically

K_g growth constant; $K_g \in [0, 1]$ [Baek 2006]

$\lambda^k(\tau, t)$ stretch at time t of k-fibers placed at time τ

$\boldsymbol{m}^k(\tau, t)$ orientation at time t of k-fibers placed at time τ

$\boldsymbol{N}$ outward-pointing unit normal in the reference configuration

$\boldsymbol{N}^A$ NURBS basis functions comprising $\mathcal{V}^h$ and $\mathcal{S}^h$

ν Poisson's ratio

Ω_0 set of $\boldsymbol{X}$ in $\mathcal{B}$ at time 0

Ω_t set of $\boldsymbol{x}$ in $\mathcal{B}$ at time t

p_{BP} average blood pressure, constant at GNR timescale, applied to Γ_{interior}

p_{brain} pressure boundary condition on the exterior of the artery; derived from intracranial pressure and cerebrospinal fluid pressure; constant at all timescales, applied to Γ_{exterior}

$\boldsymbol{\varphi}_t$ material motion

$q(\boldsymbol{X}, t)$ Winkler stiffness coefficient

$q(\tau)$ decay function representing the uptake of old fibers in remodeling

R rate of growth; $r\,dv = R\,dV$

R^{elastin} initial fraction of all the non-growing constituents of the material

R^k initial fraction of constituent k

$r^k(\tau)$ scalar measure of stress-induced growth in the direction of k-fibers

r rate of growth; $r = r(\boldsymbol{x}, t)$; $d/dt\,(dm) = r\,dv$

r_h homeostatic mass production; this represents the mass production rate required of a healthy artery to remain stable

$\boldsymbol{R}_i^A$ residual in the i-th direction at node A for use in solving (GNR, G)

$\restriction$ restriction of a function to a smaller domain

ρ current mass density per unit current volume; this number is assumed constant for all time, for all points in the body

$\mathcal{S}$ "space" of candidate solutions

$\mathcal{S}^h$ finite-dimensional approximation of $\mathcal{S}$

$\sigma^k(\tau)$ (scalar-valued) component of FSI stress that would be felt by k-fibers

$\boldsymbol{\sigma}_{\text{cardiac}}(\tau)$: Cauchy stress form of $\boldsymbol{S}_{\text{cardiac}}$

σ_h homeostatic stress; this represents the body's (postulated) target stress level; J.D. Humphrey believes σ_h is approximately 100kPa

t time

Δt timestep

$\mathcal{V}$ space of test functions

$\mathcal{V}^h$ finite-dimensional approximation of $\mathcal{V}$

$w(t)$: strain energy density function; $w(t) = w(\boldsymbol{X}, t)$

$\boldsymbol{x}$ point in current configuration

$\boldsymbol{X}$ point in reference configuration

AAA abdominal aortic aneurysm

ACA anterior communicating artery

aneurysm: bulge in the wall of an artery or vein

apoptosis: /apo·TOE·sis/ a highly-regulated biological process of programmed cell death; the opposite of apoptosis—unregulated cell proliferation—is cancer

ATP Adult Treatment Panel

ATP IV: Adult Treatment Panel's fourth and current set of guidelines for treatment of disease in adults

CHD coronary heart disease

CME Continuing Medical Education

CT x-ray computed tomography

CVD cardiovascular disease

EKG electrocardiograph

GNR growth and remodeling

growth: addition of mass, independent of deformation

IMT intima–media thickness

IRB Internal Review Board

ISUIA International Study of Unruptured Intracranial Aneurysms

JL4 Judkins 4 catheter for accessing left coronary artery

LAD left anterior descending artery

LCA left coronary artery

LCX left circumflex artery

LDL low density lipoprotein, aka bad cholesterol

LVAD left ventricular assist device; a mechanical aid for a failing heart

LVAD left ventricular assist device

MR magnetic resonance imaging

MRFIT Multiple Risk Factor Intervention Trial

MRI magnetic resonance imaging

PCommA: posterior communicating artery

PET positron emission tomography

QRS complex: waves on an EKG which represent ventricular contraction

Ramos branch: branch artery arising at the juncture of the LCX and LAD; the Ramos branch serves the same purpose as diagonal branches off the LCX or LAD

RCA right coronary artery

remodeling: changes in structure due to replacement of old material (fibers, in this work) with new material

SPECT single photon emission computed tomography

subclinical lesion: structural weakening within an artery that leads to aneurysm or may lead to aneurysm

tricuspid valve: heart valve in mammals that regulates blood flow from the right atrium to the right ventricle; this is blood traveling from the body into the lungs

UT The University of Texas at Austin

WSS wall shear stress

Index